

Estimating Associations Between Cumulative Exposure and Health via Generalized Distributed Lag Non-Linear Models using Penalized Splines

Tianyi Pan¹, Hwashin Hyun Shin^{2,3}, Glen McGee¹, and Alex Stringer¹

¹Department of Statistics and Actuarial Science, University of Waterloo

²Environmental Health Science and Research Bureau, Health Canada

³Department of Mathematics and Statistics, Queen's University

Abstract

Quantifying associations between short-term exposure to ambient air pollution and health outcomes is an important public health priority. Many studies have investigated the association considering delayed effects within the past few days. Adaptive cumulative exposure distributed lag non-linear models (ACE-DLNMs) quantify associations between health outcomes and cumulative exposure that is specified in a data-adaptive way. While the ACE-DLNM framework is highly interpretable, it is limited to continuous outcomes and does not scale well to large datasets. Motivated by a large analysis of daily pollution and respiratory hospitalization counts in Canada between 2001 and 2018, we propose a generalized ACE-DLNM incorporating penalized splines, improving upon existing ACE-DLNM methods to accommodate general response types. We then develop a computationally efficient estimation strategy based on profile likelihood and Laplace approximate marginal likelihood with Newton-type methods. We demonstrate the performance and practical advantages of the proposed method through simulations. In application to the motivating analysis, the proposed method yields more stable inferences compared to generalized additive models with fixed exposures, while retaining interpretability.

Keywords: Air pollution; Daily respiratory hospitalizations; Distributed lag non-linear model; Penalized splines; PM2.5.

1 Introduction

Quantifying associations between short-term exposure to air pollution and health outcomes remains a public health priority in Canada and around the world. For example, Health Canada and Environment and Climate Change Canada are tasked to monitor air quality and their associated risks to public health (Environment and Climate Change Canada, 2022). The motivation for this work is to characterize associations between daily hospitalization counts and $\text{PM}_{2.5}$ measurements from 2001 to 2018 aggregated by census division across Canada. Many studies have recognized that the association between air pollution and health is potentially non-linear and subject to delayed effects (Chen et al., 2017; Liu et al., 2019). To appropriately account for the delayed effect in a non-linear framework, two distinct classes of distributed lag non-linear models have been proposed. However, one class (e.g. Gasparrini, 2014) can be challenging to interpret, while the other (e.g. Wilson et al., 2022) requires continuous outcomes and therefore cannot be applied to our motivating analysis of health outcome counts. In this paper, we present a fast, scalable, and flexible framework to estimate associations between exposure and daily health outcome counts, accounting for the lagged effects and retaining interpretability.

A common approach for estimating non-linear associations between health outcomes and short-term exposure to air pollution is to fit a generalized additive model (GAM). This approach typically considers either (1) a single-day exposure (Powell et al., 2015; Shin et al., 2021), or (2) fixed cumulative exposure for lagged effects (Chen et al., 2017; Liu et al., 2019), which takes a simple average of exposures over several days. While the former approach ignores exposures on any other days, the latter can be sensitive to the choice of time window (e.g. Shin et al., 2021, 2023). In our motivating application, fitting GAMs for daily $\text{PM}_{2.5}$ with different definitions of exposure led to different inferences and wide intervals (Section 5). These results highlight the need for a more sophisticated modelling approach, allowing cumulative exposure to be specified adaptively rather than fixed in advance.

Distributed lag models (DLMs) address this by modelling the cumulative exposure as a weighted average with unknown weights estimated from the data (Schwartz, 2000; Zanobetti et al., 2000). We refer to the cumulative exposure under unknown weights as *adaptive cumulative exposure* (ACE), and the association function between ACE and response as *adaptive cumulative exposure-response function* (ACERF). The ACE generalizes the simple average exposure, and the ACERF is analogous to the exposure-response function in a GAM. However, the DLM restricts associations to be linear, which may not be appropriate for modelling air pollution and health. Two distinct classes of distributed lag non-linear model (DLNM) have been proposed to extend DLMs to handle non-linear associations.

The first class—which we call distributed response function DLNMs (DRF-DLNMs)—fits distinct non-linear associations at each lag via a bivariate exposure-lag-response function (Gasparrini et al., 2010; Gasparrini, 2014; Gasparrini et al., 2017; Mork and Wilson, 2022). Fitting DRF-DLNMs is computationally convenient (e.g. Gasparrini, 2011), but interpretation is not straightforward, relying on post-hoc summary statistics from the estimated bivariate surface, such as the exposure-response curve at a specific lag. These quantities are not directly comparable to the associations between cumulative exposure and response from the broadly used GAMs.

The second class of model instead specifies a non-linear function (i.e. ACERF) of the ACE itself (Wilson et al., 2022; Wang et al., 2023). We refer to this model as an *adaptive cumulative exposure distributed lag non-linear model* (ACE-DLNM). This is more interpretable, yielding inference similar to that from simpler GAMs: the lag weights indicate at which times exposure effects are strongest, and the ACERF characterizes the effect of cumulative exposure.

While the ACE-DLNM framework is highly interpretable, all existing ACE-DLNMs require continuous responses, preventing their applications to daily hospitalization counts and PM_{2.5}. In addition, they face difficulties in inference and computation. Wilson et al. (2022) proposed the Bayesian kernel machine regression and distributed lag model for Gaussian responses, but it relies on an MCMC approach for a number of kernel function coefficients equal to the sample size. Wang et al. (2023) introduced a distributed lag quantile regression model for continuous responses, but its estimation is based on a derivative-free algorithm, and it uses unpenalized splines requiring manual smoothness selection. Some functional regression models share similar forms to ACE-DLNMs (Kong et al., 2010; Ma, 2016); these too require continuous responses, which simplifies the objective functions into least-square problems that do not extend naturally to count responses. These approaches fit unpenalized splines and avoid over-fitting by grid-search for numbers of knots. The discrete number of knots cannot properly control smoothness (Eilers and Marx, 1996) and grid-search is infeasible with many smooth functions. Our motivating application considers five non-linear functions—the ACERF, lag weights, secular time trend, seasonality, temperature associations—and hence it requires a more efficient approach.

In this paper, we propose an inferential and computational framework for ACE-DLNMs, improving upon existing ACE-DLNM methods to accommodate general response types and scale to large datasets. We introduce a novel estimation approach, using profile likelihood and Laplace approximate marginal likelihood implemented by fast and accurate Newton-type methods. This framework: (1) is designed for possibly over-dispersed count responses but applies to more general types of data (including the exponential family), (2) allows for flexible non-linearity in weight function and ACERF (as well as association functions of covariates), (3) imposes smoothness penalties to avoid over-fitting, and (4) scales well to large datasets. We successfully apply the proposed ACE-DLNM to the motivating analysis of daily hospitalization counts and PM_{2.5} in five cities across Canada between 2001 and 2008, finding that it yields more stable inferences than simpler GAM approaches. We compare the proposed approach with the DRF-DLNM in this analysis and illustrate the advantage of the ACE-DLNM in interpretability.

2 Adaptive Cumulative Exposure Distributed Lag Non-Linear Model

Let Y_t be a response, which may be count, continuous or otherwise, observed at a set of N discrete time points, $t \in \mathcal{T} = \{1, 2, \dots, N\}$. Let $X : \mathbb{R} \rightarrow \mathbb{R}$ be a continuous exposure process. Denote x_s as the value of X at discrete time point $s \in \mathcal{T}^x$, where \mathcal{T}^x is not necessarily equal to or a subset of \mathcal{T} but its range is bounded by the range of \mathcal{T} . Let $\mathbf{z}_t \in \mathbb{R}^p$ represent the vector of covariates. We assume that $Y_t|X, \mathbf{z}_t$ follows a distribution

specified in Wood et al. (2016) with a finite mean $\mu_t \in \mathcal{M} \subseteq \mathbb{R}$ and unknown parameters θ .

An adaptive cumulative exposure distributed lag non-linear model (ACE-DLNM) is

$$g(\mu_t) = f \left\{ \int_0^L w(l)X(t-l)dl \right\} + \sum_{j=1}^p h_j(z_{tj}), \quad (1)$$

where $g : \mathcal{M} \rightarrow \mathbb{R}$ is a smooth, monotone link function. Define $E(t) = \int_0^L w(l)X(t-l)dl$ as the adaptive cumulative exposure (ACE) at time t with respect to the unknown smooth weight function $w(\cdot)$ and the maximum lag L . The $f(\cdot)$ is the unknown smooth adaptive cumulative exposure-response function (ACERF). The $h_j(\cdot)$ are p unknown smooth functions of covariates z_{tj} , $j = 1, \dots, p$, accommodating non-linear smooth functions (e.g., non-linear time trend and temperature association in the motivating application), linear components, and random effects (see e.g. Wood et al., 2016).

This model extends existing ACE-DLNMs from continuous responses to more general types of data. This extension introduces inferential and computational challenges. In Section 3, we propose a fast, scalable, and flexible framework for fitting ACE-DLNMs.

Motivated by the analysis of daily PM_{2.5} and hospitalization counts in Canada, in the remainder of the paper, we adopt a negative binomial distribution with mean μ_t and dispersion parameter $\theta > 0$ such that $\text{Var}(Y_t|X, \mathbf{z}_t) = \mu_t + \mu_t^2/\theta$ and hence $\text{Var}(Y_t|X, \mathbf{z}_t) > \text{E}(Y_t|X, \mathbf{z}_t)$ allowing for potential over-dispersion; and we use the log-link, $g(\mu_t) = \log(\mu_t)$.

2.1 Relation to GAM, DLM and DRF-DLNM

The ACE-DLNM includes the GAM and DLM as special cases by restricting either w or f . Assuming w is a fixed *known* function, the cumulative exposure $E(t)$ is therefore *known* and the ACE-DLNM reduces to a GAM, where the *known* $E(t)$ can be, e.g., the simple average over some set of days (Chen et al., 2017; Liu et al., 2019). On the other side, assuming f to be *linear*, the ACE-DLNM reduces to a DLM with $g(\mu_t) = \beta \int_0^L w(l)X(t-l)dl + \sum_{j=1}^p h_j(z_{tj})$.

The DRF-DLNM generalizes the DLM in another way, fitting potentially distinct non-linear associations for x_{t-l} at each lag l :

$$g(\mu_t) = \sum_{l=0}^{L-1} \psi(x_{t-l}, l) + \sum_{j=1}^p h_j(z_{tj}),$$

where $\psi(\cdot, \cdot)$ is a bivariate exposure-lag-response function (See Web Appendix A for details). Interpretation of the DRF-DLNM is based on the bivariate function $\psi(\cdot, \cdot)$.

2.2 Continuous Exposure Process

In ACE-DLNMs, we treat the exposure continuously, replacing $X(t)$ with an interpolating spline fit to the observed $x_s, s \in \mathcal{T}^x$; see Web Appendix B for details. The continuous exposure leads to a fast and exact evaluation of the ACEs and an identifiability proposition.

Under the spline representation, we propose a fast and exact approach to evaluate $E(t) = \int_0^L w(l)X(t-l)dl$ for each t , overcoming the need to approximate them by discretization that is adopted in all existing ACE-DLNMs. This approach uses de Boor's

algorithm (De Boor, 1978) and a modification of the method in Wood (2017b); see Web Appendix C.

2.3 Identifiability

As discussed in Wilson et al. (2022) and Wang et al. (2023), the model is not identifiable without constraints: we could replace $w(l)$ with $\tilde{w}(l) = c \cdot w(l)$ and $f(E)$ with $\tilde{f}(E) = f(E/c)$ but the likelihood holds the same. We impose the continuous constraints on w following Wilson et al. (2022): (1) scale constraint $\int_0^L w(l)^2 dl = 1$, and (2) sign constraint $\int_0^L w(l) dl > 0$. We then introduce Proposition 1. The proof is in Web Appendix D.2.

Proposition 1. *Under Conditions in Web Appendix D.2, there exists a knot sequence for spline $X(t)$, such that the ACE-DNLM is identifiable under the scale and sign constraints.*

3 Estimation

We represent $w(\cdot)$ and $f(\cdot)$ by cubic B-spline basis expansions, specifically: $f(E) = \sum_{q=1}^{d^f} b_q^f(E) \alpha_q^f$ and $w(l) = \sum_{q=1}^{d^w} b_q^w(l) \alpha_q^w$, where $b_q^f(\cdot)$ and $b_q^w(\cdot)$ are known B-spline basis functions, and $\boldsymbol{\alpha}^f = [\alpha_1^f, \dots, \alpha_{d^f}^f]^\top$ and $\boldsymbol{\alpha}^w = [\alpha_1^w, \dots, \alpha_{d^w}^w]^\top$ are unknown spline coefficients. We represent $h_j(\cdot)$ by basis expansions: $h_j(z_{tj}) = \sum_{q=1}^{d^{h_j}} b_{jq}^h(z_{tj}) \beta_{jq}$, where $b_{jq}^h(\cdot)$ are known basis functions, and let $\boldsymbol{\beta} = [\boldsymbol{\beta}_1^\top, \dots, \boldsymbol{\beta}_p^\top]^\top$ where $\boldsymbol{\beta}_j = [\beta_{j1}, \dots, \beta_{jd^j}]^\top$ for $j = 1, \dots, p$.

3.1 Reparameterization

For model identifiability, the sign and scale constraints (Section 2.3) are imposed on function w and hence its spline coefficients $\boldsymbol{\alpha}^w$. We propose the following reparameterization to map the constrained $\boldsymbol{\alpha}^w$ to an unconstrained $\boldsymbol{\phi}^w \in \mathbb{R}^{d^w-1}$.

We first reparametrize $w(l) = \sum_{q=1}^{d^w} b_q^w(l) \alpha_q^w$ via the sum-to-zero reparameterization (details in Wood, 2017a): $w(l) = \alpha_1^{w+} + w^+(l)$, where $w^+(l) = \sum_{q=2}^{d^w} b_q^{w+}(l) \alpha_q^{w+}$ and $\sum_{j=1}^J w^+(l_j) = 0$, with $\{l_j\}_{j=1}^J$ being an evenly spaced partition of $[0, L]$. We replace $\int_0^L w^+(l) dl$ by $(L/J) \sum_{j=1}^J w^+(l_j)$ with a large J , and then the sign of $\int_0^L w(l) dl$ is determined by the sign of α_1^{w+} . Define $\boldsymbol{\alpha}^{w+} = [\alpha_1^{w+}, \dots, \alpha_{d^w}^{w+}]^\top$ and \mathbf{C} as a $d^w \times d^w$ matrix with $C_{i,j} = \int_0^L b_i^{w+}(l) b_j^{w+}(l) dl$. We then reparametrize $\boldsymbol{\alpha}^{w+}$ by the unconstrained $\boldsymbol{\phi}^w \in \mathbb{R}^{d^w-1}$:

$$\boldsymbol{\alpha}^{w+} = \frac{[1, \boldsymbol{\phi}^{w\top}]^\top}{([1, \boldsymbol{\phi}^{w\top}] \mathbf{C} [1, \boldsymbol{\phi}^{w\top}]^\top)^{1/2}}.$$

Through the reparameterization above, the function w satisfies the sign and scale constraints, ensuring that the ACE-DNLM is identifiable under the Conditions in Proposition 1; see details in Web Appendix D.3. The computational complexity of the reparameterization is $O(J(d^w)^2)$, being dominated by the QR decomposition of a $J \times d^w$ -dimensional matrix.

Under the same identifiability constraints, Wilson et al. (2022) sampled parameters on a constrained parameter space. Ma (2016) imposed alternative constraints and minimized an objective function using a constrained optimization. The constrained sampling/optimization is challenging. In this proposed framework, the reparameterization absorbs the constraints, facilitating a simple unconstrained estimation.

3.2 Penalized Log-Likelihood

To control the roughness of the functions and avoid over-fitting, quadratic penalties, denoted by \mathcal{P} , are imposed on α^w , α^f and β : $\mathcal{P}(\alpha^w; \lambda^w) = (1/2)\lambda^w \alpha^{w\top} \mathbf{S}^w \alpha^w$, $\mathcal{P}(\alpha^f; \lambda^f) = (1/2)\lambda^f \alpha^{f\top} \mathbf{S}^f \alpha^f$, and $\mathcal{P}(\beta; \lambda^h) = \sum_{j=1}^p (1/2)\lambda_j^h \beta_j^\top \mathbf{S}_j^h \beta_j$, where $\lambda = [\lambda^w, \lambda^f, \lambda^h]^\top$, $\lambda^h = [\lambda_1^h, \dots, \lambda_p^h]^\top$ are unknown smoothing parameters, and \mathbf{S}^w , \mathbf{S}^f and $\mathbf{S}_j^h, j = 1, \dots, p$ are *fixed*, known penalty matrices. We set \mathbf{S}^w and \mathbf{S}^f as integrated squared second-order derivative penalty matrices (Wood, 2017b). Specifically, $\mathbf{S}^f = (S_{i,j}^f)_{1 \leq i,j \leq df}$ where $S_{i,j}^f = \int b_i^{f[2]}(x) b_j^{f[2]}(x) dx$ and $b_i^{f[2]}(x)$ denotes the second-order derivative of $b_i^f(x)$. We specify h_j using any basis expansion with the corresponding default penalty (see Wood et al., 2016 and Wood, 2015).

The basis functions $b_1^f(\cdot), \dots, b_{df}^f(\cdot)$, and thus \mathbf{S}^f , rely on the range of $E(t) = \int_0^L w(l)X(t-l)dl$, which varies by $w(\cdot)$ and can change at each optimization iteration. These changes make the derivatives of α^w and α^f intractable and require recomputing the expensive penalty matrix \mathbf{S}^f at each iteration. To address this, for a generic exposure X and any given t , we derive the predetermined bounds for $E(t)$ using the Cauchy-Schwarz inequality:

$$-\sqrt{\int_0^L X(t-l)^2 dl} \leq E(t) \leq \sqrt{\int_0^L X(t-l)^2 dl}.$$

It follows that the range of $E(t)$ over all $t \in \mathcal{T}$ is contained within $[-\bar{E}, \bar{E}]$ where $\bar{E} = \max_{t \in \mathcal{T}} \sqrt{\int_0^L X(t-l)^2 dl}$. We then define the basis functions and compute \mathbf{S}^f only once at the beginning.

For identifiability, we replace α^w with the unconstrained parameter $\phi^w \in \mathbb{R}^{d^w-1}$ as described in Section 3.1. The penalized log-likelihood is

$$\mathcal{L}(\phi^w, \alpha^f, \beta; \lambda, \theta) = l(\phi^w, \alpha^f, \beta; \lambda, \theta) - \mathcal{P}(\phi^w; \lambda^w) - \mathcal{P}(\alpha^f; \lambda^f) - \mathcal{P}(\beta; \lambda^h),$$

where $l(\phi^w, \alpha^f, \beta; \lambda, \theta) = \sum_{t=1}^N \log p(y_t; \mu_t, \theta)$ is the log-likelihood.

3.3 Optimization: Nested Profiling Approach

There are two challenges in maximizing \mathcal{L} for estimations. The first challenge is that estimating the coefficients for w and f simultaneously is infeasible (Ma, 2016), due to the nested, non-linear, and high-dimensional structure. Kong et al. (2010) and Ma (2016) used iterative approaches for continuous responses, which cannot be applied to general response types. Wang et al. (2023) used a profile likelihood approach for continuous responses but relied on a computationally inefficient derivative-free optimization, stating that implicit functions in the profile likelihood are not analytically tractable. The second challenge is

the need to estimate both $\boldsymbol{\theta}$ and $\boldsymbol{\lambda}$, which has been described by Wood (2017a) as the biggest computational challenge encountered when fitting penalized spline models.

To address both challenges, we propose a nested profiling approach. In the inner stage, given $\boldsymbol{\lambda}$ and $\boldsymbol{\theta}$, the $\boldsymbol{\phi}^w$, $\boldsymbol{\alpha}^f$ and $\boldsymbol{\beta}$ are estimated by a profile likelihood method. Rather than employing a derivative-free optimization as in Wang et al. (2023), we derive the analytical gradient and Hessian for fast and accurate Newton’s methods. In the outer stage, the mode of $[\boldsymbol{\phi}^w, \boldsymbol{\alpha}^f, \boldsymbol{\beta}]$ from the inner stage is plugged into the Laplace approximate marginal likelihood for estimating $\boldsymbol{\lambda}$ and $\boldsymbol{\theta}$ via Broyden–Fletcher–Goldfarb–Shanno (BFGS) method. See Web Appendix E for complete algorithms.

3.3.1 Inner Stage

Given $\boldsymbol{\lambda}$ and $\boldsymbol{\theta}$, we estimate $\boldsymbol{\phi}^w$ (for w), $\boldsymbol{\alpha}^f$ (for f) and $\boldsymbol{\beta}$ (for h_j) using a profile likelihood method. For a given $\boldsymbol{\phi}^w$, the estimation is reduced to an unpenalized estimation for a GAM. We denote the estimator as

$$\left[\hat{\boldsymbol{\alpha}}^f(\boldsymbol{\phi}^w; \boldsymbol{\lambda}, \boldsymbol{\theta}), \hat{\boldsymbol{\beta}}(\boldsymbol{\phi}^w; \boldsymbol{\lambda}, \boldsymbol{\theta}) \right] = \arg \max_{\boldsymbol{\alpha}^f, \boldsymbol{\beta}} \mathcal{L}(\boldsymbol{\phi}^w, \boldsymbol{\alpha}^f, \boldsymbol{\beta}; \boldsymbol{\lambda}, \boldsymbol{\theta}). \quad (2)$$

Then, we define the profile log-likelihood for $\boldsymbol{\phi}^w$ as

$$\mathbf{Q}(\boldsymbol{\phi}^w; \boldsymbol{\lambda}, \boldsymbol{\theta}) = \mathcal{L} \left(\boldsymbol{\phi}^w, \hat{\boldsymbol{\alpha}}^f(\boldsymbol{\phi}^w; \boldsymbol{\lambda}, \boldsymbol{\theta}), \hat{\boldsymbol{\beta}}(\boldsymbol{\phi}^w; \boldsymbol{\lambda}, \boldsymbol{\theta}); \boldsymbol{\lambda}, \boldsymbol{\theta} \right).$$

The profile likelihood estimators are obtained by

$$\hat{\boldsymbol{\phi}}^w(\boldsymbol{\lambda}, \boldsymbol{\theta}) = \arg \max_{\boldsymbol{\phi}^w} \mathbf{Q}(\boldsymbol{\phi}^w; \boldsymbol{\lambda}, \boldsymbol{\theta}). \quad (3)$$

Plugging $\hat{\boldsymbol{\phi}}^w(\boldsymbol{\lambda}, \boldsymbol{\theta})$ into Equation 2, we obtain the estimators $\hat{\boldsymbol{\alpha}}^f(\boldsymbol{\lambda}, \boldsymbol{\theta}) = \hat{\boldsymbol{\alpha}}^f(\hat{\boldsymbol{\phi}}^w(\boldsymbol{\lambda}, \boldsymbol{\theta}); \boldsymbol{\lambda}, \boldsymbol{\theta})$ and $\hat{\boldsymbol{\beta}}(\boldsymbol{\lambda}, \boldsymbol{\theta}) = \hat{\boldsymbol{\beta}}(\hat{\boldsymbol{\phi}}^w(\boldsymbol{\lambda}, \boldsymbol{\theta}); \boldsymbol{\lambda}, \boldsymbol{\theta})$.

The solution of Equation 3 relies on Equation 2 and contributes to the outer stage; thus, the stability and speed of the optimization are important. We employ a Newton’s method with two modifications: (1) the Q-Newton method of Truong et al. (2023) ensures that the Newton step is in an ascent direction and of appropriate length, and (2) step-halving ensures that the objective function increases after each Newton update.

Newton’s methods need the gradient and Hessian of the objective functions in Equations 2 and 3. For Equation 2, we describe the analytic forms of the gradient and Hessian of \mathcal{L} in Web Appendix F.1. For Equation 3, it is challenging to derive the gradient and Hessian of the profile likelihood \mathbf{Q} because of the implicit functions $\hat{\boldsymbol{\alpha}}^f(\boldsymbol{\phi}^w; \boldsymbol{\lambda}, \boldsymbol{\theta})$ and $\hat{\boldsymbol{\beta}}(\boldsymbol{\phi}^w; \boldsymbol{\lambda}, \boldsymbol{\theta})$ (see e.g. Wang et al., 2023). In this approach, we analytically evaluate these derivatives using the implicit differentiation technique; see details in Web Appendix F.2.

3.3.2 Outer Stage

Denote $\mathbf{u} = [\boldsymbol{\phi}^w, \boldsymbol{\alpha}^f, \boldsymbol{\beta}]^\top$ and the estimator from the inner stage as $\hat{\mathbf{u}}(\boldsymbol{\lambda}, \boldsymbol{\theta})$. Inference for $\boldsymbol{\lambda}$ and $\boldsymbol{\theta}$ is based on the Laplace approximate marginal likelihood (LAML; Wood, 2011) that depends on $\hat{\mathbf{u}}(\boldsymbol{\lambda}, \boldsymbol{\theta})$. LAML is preferred over prediction error criteria such as Akaike’s information criterion (AIC) and generalized cross-validation (GCV), due to its greater resistance to over-fitting as well as other advantages (Wood, 2011, 2017a).

We estimate $\boldsymbol{\lambda}$ and $\boldsymbol{\theta}$ by maximizing the log-LAML:

$$\begin{aligned}\mathcal{L}_{\text{LA}}^*(\boldsymbol{\lambda}, \boldsymbol{\theta}) = & \mathcal{L}(\hat{\mathbf{u}}(\boldsymbol{\lambda}, \boldsymbol{\theta}); \boldsymbol{\lambda}, \boldsymbol{\theta}) - \frac{1}{2} \log \{\det \mathbf{H}(\hat{\mathbf{u}}(\boldsymbol{\lambda}, \boldsymbol{\theta}); \boldsymbol{\lambda}, \boldsymbol{\theta})\} \\ & + \frac{1}{2} \log |\lambda^w \mathbf{S}^w|_+ + \frac{1}{2} \log |\lambda^f \mathbf{S}^f|_+ + \frac{1}{2} \sum_{j=1}^p \log |\lambda_j^h \mathbf{S}_j^h|_+ + C,\end{aligned}$$

where $\mathbf{H}(\hat{\mathbf{u}}(\boldsymbol{\lambda}, \boldsymbol{\theta}); \boldsymbol{\lambda}, \boldsymbol{\theta}) = -\partial^2 \mathcal{L}(\hat{\mathbf{u}}(\boldsymbol{\lambda}, \boldsymbol{\theta}); \boldsymbol{\lambda}, \boldsymbol{\theta}) / \partial \mathbf{u}^2$, $\log |\mathbf{A}|_+$ is the product of positive eigenvalues of matrix \mathbf{A} , and C is a constant. We write the estimators as $(\log \hat{\boldsymbol{\lambda}}, \log \hat{\boldsymbol{\theta}}) = \arg \max_{\log \boldsymbol{\lambda}, \log \boldsymbol{\theta}} \mathcal{L}_{\text{LA}}^*$. Finally, plugging $\hat{\boldsymbol{\lambda}}, \hat{\boldsymbol{\theta}}$ into $\hat{\mathbf{u}}(\boldsymbol{\lambda}, \boldsymbol{\theta})$ yields $\hat{\mathbf{u}} = \hat{\mathbf{u}}(\hat{\boldsymbol{\lambda}}, \hat{\boldsymbol{\theta}})$.

To maximize $\mathcal{L}_{\text{LA}}^*$, the derivative-free optimization algorithms are inefficient. We propose to use a Newton-type method, BFGS. Unlike the inner stage, we do not adopt Newton's method here, since computing the Hessian of $\mathcal{L}_{\text{LA}}^*$ is both analytically and algorithmically complicated. The BFGS needs the gradient of $\mathcal{L}_{\text{LA}}^*$, involving that of $\mathcal{L}(\hat{\mathbf{u}}(\boldsymbol{\lambda}, \boldsymbol{\theta}); \boldsymbol{\lambda}, \boldsymbol{\theta})$, $\log |\mathbf{A}|_+$ terms and $\log \{\det \mathbf{H}(\hat{\mathbf{u}}(\boldsymbol{\lambda}, \boldsymbol{\theta}); \boldsymbol{\lambda}, \boldsymbol{\theta})\}$. We find the gradient of $\mathcal{L}(\hat{\mathbf{u}}(\boldsymbol{\lambda}, \boldsymbol{\theta}); \boldsymbol{\lambda}, \boldsymbol{\theta})$ analytically using the implicit differentiation; see Web Appendix F.3. The derivatives of $\log |\mathbf{A}|_+$ terms follow directly from Wood et al. (2016). It is difficult to obtain analytical gradient of $\log \{\det \mathbf{H}(\hat{\mathbf{u}}(\boldsymbol{\lambda}, \boldsymbol{\theta}); \boldsymbol{\lambda}, \boldsymbol{\theta})\}$, and we compute it via the automatic differentiation of the Cholesky algorithm, achieved using the `autodiff` (Leal, 2018) library in C++.

3.4 Confidence Intervals

To estimate the confidence intervals for w , f and h_j , we need to estimate those for the coefficients $\boldsymbol{\alpha}^w$, $\boldsymbol{\alpha}^f$ and $\boldsymbol{\beta}$. In this framework, given $\boldsymbol{\lambda}$ and $\boldsymbol{\theta}$, the unconstrained $\mathbf{u} = [\boldsymbol{\phi}^w, \boldsymbol{\alpha}^f, \boldsymbol{\beta}]^\top$ is estimated by maximizing the log-likelihood, where $\boldsymbol{\phi}^w$ is from a non-linear transformation of $\boldsymbol{\alpha}^w$. We propose to estimate the confidence intervals via a sampling strategy similar to one presented in Stringer et al. (2024). First, we sample $\mathbf{u}^{(i)} = [\boldsymbol{\phi}^{w(i)}, \boldsymbol{\alpha}^{f(i)}, \boldsymbol{\beta}^{(i)}]^\top$ from $\mathcal{N}(\hat{\mathbf{u}}, [\mathbf{H}(\hat{\mathbf{u}}; \hat{\boldsymbol{\lambda}}, \hat{\boldsymbol{\theta}})]^{-1})$ for $i = 1, 2, \dots, R$, where R is the number of samples chosen by the user. Second, for each $\boldsymbol{\phi}^{w(i)}$, we compute $\boldsymbol{\alpha}^{w(i)}$ by the reparameterization in Section 3.1. Finally, the approximated $(1 - \alpha)$ confidence intervals are obtained by the $(\alpha/2, 1 - \alpha/2)$ sample quantiles of $\boldsymbol{\alpha}^{w(i)}$, $\boldsymbol{\alpha}^{f(i)}$ and $\boldsymbol{\beta}^{(i)}$. In this procedure, we only use the point estimates of $\boldsymbol{\lambda}$ and $\boldsymbol{\theta}$, ignoring their uncertainty, as is typical in a GAM (see e.g. Wood et al., 2016).

The delta method can also be used to quantify the uncertainty in transformed maximum likelihood estimators (see Web Appendix G for details). In simulations, however, we found that it yielded poor finite sample performance (see Web Table 5). Instead we recommend the sampling method described above.

4 Simulations

In this section, we conduct two simulation studies to investigate the performance of the proposed framework, implemented in the R package `aceDLNM`. Simulation A demonstrates the absolute performance, showing low RMSE and appropriate coverage. Simulation B compares the ACE-DLNM with the GAM and DRF-DLNM, illustrating its practical advantages.

4.1 Simulation A: Absolute Performance

In this simulation, we demonstrate the performance of the proposed ACE-DLNM. The continuous exposure is obtained by interpolating the true daily PM_{2.5} in Waterloo (visualized in Web Appendix H.1), starting from January 1, 2001, with a sample size of 1,000 or 2,000. We set a time trend $h(t) = 0.5 \sin(t/150)$. We consider three weight functions w with a two-week maximum lag (Type (i) $w(l)$ peaks at $l = 3$ and then gradually decreases, Type (ii) $w(l)$ is flat up to around $l = 5$ and decreases, and Type (iii) $w(l)$ decays exponentially from $l = 0$), and three ACERFs f (Type (i) f is cubic, Type (ii) f is from the standard normal density function, and Type (iii) f is linear). These functions are shown as solid black curves in Figure 1. The true dispersion parameter in the negative binomial distribution is $\theta = 8$, yielding large over-dispersion. We generate the count outcome according to the model:

$$\log(\mu_t) = f \left\{ \int_0^{15} w(l)X(t-l)dl \right\} + h(t).$$

Table 5 reports root mean square error (RMSE), 95% confidence intervals coverage (Cvg) and average widths (Width) for estimates of w and f across grids of evenly spaced values over 10,000 replicates. In Figure 1, we plot the estimates from the first 100 simulated datasets for three cases as examples; remaining results are provided in Web Appendix H.2.1. In all settings, we observe low RMSE and nominal interval coverage in estimating w and f , indicating the validity of the proposed approach. We observe that the RMSE for f is higher than that for w . A possible explanation is that f measures the association between the ACE and the outcome, while the ACE itself is computed using the estimated w . Estimation error in w introduces additional variability into the estimation of f , resulting in a higher RMSE. When the true f is linear (Type (iii)), the model simplifies to a DLM. We compare the ACE-DLNM and the correctly specified DLM under this setting in Web Appendix H.3, and find that the ACE-DLNM achieves similar performance. Web Table 4 shows that the proposed method performs well in estimating the time trend $h(t)$ and the dispersion parameter θ .

4.2 Simulation B: Relative Performance

This simulation compares the ACE-DLNM with the GAM, which pre-specifies the cumulative exposure as if the lag weight was known *a priori*, and the DRF-DLNM, which fits a bivariate exposure-lag-response surface, to illustrate the advantages of the ACE-DLNM in practice.

The data are generated from the GAMs: $\log(\mu_t) = f(E_t) + h(t)$, where the cumulative exposure E_t is specified as one of the following: (i) same-day exposure $E_t = x_t$; (ii) average of 0- and 1-day lags $E_t = (x_t + x_{t-1})/2$; (iii) average from 0- to 7-day lags $E_t = (x_t + x_{t-1} + \dots + x_{t-7})/8$; (iv) average from 0- to 14-day lags $E_t = (x_t + x_{t-1} + \dots + x_{t-14})/15$; or (v) weighted average $E_t = w_0x_t + w_1x_{t-1} + \dots + w_{14}x_{t-14}$ where the non-constant weights are from Type (i) $w(l)$ in Simulation A. The true f is Type (i) from Simulation A. The sample size is 2,000, and all other settings remain the same as in Simulation A.

We compare the ACE-DLNM with: (a) GAM using the same-day exposure (GAM lag0), (b) GAM using the average of 0- and 1-day lags (GAM avg lag0-1), (c) GAM using the average from 0- to 7-day lags (GAM avg lag0-7), (d) GAM using the average

Table 1: Results of Simulation A under different weight functions w and ACERFs f . The RMSE, 95% confidence intervals coverage (Cvg) and average widths (Width) for w and f with the sample size $N = 1000$ and 2000 are reported.

N	w			f		
	RMSE	Cvg	Width	RMSE	Cvg	Width
Type (i) w				Type (i) f		
1000	0.015	0.970	(0.064)	0.126	0.943	(0.467)
2000	0.011	0.979	(0.049)	0.102	0.951	(0.355)
				Type (ii) f		
1000	0.012	0.977	(0.055)	0.085	0.964	(0.352)
2000	0.009	0.980	(0.042)	0.062	0.965	(0.263)
				Type (iii) f		
1000	0.018	0.961	(0.075)	0.027	0.945	(0.104)
2000	0.014	0.973	(0.060)	0.019	0.954	(0.078)
Type (ii) w				Type (i) f		
1000	0.014	0.965	(0.060)	0.121	0.949	(0.449)
2000	0.010	0.966	(0.044)	0.092	0.948	(0.318)
				Type (ii) f		
1000	0.012	0.968	(0.051)	0.079	0.962	(0.337)
2000	0.008	0.973	(0.038)	0.056	0.964	(0.235)
				Type (iii) f		
1000	0.017	0.954	(0.071)	0.026	0.948	(0.102)
2000	0.013	0.964	(0.055)	0.018	0.951	(0.073)
Type (iii) w				Type (i) f		
1000	0.017	0.964	(0.063)	0.148	0.950	(0.550)
2000	0.011	0.975	(0.050)	0.117	0.950	(0.427)
				Type (ii) f		
1000	0.013	0.975	(0.060)	0.100	0.961	(0.410)
2000	0.010	0.979	(0.047)	0.078	0.955	(0.316)
				Type (iii) f		
1000	0.021	0.969	(0.093)	0.030	0.943	(0.114)
2000	0.017	0.976	(0.078)	0.023	0.946	(0.090)

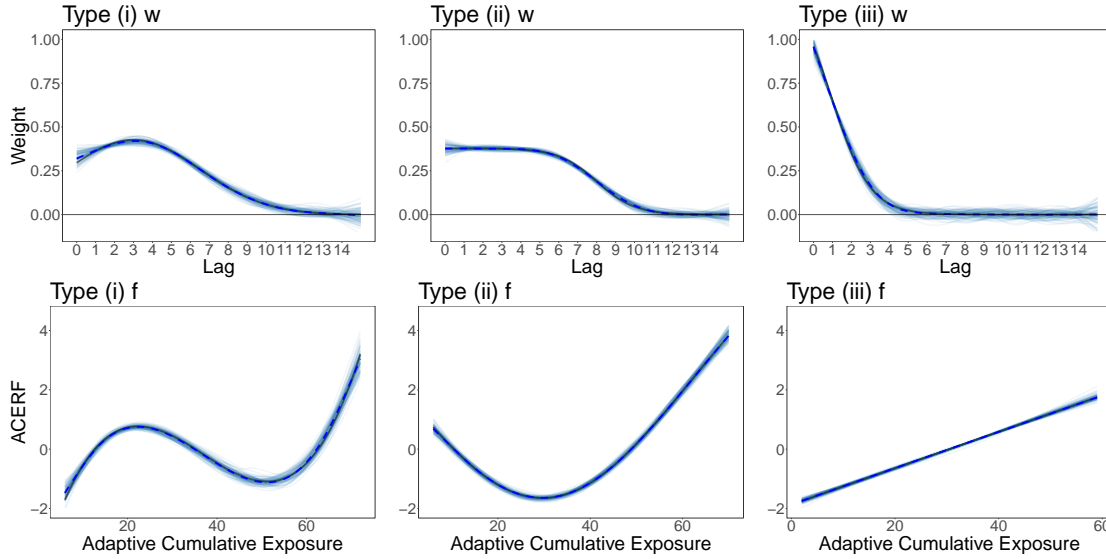


Figure 1: Visualization of Simulation A Results. The data are generated with (1) the first column: Type (i) weight function and Type (i) ACERF; (2) the second column: Type (ii) weight function and Type (ii) ACERF; and (3) the third column: Type (iii) weight function and Type (iii) ACERF. The sample size is 1,000. The estimates from the first 100 simulated datasets for the weight function w (first row) and the ACEFR f (second row) are shown as blue curves. The dashed blue curves show the mean of the estimates over all of the 10,000 simulated datasets. The true functions are the solid black curves.

from 0- to 14-day lags (GAM avg lag0-14), and (e) DRF-DLNM (Gasparrini et al., 2017). Models (a)—(d) are correctly specified under scenarios (i)—(iv) respectively. We evaluate performance using RMSE and 95% confidence intervals coverage (Cvg) for $f(E_t)$ evaluated over $t \in \mathcal{T}$ across 10,000 replicates, as reported in Table 2.

Under scenarios (i)—(iv) where the data are generated from the GAM using a simple average, the GAM with the correctly specified lag window achieves the lowest RMSE and near nominal coverage. In contrast, GAMs with misspecified lag windows perform poorly. The ACE-DLNM yields the second-best performance, close to the correctly specified GAM, and substantially outperforms the misspecified GAMs. Under scenario (v) where the lag weights are non-constant, the ACE-DLNM is the only model that achieves low RMSE and appropriate coverage, while all other models perform poorly with high RMSE and substantial undercoverage. In practice, the true relevant lag window for the cumulative exposure is unknown, and the weights are also unknown and are not expected to remain constant across the lag window. The GAM, on its own, fails to offer a practical way to define the appropriate cumulative exposure, whereas the ACE-DLNM addresses this by treating cumulative exposure adaptively.

Mild under-coverage is observed for the ACE-DLNM (0.932, 0.939 and 0.922), due to the difficulty of making inferences in these scenarios, where the true weight holds constant over the relevant lag window and then drops to zero, causing a discontinuity that is challenging to capture using a spline.

The DRF-DLNM models a separate function of exposure at each lag, rather than a single function applied to the cumulative exposure as in ACE-DLNM and GAM. It is correctly specified only under scenario (i), where the cumulative exposure is the same-day exposure,

Table 2: Results of Simulation B under different data generations. The RMSE and 95% confidence intervals coverage (Cvg) for $f(E_t)$ are reported.

	ACE-DLNM	GAM lag 0	GAM avg lag 0-1	GAM avg lag 0-7	GAM avg lag 0-14	DRF-DLNM
(i) $E_t = x_t$						
RMSE	0.069	0.040	0.427	0.600	0.612	0.116
Cvg	0.932	0.959	0.165	0.094	0.084	0.944
(ii) $E_t = (x_t + x_{t-1})/2$						
RMSE	0.062	0.405	0.040	0.518	0.537	0.267
Cvg	0.939	0.184	0.959	0.115	0.096	0.750
(iii) $E_t = (x_t + x_{t-1} + \dots + x_{t-7})/8$						
RMSE	0.060	0.520	0.504	0.041	0.442	0.359
Cvg	0.922	0.083	0.101	0.964	0.188	0.554
(iv) $E_t = (x_t + x_{t-1} + \dots + x_{t-14})/15$						
RMSE	0.048	0.597	0.586	0.457	0.042	0.340
Cvg	0.954	0.063	0.064	0.133	0.967	0.355
(v) $E_t = w_0x_t + w_1x_{t-1} + \dots + w_{14}x_{t-14}$						
RMSE	0.051	0.529	0.512	0.160	0.411	0.357
Cvg	0.955	0.080	0.091	0.481	0.167	0.484

and performs better than the misspecified GAMs in this case. However, the RMSE is higher than that of the ACE-DLNM and GAM lag0, potentially because of the difficulty of estimating 15 separate functions when 14 of them are truly null. Under scenarios (ii)—(v), the DRF-DLNM is misspecified and behaves poorly as expected. Note that ACE-DLNM and DRF-DLNM rely on different model assumptions, and their performance depends on how well these align with the true data-generating mechanism; see also Web Appendix H.4 for two supplementary simulations where the DRF-DLNM is correctly specified. In practice, selection may be based on model fit or interpretability considerations, which we further illustrate in Section 5.

5 Application: Adverse Health Effect of Air Pollution in Canada

5.1 Background and Aim

Health Canada monitors adverse health effect of ambient air pollution in collaboration with Environment and Climate Change Canada, including the public health risks attributable to short-term exposure to fine particulate matter smaller than 2.5 micrometers in diameter ($PM_{2.5}$). $PM_{2.5}$ is emitted directly into the air from vehicles, residential wood-burning, industry, wildfires, and burning waste. Numerous epidemiological studies have established significant associations between exposure to airborne $PM_{2.5}$ and adverse health effects, including non-accidental all-cause hospitalizations (Dominici et al., 2006) and mortality (Pope et al., 1995). The goal of this analysis is to quantify *non-linear* associations between *cumulative* exposure to $PM_{2.5}$ and hospitalizations (respiratory morbidity) in five cities across Canada from January 1, 2001 to December 31, 2018.

5.2 Data sources

Daily counts of hospitalization (morbidity) were collected from the Canadian Institute for Health Information (CIHI) for 2001-2018. Based on the International Classification of Diseases 10th version (World Health Organization, 2019), we extracted the respiratory (J00-J99) morbidity and aggregated them by city (census division). Where there were multiple causes (up to 10) diagnosed by a medical doctor, we used the first cause in this analysis.

Hourly $PM_{2.5}$ concentrations were obtained from the National Air Pollution Surveillance (NAPS) program (Environment and Climate Change Canada, 2021). For each NAPS monitoring station, daily average $PM_{2.5}$ concentrations were calculated if at least 18 hourly concentrations were available for the given day. In the case of short gaps (up to 10 consecutive hours), the interpolation method of Burr et al. (2015) was employed. For cities with multiple NAPS stations, average concentrations of available stations were taken to represent city level air pollution concentrations. More details can be found in Shin et al. (2024).

Daily mean temperatures were also obtained from the National Climate Data and Information Archive (Environment and Climate Change Canada, 2024). Daily temperatures

for each city were calculated using the same approach as for daily PM_{2.5} concentrations.

5.3 Analysis

We analyzed five cities—Waterloo, Peel, Hamilton, Calgary and Vancouver—that represent a diverse range of geographies, climates, industries, and populations. (See Web Table 9 for summary data.) The outcomes were counts, and their sample variances were relatively large (e.g., Peel had an average respiratory morbidity of 16.4 with a variance of 37.2), indicating potential over-dispersion. Moreover, the datasets were quite large: outcomes and exposure were measured daily between 2001 and 2018 for a total of 6,574 days for each city.

We therefore fit the generalized ACE-DLNM with the negative binomial distribution separately for each of the five cities. The mean model is

$$\log(\mu_t) = f \left\{ \int_0^{15} w(l)X(t-l)dl \right\} + h_1(t) + h_2(\text{Month}_t) + h_3(\text{Temp}_t) + \sum_{p=1}^6 \beta_p^{\text{DOW}} \text{DOW}_{pt},$$

where Y_t is the respiratory morbidity count, X is the PM_{2.5}, $h_1(t)$ and $h_3(\text{Temp}_t)$ are cubic B-splines for long-term trend and temperature association, and $h_2(\text{Month}_t)$ is a cyclic cubic spline of month to capture seasonality. Indicator variables for the day of week (DOW) are included. We quantify the associations without making causal claims in this paper, and leave open the possibility of the presence of confounders.

We compare the ACE-DLNM to simpler GAMs fitted under different pre-specified cumulative exposures (via R package `mgcv`; Wood, 2015): (a) same-day exposure (lag0), (b) average of 0- and 1-day lags (avg lag0-1), (c) average from 0- to 7-day lags (avg lag0-7), and (d) average from 0- to 14-day lags (avg lag0-14), while keeping all other specifications same with those of the ACE-DLNM. The cumulative exposures are scaled by constants, to align with the constraints in ACE-DLNM, making the association functions comparable. The estimates for all quantities are almost identical among these models (see Web Appendix I.2), except for the association function f .

We also fit the DRF-DLNM (Gasparrini et al., 2017) via the `dlnm` package (Gasparrini, 2011). Its model specification is similar to the ACE-DLNM, except that the non-linear association with the ACE is replaced by 15 distinct lag-specific functions, i.e. $\sum_{l=0}^{14} \psi(x_{t-l}, l)$.

5.4 Results

Figure 2 demonstrates the results for respiratory morbidity in the five selected cities. Figure 2 demonstrates the results for respiratory morbidity in the five selected cities. The estimated weight function and ACERF from the ACE-DLNM, as well as the exposure-response function (ERF) from the GAMs, are plotted. The ACE-DLNM estimates non-linear associations in Waterloo and Calgary, a slight non-linear association in Peel, and a linear association in Hamilton. In contrast, the GAMs, with pre-specified cumulative exposures, fail to capture these non-null associations in some cases. In Peel and Hamilton, where the relevant lag windows cover about two or three days, the GAM with same-day exposure (lag0) yields a similar association to the ACE-DLNM. However, in Waterloo and Calgary, where the relevant lag windows extend to about one week, the estimated associations from

the GAM lag0 are nonsignificant with wide confidence intervals. This highlights the advantage of ACE-DLNMs in making stable inferences by adaptively estimating cumulative exposure without the need for pre-specification.

ACE-DLNMs require non-constant (non-null) ACERFs for identifiability (see Web Appendix D). In Vancouver, the association is close to zero, making the weight function uninformative. Even in this nonidentifiable case, the ACE-DLNM provides a stable and narrower confidence interval for the association than GAMs.

For cities with non-constant ACERFs, estimated weight functions behave as expected, starting positive at zero lag and nearing zero at large lags. But the shape varies by city. In Waterloo, for example, the weight function maintains a large value for up to one week, suggesting long-lasting exposure associations, whereas in Peel, it declines sharply after two days. The variation in weight functions emphasizes the flexibility of ACE-DLNM in capturing city-specific lag patterns.

Model diagnostics based on randomized quantile residuals (Dunn and Smyth, 1996) show no evidence of a lack of model fit (Web Appendix I.2). We compare the fitted negative binomial models to more restrictive Poisson models using AIC; the results in Web Table 15 support our choice of the negative binomial distribution.

To compare ACE-DLNM and DRF-DLNM, we report two types of rate ratios: (1) the lag-specific rate ratio, defined as the ratio of morbidity rates when the exposure at a specific lag increases from the lower quartile (Q_1) to upper quartile (Q_3) while all other lags are held at Q_1 ; and (2) the overall rate ratio, defined as the ratio of morbidity rates when the entire exposure profile shifts from Q_1 to Q_3 simultaneously. We use the Hamilton data as an example where $Q_1 = 4.33$ and $Q_3 = 11.11$. Figures 3a and 3b show the rate ratios from ACE-DLNM and DRF-DLNM. The two models yield similar lag-specific rate ratios—significant from lag-0 to lag-2 and then gradually declining to null. The ACE-DLNM provides a more efficient estimate of the overall rate ratio with a narrower confidence interval. AIC comparisons also favour the ACE-DLNM. The results for the remaining four cities are provided in Web Appendix I.2. The patterns of estimated rate ratio are broadly similar between the two models.

However, the rate ratio comparing Q_3 and Q_1 does not reflect nonlinearity, and the underlying interpretations of the models differ a lot. The DRF-DLNM estimates a bivariate exposure-lag-response surface—estimating a separate non-linear function at each lag. We plot the estimated surface with its 95% confidence interval in Figure 3d. It can be difficult to interpret the bivariate surfaces directly, so we plot the separate non-linear function evaluated at each lag in Figure 3e and Web Figure 14. At a specific lag, the estimated function, among the 15 functions, describes how the exposure at that lag is associated with the response. Although these functions vary in scale, we cannot observe much variation in their shape—which is also observed in the other four cities (Web Appendix I.2)—suggesting that modelling separate functions at each lag may be unnecessary but complicate the interpretations. In contrast, the ACE-DLNM uses only two univariate functions: the lag weight and ACERF, as shown in Figure 3c. The ACERF describe the association between the cumulative exposure and response, while the lag weight indicates the relative contribution of each lag. Both estimated functions are interpretable and informative in this analysis.

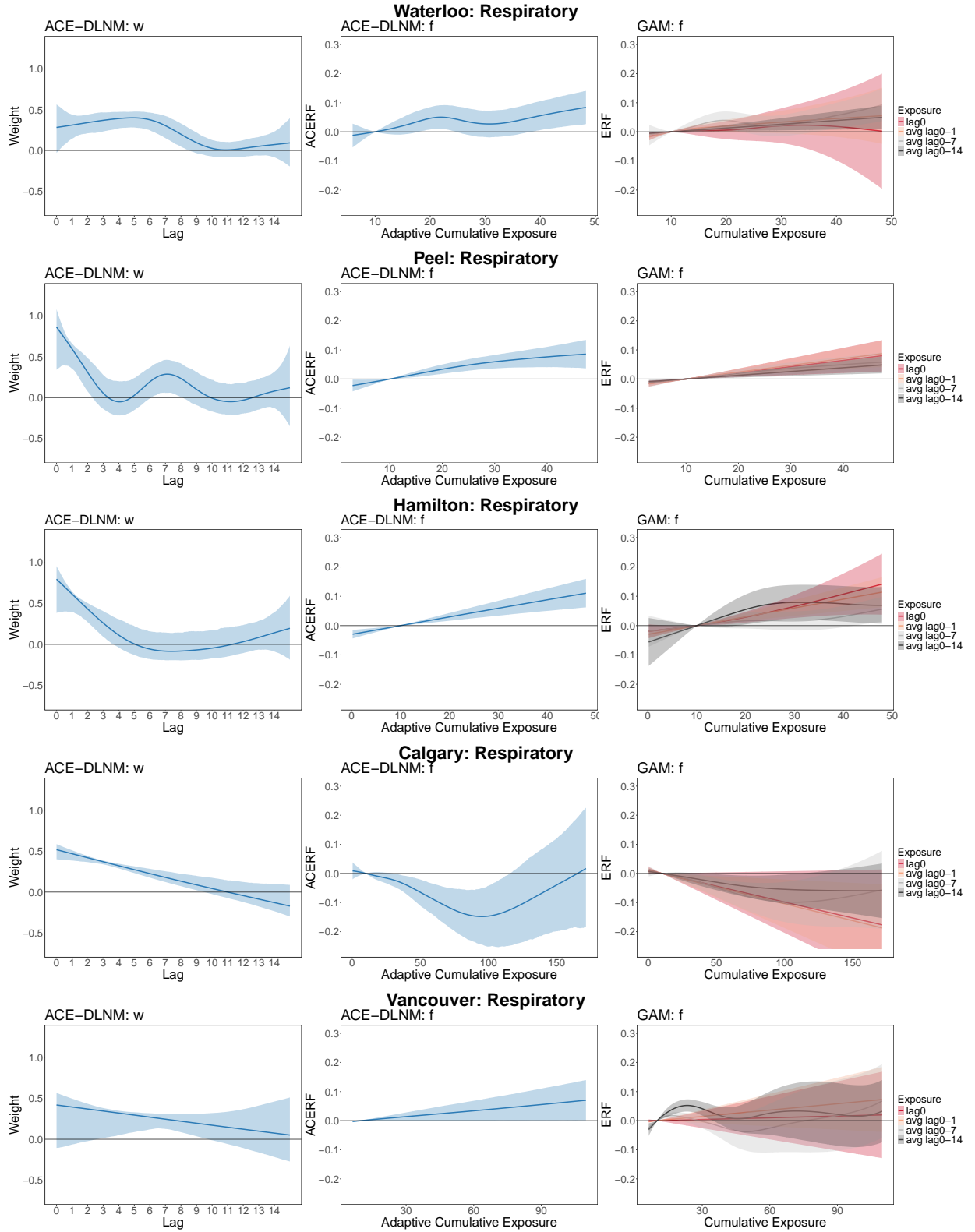


Figure 2: Estimated weight (left column) and ACERF (middle column) from ACE-DLNM and the estimated ERF (right column) from GAM for respiratory morbidity in five cities: Waterloo (top row), Peel, Hamilton, Calgary and Vancouver (bottom row). The point estimates are in solid curves with 95% confidence intervals in shade.

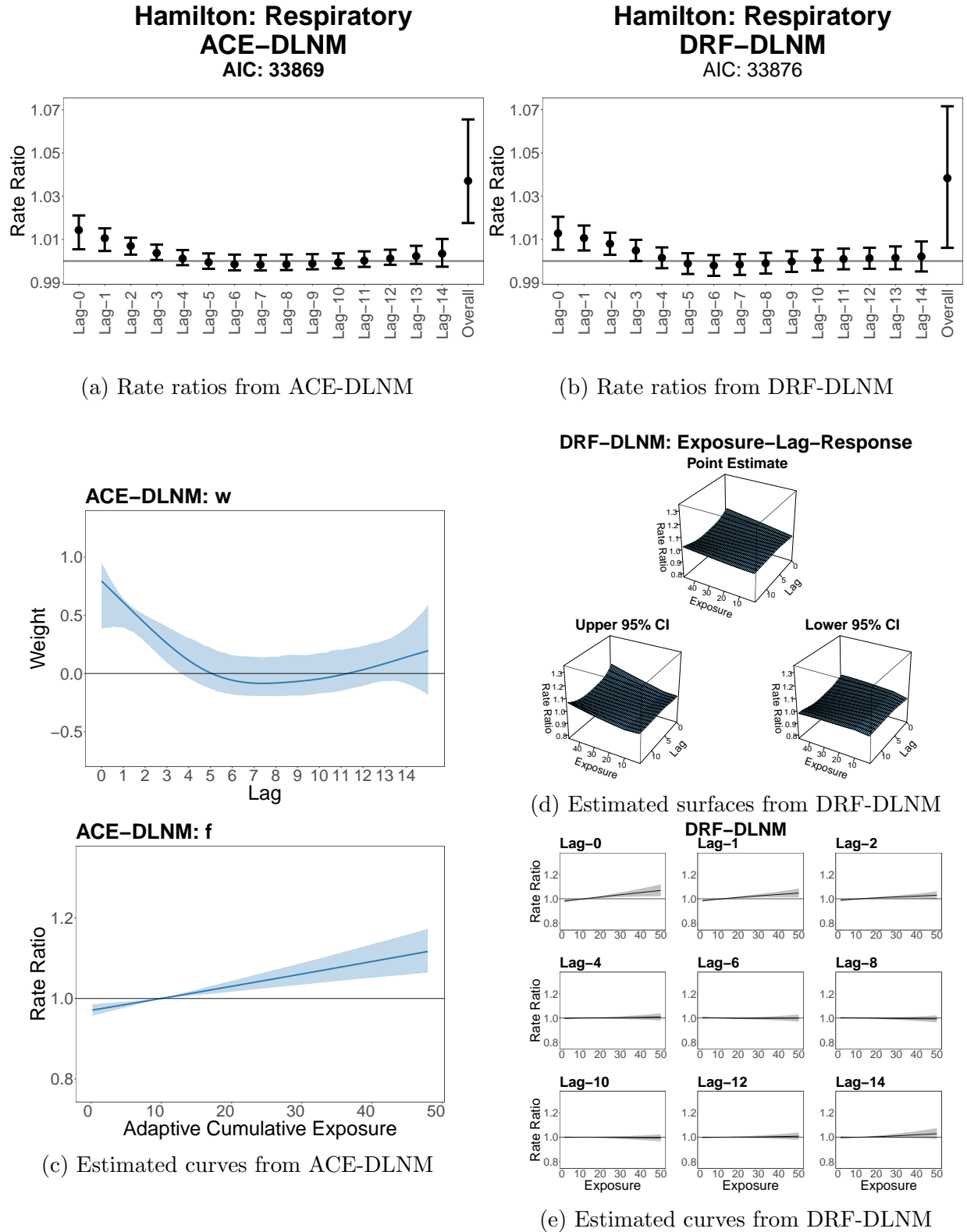


Figure 3: Comparisons between the ACE-DLNM and DRF-DLNM in the Hamilton dataset. The lag-specific and overall rate ratios from the ACE-DLNM (a) and DRF-DLNM (b) are plotted. Interpretation of the ACE-DLNM is based on the two curves shown in (c). Interpretation of the DRF-DLNM relies on the bivariate surfaces in (d), and we plot the estimated curves at selected lags in (e) (the full results are provided in Web Figure 14). The AICs for the two fitted models are reported.

6 Discussion

The ACE-DLNM quantifies the associations between cumulative exposure and health outcomes. However, the existing ACE-DLNM methods are limited to continuous outcomes and do not scale well to large datasets. We present an inferential and computational framework for ACE-DLNMs that addresses these limitations, allowing for general response types and large datasets. We successfully apply the proposed ACE-DLNM to our motivating analysis, and the results demonstrate that the ACE-DLNM provides more stable inferences than simpler GAMs and is more interpretable compared to the DRF-DLNM.

The distributed lag model framework is conceptually similar to the weighted cumulative exposure (WCE) models. Breslow et al. (1983) and Thomas (1988) proposed the WCE, and some flexible modelling approaches were developed by, for example, Hauptmann et al. (2000) and Sylvestre and Abrahamowicz (2009). However, the existing WCE models are limited by the assumption of a linear exposure-response association. This limitation can be addressed by the DRF-DLNM (Gasparrini, 2014) or by the ACE-DLNM as discussed in this paper.

This paper uses air pollution data without gaps over the study period and assumes no measurement error, as in Shin et al. (2024). However, exposures may be subject to measurement error, which can lead to effect attenuation (see e.g. Chang et al., 2011). Mauff et al. (2017) and Wagner et al. (2021) addressed exposure measurement error in linear WCE models (similar to DLNs). Measurement error in non-linear models, such as the DRF-DLNM and ACE-DLNM, has not been studied and remains an important direction for future work.

The model and motivating analysis in this paper focus on a single pollutant. A natural extension is to accommodate multiple pollutants X_1, \dots, X_M using an additive model:

$$g(\mu_t) = f_1 \left\{ \int_0^{L_1} w_1(l) X_1(t-l) dl \right\} + \dots + f_M \left\{ \int_0^{L_M} w_M(l) X_M(t-l) dl \right\} + \sum_{j=1}^p h_j(z_{tj}).$$

We have implemented this in the R package `aceDLNMadditive`, available at github.com/tianyi-pan/aceDLNMadditive. However, this framework does not allow for interactions either among multiple exposures or between exposure and covariate z_{tj} . An important direction for future work is to extend the ACE-DLNM to allow for non-additive interactions, while retaining flexibility for general response types as well as smooth functions in large datasets, as in the present paper.

Acknowledgements

The authors gratefully acknowledge data stewardship and contribution: the Canadian Institute for Health Information (CIHI) for hospitalization data, and Environment and Climate Change Canada (ECCC) for air pollution and weather data. However, the analyses, conclusions, opinions, and statements expressed herein are those of the author, and not necessarily those of the data providers.

Supplementary Materials

The R package is available at <https://github.com/tianyi-pan/aceDLNM>. Code to reproduce the results in this paper is available at <https://github.com/tianyi-pan/aceDLNM-paper-code>.

Funding

This study was funded under “Canadian Environmental Sustainability Indicators” of Environment and Climate Change Canada and “Addressing Air Pollution Horizontal Initiative” of Health Canada (#AAPHI-859104; Principal Investigator, HH Shin).

Competing Interests

The authors also declare that they have no actual or potential competing financial interests, and that this study did not have any relationships or support that might be perceived as constituting a conflict of interest.

Data Availability

The air pollution and temperature datasets analyzed in this study are open to the public by Environment and Climate Change Canada (<http://data.ec.gc.ca/data/air/monitor/national-air-pollution-surveillance-naps-program/> and <https://climatedata.ca/>). The health data used for this study cannot be shared freely due to the policy of the CIHI for the use and distribution of sensitive records. Our data source, the Discharge Abstract Database (DAD), captures administrative, clinical, and demographic information on hospital discharges. Details regarding the DAD can be found at: <https://www.cihi.ca/en/discharge-abstract-database-metadata-dad>. The CIHI is the primary custodian of the DAD. CIHI is an independent, not-for-profit organization that provides essential information on Canada’s health systems and the health of people living in Canada. More information about CIHI can be found at: <https://www.cihi.ca/en/about-cihi>. Restrictions apply to the availability of the data as the data was used under a data sharing agreement and is not publicly available. General data inquiries about accessing CIHI data can be made at privacy@cihi.ca at the CIHI (<https://www.cihi.ca/en/access-data-and-reports/data-holdings/make-a-data-request>) or the author (hwashin.shin@hc-sc.gc.ca).

References

- J. M. Bernardo et al. Psi (digamma) function. *Applied Statistics*, 25(3):315–317, 1976.
- N. E. Breslow, J. H. Lubin, P. Marek, and B. Langholz. Multiplicative models and cohort analysis. *Journal of the American Statistical Association*, 78(381):1–12, 1983.
- W. S. Burr, G. Takahara, and H. H. Shin. Bias correction in estimation of public health risk attributable to short-term air pollution exposure. *Environmetrics*, 26(4):298–311, 2015.
- H. H. Chang, R. D. Peng, and F. Dominici. Estimating the acute health effects of coarse particulate matter accounting for exposure measurement error. *Biostatistics*, 12(4):637–652, 2011.
- R. Chen, P. Yin, X. Meng, C. Liu, L. Wang, X. Xu, J. A. Ross, L. A. Tse, Z. Zhao, H. Kan, et al. Fine particulate air pollution and daily mortality. A nationwide analysis in 272 Chinese cities. *American Journal of Respiratory and Critical Care Medicine*, 196(1):73–81, 2017.
- Y. Chen and R. J. Samworth. Generalized additive and index models with shape constraints. *Journal of the Royal Statistical Society Series B: Statistical Methodology*, 78(4):729–754, 2016.
- C. De Boor. *A practical guide to splines*, volume 27. springer-verlag New York, 1978.
- J. W. Demmel. *Applied numerical linear algebra*. SIAM, 1997.
- F. Dominici, R. D. Peng, M. L. Bell, L. Pham, A. McDermott, S. L. Zeger, and J. M. Samet. Fine particulate air pollution and hospital admission for cardiovascular and respiratory diseases. *Jama*, 295(10):1127–1134, 2006.
- P. K. Dunn and G. K. Smyth. Randomized quantile residuals. *Journal of Computational and Graphical Statistics*, 5(3):236–244, 1996.
- P. H. Eilers and B. D. Marx. Flexible smoothing with B-splines and penalties. *Statistical Science*, 11(2):89–121, 1996.
- Environment and Climate Change Canada. National air pollution surveillance program, Available from the Government of Canada Open Data Portal. open.canada.ca, 2021.
- Environment and Climate Change Canada. Canadian environmental sustainability indicators: Air health trends, 2022. Consulted on September 4, 2024. Available at: www.canada.ca/en/environment-climate-change/services/environmental-indicators/air-health-trends.html.
- Environment and Climate Change Canada. National climate data and information archive, 2024. Available at: <https://climate.weather.gc.ca/>.
- A. Gasparrini. Distributed lag linear and non-linear models in R: the package dlnm. *Journal of Statistical Software*, 43(8):1, 2011.

- A. Gasparrini. Distributed lag linear and non-linear models for time series data. *Document is available at R Project*, 2013.
- A. Gasparrini. Modeling exposure–lag–response associations with distributed lag non-linear models. *Statistics in Medicine*, 33(5):881–899, 2014.
- A. Gasparrini, B. Armstrong, and M. G. Kenward. Distributed lag non-linear models. *Statistics in Medicine*, 29(21):2224–2234, 2010.
- A. Gasparrini, F. Scheipl, B. Armstrong, and M. G. Kenward. A penalized framework for distributed lag non-linear models. *Biometrics*, 73(3):938–948, 2017.
- P. J. Green and B. W. Silverman. *Nonparametric regression and generalized linear models: a roughness penalty approach*. Crc Press, 1993.
- T. Hastie, R. Tibshirani, and J. H. Friedman. *The elements of statistical learning: data mining, inference, and prediction*, volume 2. Springer, 2009.
- M. Hauptmann, J. Wellmann, J. H. Lubin, P. S. Rosenberg, and L. Kreienbrock. Analysis of exposure-time-response relationships using a spline weight function. *Biometrics*, 56(4):1105–1108, 2000.
- E. Kong, H. Tong, and Y. Xia. Statistical modelling of nonlinear long-term cumulative effects. *Statistica Sinica*, 20(3):1097–1123, 2010.
- C. Lanczos. A precision approximation of the gamma function. *Journal of the Society for Industrial and Applied Mathematics, Series B: Numerical Analysis*, 1(1):86–96, 1964.
- A. M. M. Leal. autodiff, a modern, fast and expressive C++ library for automatic differentiation. <https://autodiff.github.io>, 2018. URL <https://autodiff.github.io>.
- C. Liu, R. Chen, F. Sera, A. M. Vicedo-Cabrera, Y. Guo, S. Tong, M. S. Coelho, P. H. Saldiva, E. Lavigne, P. Matus, et al. Ambient particulate air pollution and daily mortality in 652 cities. *New England Journal of Medicine*, 381(8):705–715, 2019.
- S. Ma. Estimation and inference in functional single-index models. *Annals of the Institute of Statistical Mathematics*, 68(1):181–208, 2016.
- K. Mauff, E. W. Steyerberg, G. Nijpels, A. A. van der Heijden, and D. Rizopoulos. Extension of the association structure in joint models to include weighted cumulative effects. *Statistics in Medicine*, 36(23):3746–3759, 2017.
- D. Mork and A. Wilson. Treed distributed lag nonlinear models. *Biostatistics*, 23(3):754–771, 2022.
- C. A. Pope, M. J. Thun, M. M. Namboodiri, D. W. Dockery, J. S. Evans, F. E. Speizer, C. W. Heath, et al. Particulate air pollution as a predictor of mortality in a prospective study of US adults. *American Journal of Respiratory and Critical Care Medicine*, 151(3):669–674, 1995.

- H. Powell, J. R. Krall, Y. Wang, M. L. Bell, and R. D. Peng. Ambient coarse particulate matter and hospital admissions in the medicare cohort air pollution study, 1999–2010. *Environmental Health Perspectives*, 123(11):1152–1158, 2015.
- J. Schwartz. The distributed lag between air pollution and daily deaths. *Epidemiology*, 11(3):320–326, 2000.
- H. H. Shin, P. Gogna, A. Maquiling, R. P. Parajuli, L. Haque, and B. Burr. Comparison of hospitalization and mortality associated with short-term exposure to ambient ozone and PM_{2.5} in Canada. *Chemosphere*, 265:128683, 2021.
- H. H. Shin, J. Owen, A. Maquiling, R. P. Parajuli, and M. Smith-Doiron. Circulatory health risks from additive multi-pollutant models: short-term exposure to three common air pollutants in Canada. *Environmental Science and Pollution Research*, 30(6):15740–15755, 2023.
- H. H. Shin, J. Owen, A. O. Delic, M. Kabasakal, and S. Buteau. Modifying factors and temporal trends of adverse health effects of short-term exposure to PM_{2.5} in Canada (2001–2018). *Science of the Total Environment*, 955:177046, 2024.
- A. Stringer. Identifiability constraints in generalized additive models. *Canadian Journal of Statistics*, 2023.
- A. Stringer, T. Akkaya Hocagil, R. J. Cook, L. M. Ryan, S. W. Jacobson, and J. L. Jacobson. Semi-parametric benchmark dose analysis with monotone additive models. *Biometrics*, 80(3):ujae098, 2024.
- M.-P. Sylvestre and M. Abrahamowicz. Flexible modeling of the cumulative effects of time-dependent exposures on the hazard. *Statistics in Medicine*, 28(27):3437–3453, 2009.
- D. C. Thomas. Models for exposure-time-response relationships with applications to cancer epidemiology. *Annual Review of Public Health*, 9(1):451–482, 1988.
- T. T. Truong, T. D. To, H.-T. Nguyen, T. H. Nguyen, H. P. Nguyen, and M. Helmy. A fast and simple modification of Newton’s method avoiding saddle points. *Journal of Optimization Theory and Applications*, 199(2):805–830, 2023.
- M. Wagner, F. Grodstein, K. Leffondre, C. Samieri, and C. Proust-Lima. Time-varying associations between an exposure history and a subsequent health outcome: a landmark approach to identify critical windows. *BMC Medical Research Methodology*, 21:1–15, 2021.
- Y. Wang, A. Ghassabian, B. Gu, Y. Afanasyeva, Y. Li, L. Trasande, and M. Liu. Semi-parametric distributed lag quantile regression for modeling time-dependent exposure mixtures. *Biometrics*, 79(3):2619–2632, 2023.
- A. Wilson, H.-H. L. Hsu, Y.-H. M. Chiu, R. O. Wright, R. J. Wright, and B. A. Coull. Kernel machine and distributed lag models for assessing windows of susceptibility to environmental mixtures in children’s health studies. *The Annals of Applied Statistics*, 16(2):1090–1110, 2022.

- S. Wood. Package ‘mgcv’. *R package version*, 1(29):729, 2015.
- S. N. Wood. Fast stable restricted maximum likelihood and marginal likelihood estimation of semiparametric generalized linear models. *Journal of the Royal Statistical Society: Series B (Statistical Methodology)*, 73(1):3–36, 2011.
- S. N. Wood. *Generalized additive models: an introduction with R*. CRC press, 2017a.
- S. N. Wood. P-splines with derivative based penalties and tensor product smoothing of unevenly distributed data. *Statistics and Computing*, 27:985–989, 2017b.
- S. N. Wood, N. Pya, and B. Säfken. Smoothing parameter and model selection for general smooth models. *Journal of the American Statistical Association*, 111(516):1548–1563, 2016.
- S. N. Wood, Z. Li, G. Shaddick, and N. H. Augustin. Generalized additive models for gigadata: modeling the UK black smoke network daily data. *Journal of the American Statistical Association*, 112(519):1199–1210, 2017.
- World Health Organization. International classification of diseases, 10th revision, 2019. Available at: <https://icd.who.int/browse10/2019/en>.
- M. Yuan. On the identifiability of additive index models. *Statistica Sinica*, pages 1901–1911, 2011.
- A. Zanobetti, M. Wand, J. Schwartz, and L. Ryan. Generalized additive distributed lag models: quantifying mortality displacement. *Biostatistics*, 1(3):279–292, 2000.

Appendix

Web Appendix A	DRF-DLNM	25
Web Appendix B	Interpolation using Cubic B-spline	25
Web Appendix C	Integration for Adaptive Cumulative Exposures	28
Web Appendix D	Identifiability	30
Web Appendix D.1	Review of Identifiability Constraints	30
Web Appendix D.2	Constraints and Identifiability Proposition 1	31
Web Appendix D.3	Reparameterization	33
Web Appendix E	Optimization Algorithm	33
Web Appendix E.1	Newton Step	35
Web Appendix F	Derivative Computation	35
Web Appendix F.1	Derivative of \mathcal{L}	36
Web Appendix F.2	Derivative of \mathbf{Q}	38
Web Appendix F.3	Derivative of $\mathcal{L}_{\text{LA}}^*$	39
Web Appendix G	Delta Method	40
Web Appendix H	Simulations	41
Web Appendix H.1	Data-Generation Details	41
Web Appendix H.2	Additional Simulation Results	43
Web Appendix H.3	Supplementary Simulation: Linear f	55
Web Appendix H.4	Supplementary Simulation: Misspecification	56
Web Appendix I	Canadian Air Pollution Data	59
Web Appendix I.1	Data Summary	59
Web Appendix I.2	Additional Application Results	60
Web Appendix I.3	Sensitivity to the Bounds of ACE	76
Web Appendix I.4	Sensitivity to the Initial Values	77
Web Appendix I.5	Negative Binomial and Poisson Distribution	78

Web Appendix A DRF-DLNM

In this Web Appendix, we review the DRF-DLNMs. The DRF-DLNM proposed by Gasparrini et al. (2010) and Gasparrini (2014) is specified as

$$g(\mu_t) = \sum_{l=0}^{L-1} \psi(x_{t-l}, l) + \sum_{j=1}^p h_j(z_{tj}),$$

where $\psi(\cdot, \cdot)$ is a bivariate exposure-lag-response function, modelled by splines and expressed as a linear combination of spline coefficients through a cross-basis expansion. The fitting of the model is convenient using the packages `dlnm` (Gasparrini, 2011) and `mgcv` (Wood, 2015). Gasparrini et al. (2017) proposed a penalized framework, where the penalty matrices \mathbf{S}_x and \mathbf{S}_l along with smoothing parameters λ_x and λ_l are imposed on the two dimensions of the exposure-lag-response function. The framework supports various types of smoothers, and the model referred to as the “primary” model in Gasparrini et al. (2017) is based on P-splines (Eilers and Marx, 1996), where difference penalties are applied to the spline coefficients. In our paper, all DRF-DLNMs are fitted with the P-spline model.

A similar model based on splines is described in Chapter 7.4.2 in Wood (2017a) and can be fitted by tensor product splines via “summation convention” in `mgcv`. Mork and Wilson (2022) proposed a DRF-DLNM based on the Bayesian additive regression tree to relax the smoothness constraint and impose monotone constraints on weight functions.

The interpretations of the DRF-DLNM rely on *post-hoc* summary statistics, including the exposure-response curve at a specific lag, the lag-response curve at a specific exposure level, and the overall cumulative risk for a specific exposure history (Gasparrini, 2014).

Web Appendix B Interpolation using Cubic B-spline

The continuous exposure process X is obtained by interpolating the collected exposure x_t using the cubic spline. Green and Silverman (1993) proposed an approach to specify the spline through its values and second-order derivatives at the observed points. It is computationally efficient, but has some limitations, including numerical instability, among others; see Chapter 3.6 in Green and Silverman (1993). One popular solution is the basis expansion approach, which is appealing in stability and flexibility.

In this Web Appendix, we represent X by cubic B-spline basis expansion and present a least-square-based approach to obtain the spline coefficient. This approach has a computational complexity $O(N)$, the same as that of the approach in Green and Silverman (1993), and is easier to implement and can take advantage of the B-spline basis expansion.

We will first describe the cubic B-spline, and then introduce the least-square-based approach, along with a discussion on the computational complexity.

Let $b_{l,p}(x)$ be the l^{th} B-spline function of order p , where $l = 1, \dots, K$. The knots sequence is denoted as $\tau = [\tau_1, \tau_2, \dots, \tau_{K+p}]$. Let ξ_l and ξ_u , $\xi_l \leq \xi_u$, be the boundaries defining the domain where we evaluate the B-splines. $\tau_1 \leq \tau_2 \leq \dots \leq \tau_p \leq \xi_l$ and $\xi_u \leq \tau_{K+1} \leq \tau_{K+2} \leq \dots \leq \tau_{K+p}$ are the auxiliary knots with arbitrary values beyond the boundaries. The knots within the boundary $\tau_{p+1} \leq \dots \leq \tau_K$ are interior knots. The B-spline function $b_{l,p}(x)$ is defined recursively and locally supported in (τ_l, τ_{l+p}) .

The s -order derivative of $b_{l,p}(x)$ is given by

$$\frac{d^{(s)}b_{l,p}(x)}{dx^{(s)}} = (p-1) \left(\frac{d^{(s-1)}b_{l,p-1}(x)/dx^{(s-1)}}{\tau_{l+p-1} - \tau_l} - \frac{d^{(s-1)}b_{l+1,p-1}(x)/dx^{(s-1)}}{\tau_{l+p} - \tau_{l+1}} \right). \quad (\text{S.4})$$

See more details in Wood (2017a). Using $p = 4$ for cubic B-spline, we ignore the subscript p to simplify the notation to $b_l(x)$.

A cubic spline is a *natural cubic spline*, if the additional constraint is added: the function is linear beyond the boundary ξ_l and ξ_u . The interpolating natural cubic spline g is optimal, namely g is the unique function minimizing the roughness $\int g''^2$ among all smooth functions that interpolate the data; see Green and Silverman (1993) for details.

In the ACE-DLNM, we treat the exposure process $X(t)$ continuously. Without loss of generality, assume $\mathcal{T}^x = \mathcal{T}$. Let $\{t - 0.5, x_t\}, t \in \mathcal{T} = \{1, 2, \dots, N\}$ denote the data. We propose to interpolate the discrete data using the natural cubic spline. The exposure process is modelled as

$$X(t) = \sum_{q=1}^{k^x} b_q^x(t) \alpha_q^x,$$

where $b_q^x(t)$ are cubic B-splines and α_q^x are spline coefficients. We denote $\mathbf{b}^x(t) = [b_1^x(t), \dots, b_{k^x}^x(t)]^\top$ and $\boldsymbol{\alpha}^x = [\alpha_1^x, \dots, \alpha_{k^x}^x]^\top$.

We set N interior knots $\{\tau_5, \tau_6, \dots, \tau_{N+4}\}$ at observed time points $\{0.5, 1.5, \dots, N - 0.5\}$ with corresponding observations $\{x_1, x_2, \dots, x_N\}$, and hence $k^x = N + 4$. For the auxiliary knots beyond the boundary, we set $\tau_1 = \tau_5 - c - 1$, $\tau_2 = \tau_3 = \tau_4 = \tau_5 - c$ and $\tau_{N+5} = \tau_{N+6} = \tau_{N+7} = \tau_N + c$, $\tau_{N+8} = \tau_N + c + 1$, where $c > 0$ is arbitrary. We place the empty points, i.e. setting values as 0, on the auxiliary knots, as shown in Web Table 1.

Web Table 1. The knots and the corresponding values. The interior knots $\tau_5 \dots \tau_{N+4}$ are set at observed time points. The empty points (assuming observed data are zero) are added at the auxiliary knots $\tau_1, \dots, \tau_4, \tau_{N+5}, \dots, \tau_{N+8}$.

Value	0	...	0	x_1	...	x_N	0	...	0
Knot	τ_1	...	τ_4	τ_5	...	τ_{N+4}	τ_{N+5}	...	τ_{N+8}

The B-splines evaluated at the interior knots are represented as a matrix \mathbf{B}^x with l^{th} row as $\mathbf{b}^x(l)^\top$, $l = 1, \dots, N$. Define $\tilde{\mathbf{B}}^x$ as the B-spline evaluated at both interior and auxiliary knots, i.e.,

$$\tilde{\mathbf{B}}^x = [\mathbf{b}^x(\tau_1) \quad \dots \quad \mathbf{b}^x(\tau_4) \quad \mathbf{B}^{x^\top} \quad \mathbf{b}^x(\tau_{N+5}) \quad \dots \quad \mathbf{b}^x(\tau_{N+8})]^\top.$$

Denote the observed exposure as $\mathbf{X} = [x_1, \dots, x_N]^\top$ and the vector with the empty points as $\tilde{\mathbf{X}} = [0, 0, 0, 0, \mathbf{X}^\top, 0, 0, 0, 0]^\top$. We propose to obtain the spline coefficients $\boldsymbol{\alpha}^x = [\alpha_1^x, \dots, \alpha_{N+4}^x]$ by

$$\boldsymbol{\alpha}^x = \left(\tilde{\mathbf{B}}^{x^\top} \tilde{\mathbf{B}}^x \right)^{-1} \tilde{\mathbf{B}}^{x^\top} \tilde{\mathbf{X}}. \quad (\text{S.5})$$

Then, we have the following property:

Property B.1. *The cubic B-spline $X(t) = \sum_{q=1}^{N+4} b_q^x(t) \alpha_q^x$ interpolates the data, if the spline coefficients α_q^x are computed from Equation S.5.*

Proof of Property B.1. According to Theorem 2.2 in Green and Silverman (1993), for the observed data $\{t, x_t\}, t = 1, 2, \dots, N$, there exists a *unique* natural cubic spline with interior knots at $t = 1, 2, \dots, N$ interpolating the observed data.

Assume that the spline coefficient of the interpolating natural cubic spline is α^{*x} . Then, we have, $\sum_{t=1}^N (x_t - \mathbf{b}^x(t)^\top \alpha^{*x})^2 = 0$.

By the property of natural cubic spline, the function is linear beyond the boundary. Hence, for any $z \in (\tau_1, \tau_2)$, $\mathbf{b}^{x''}(z)^\top \alpha^{*x} = 0$, where $\mathbf{b}^{x''}$ is the second derivative of B-splines. Applying the formula of derivative of B-spline (Equation S.4) and the local support property, we have $b_1^{x''}(z) > 0$ and $b_k^{x''}(z) = 0$ for $k \geq 2$, which leads to, $\alpha_1^{*x} = 0$. Similarly, we have $\alpha_{N+4}^{*x} = 0$.

Defining $\mathbf{v} = [v_1, \dots, v_{N+4}]^\top$ and a function of \mathbf{v} as follows

$$L(\mathbf{v}) = \sum_{t=1}^N (x_t - \mathbf{b}^x(t)^\top \mathbf{v})^2 + 3v_1^2 + 3v_{N+4}^2.$$

Then, $L(\alpha^{*x}) = 0$, i.e., α^{*x} as minimizer of the function $L(\mathbf{v}) \geq 0$.

From the induction definition of B-spline (Wood, 2017a), we have $\mathbf{b}^x(\tau_1) = [0, 0, \dots, 0]^\top$, $\mathbf{b}^x(s) = [1, 0, \dots, 0]^\top$ for $s = \tau_2, \tau_3, \tau_4$, $\mathbf{b}^x(s) = [0, \dots, 0, 1]^\top$ for $s = \tau_{N+5}, \tau_{N+6}, \tau_{N+7}$, and $\mathbf{b}^x(\tau_{N+8}) = [0, \dots, 0, 0]^\top$. Therefore, $L(\mathbf{v})$ can be rewritten as

$$\begin{aligned} L(\mathbf{v}) &= \sum_{t=1}^N (x_t - \mathbf{b}^x(t)^\top \mathbf{v})^2 + \sum_{s \in \{\tau_1, \dots, \tau_4, \tau_{N+5}, \dots, \tau_{N+8}\}} (0 - \mathbf{b}^x(s)^\top \mathbf{v})^2 \\ &= (\widetilde{\mathbf{X}} - \widetilde{\mathbf{B}}^x \mathbf{v})^\top (\widetilde{\mathbf{X}} - \widetilde{\mathbf{B}}^x \mathbf{v}). \end{aligned}$$

Minimizing $L(\mathbf{v})$ turns to a least-square problem. The solution is

$$\arg \min_{\mathbf{v}} L(\mathbf{v}) = (\widetilde{\mathbf{B}}^{x\top} \widetilde{\mathbf{B}}^x)^{-1} \widetilde{\mathbf{B}}^{x\top} \widetilde{\mathbf{X}}.$$

Therefore, we have $\alpha^{*x} = (\widetilde{\mathbf{B}}^{x\top} \widetilde{\mathbf{B}}^x)^{-1} \widetilde{\mathbf{B}}^{x\top} \widetilde{\mathbf{X}}$, which completes the proof. \square

By setting knots at observed points $t = 1, 2, \dots, N$, there are other approaches to obtain the interpolating natural cubic spline; see Green and Silverman (1993) for an example. According to Theorem 2.2 in Green and Silverman (1993), for the observed data $\{t, x_t\}, t = 1, 2, \dots, N$, all the possible approaches yield the same interpolating natural cubic spline. Here we propose the least-square-type approach that is easier to implement and can take advantage of the basis expansion form, as discussed before.

Solving the least-square-type equation requires $O(N^3)$ computational operations. Note that $\widetilde{\mathbf{B}}^x$ is a banded sparse matrix because of the local support property of B-splines. The equation is solved efficiently using the sparse Cholesky decomposition. With the techniques, the computational complexity reduces to $O(N)$; see also Chapter 5 in Hastie et al. (2009).

Web Appendix C Integration for Adaptive Cumulative Exposures

Define $D_q(t) = \int_0^L b_q^w(l)X(t-l)dl$. To construct the ACE, we need to evaluate the integral $D_q(t)$ for $q = 1, 2, \dots, d^w$ and each t . We propose the following approach to fast and exactly evaluate these integrals using de Boor's algorithm (De Boor, 1978) and an appropriate modification of the method given by Wood (2017b).

Wood (2017b) proposed an algorithm to compute the integral $\int b_i(x)b_j(x)dx$ where b_i and b_j are B-splines sharing the same knots sequence. The algorithm is fast and implemented in `mgcv` package. In our settings, however, the knot sequences for b_q^w and X are different. Meanwhile, the intervals of integration for different t are overlapped, and hence some evaluations are redundant. We propose a modification of Wood (2017b) algorithm.

We highlight the key steps in the modifications. First, we merge and resort the two different knot sequences to a unified knot sequence within $[t-L, t]$. Second, in each partition based on the knots sequence, Wood (2017b) solves a linear system to obtain the polynomial coefficients. In our settings, some polynomial coefficients hold the same. We propose to solve the coefficients in advance to avoid redundant calculations. The details are described as follows.

Denote $\boldsymbol{\tau}^w = [\tau_1^w, \dots, \tau_{d^w+4}^w]$ the knots for b_q^w and $\boldsymbol{\tau}^x = [\tau_1^x, \dots, \tau_{d^x+4}^x]$ the knots for X . We merge the sequences $t - \boldsymbol{\tau}^w = [t - \tau_1^w, \dots, t - \tau_{d^w+4}^w]$ and $\boldsymbol{\tau}^x$ into one sequence $\boldsymbol{\tau}_t$, i.e. $\boldsymbol{\tau}_t = \{t - \boldsymbol{\tau}^w, \boldsymbol{\tau}^x\}$. Denote $[m_{ts}, n_{ts}]$ the intervals that partition the line $(t-L, t-0)$ based on $\boldsymbol{\tau}_t$. The spline functions b_q^w and X are cubic polynomial function within $[m_{ts}, n_{ts}]$. Following Wood (2017b), we have

$$\begin{aligned} D_q(t) &= \sum_s \int_{m_{ts}}^{n_{ts}} b_q^w(l)X(t-l)dl \\ &= \sum_s \frac{m_{ts} - n_{ts}}{2} \int_{-1}^1 \sum_{i=0}^3 c_i x^i \sum_{j=0}^3 d_j x^j dx, \end{aligned}$$

where c_i and d_j are polynomial coefficients. The polynomial coefficients \mathbf{c} are obtained by solving $\mathbf{P}\mathbf{c} = \mathbf{b}^w$ where $P_{ij} = (-1 + 2(i-1)/3)^{j-1}$ and \mathbf{b}^w consists of b_q^w evaluated at the 4 points evenly spaced from a_{ts} to b_{ts} , that is,

$$\mathbf{b}^w = [b_q^w(a_{ts}), b_q^w(a_{ts}) + (b_{ts} - a_{ts})/3, b_q^w(a_{ts}) + 2(b_{ts} - a_{ts})/3, b_q^w(b_{ts})]^\top.$$

Similarly, \mathbf{d} are obtained by solving $\mathbf{P}\mathbf{d} = \mathbf{b}^x$. Therefore, we have

$$D_q(t) = \sum_s \frac{m_{ts} - n_{ts}}{2} \mathbf{b}^{x\top} \mathbf{P}^{-\top} \mathbf{H} \mathbf{P}^\top \mathbf{b}^w,$$

where $H_{ij} = (1 + (-1)^{i+j-2})/(i+j-1)$.

For the second aspect of modification about solving the linear systems for each s , the polynomial coefficients hold the same within the adjacent knots. In our algorithm, we propose to solve the coefficients in advance to avoid redundant calculations. For two adjacent knots τ_s^x and τ_{s+1}^x , for example, we calculate the matrix \mathbf{K} where $K_{ij} = (\tau_s^x + (i-1)(\tau_{s+1}^x - \tau_s^x)/3)^{j-1}$, and evaluate \mathbf{b}^x at the 4 points evenly spaced from τ_s^x to τ_{s+1}^x . Then,

we can obtain the coefficient \mathbf{d} for the two adjacent knots τ_s^x and τ_{s+1}^x by solving $\mathbf{K}\mathbf{d} = \mathbf{b}^x$. Then, \mathbf{d} is the common coefficient for any $[m_{ts}, n_{ts}]$ within τ_s^x and τ_{s+1}^x , and hence we do not need to solve $\mathbf{P}\mathbf{d} = \mathbf{b}^x$ redundantly.

Furthermore, X is modelled by interpolating cubic B-spline $X(t) = \sum_{q=1}^{k^x} b_q^x(t)\alpha_q^x$ with a large number of knots, which will induce a further computational burden. In fact, only 4 of the basis functions are non-zero for each t . To avoid wasteful evaluation, we use de Boor's Algorithm (De Boor, 1978) to increase the computational efficiency.

The full details of the algorithm are in Algorithm 1. The algorithm is implemented using cpp code available at the R package file <https://github.com/tianyi-pan/aceDLNM/blob/main/src/helpers.cpp>.

Algorithm 1 Evaluate the integral in weighted exposures

- 1: Define $I_\tau(x)$ as a function returning the index of the largest knot smaller than x in τ .
 - 2: Calculate \mathbf{P} where $P_{ij} = (-1 + 2(i-1)/3)^{j-1}$, and solve \mathbf{P}^{-1} .
 - 3: Calculate \mathbf{H} where $H_{ij} = (1 + (-1)^{i+j-2})/(i+j-1)$.
 - 4: Calculate $\mathbf{W} = \mathbf{P}^{-1\top} \mathbf{H} \mathbf{P}^{-1}$.
 - 5: **for** $r = 1, \dots, d^x + 3$ **do**
 - 6: $h_r^x = \tau_{r+1}^x - \tau_r^x$
 - 7: Evaluate $\mathbf{b}_r^x = [X(\tau_r^x), X(\tau_r^x + h_r^x/3), X(\tau_r^x + 2h_r^x/3), X(\tau_{r+1}^x)]^\top$ using de Boor's algorithm.
 - 8: Calculate \mathbf{K}^x where $K_{ij}^x = (\tau_r^x + h_r^x(i-1)/3)^{j-1}$.
 - 9: Solve the linear system $\mathbf{K}^x \mathbf{d}_r^x = \mathbf{b}_r^x$ for the polynomial coefficients \mathbf{d}_r^x .
 - 10: **end for**
 - 11: Save $\mathbf{b}_1^x, \dots, \mathbf{b}_{d^x+3}^x$ and $\mathbf{d}_1^x, \dots, \mathbf{d}_{d^x+3}^x$.
 - 12: Similarly, obtain and save $\mathbf{b}_1^w, \dots, \mathbf{b}_{d^w+3}^w$ and $\mathbf{d}_1^w, \dots, \mathbf{d}_{d^w+3}^w$.
 - 13: **for** $t = 1, \dots, N$ **do**
 - 14: Set $D_q(t) = 0$.
 - 15: **for** $u = 1, \dots, d^w + 3$ **do**
 - 16: $h_u^w = \tau_{u+1}^w - \tau_u^w$
 - 17: **if** $I_{\tau^x}(t - \tau_u^w) = I_{\tau^x}(t - \tau_{u+1}^w)$ **then**
 - 18: Calculate \mathbf{K}^x , where $K_{ij}^x = (t - \tau_{u+1}^w + (i-1)h_u^w/3)^{j-1}$.
 - 19: $D_q(t) = D_q(t) + (h_u^w/2)[\mathbf{K}^x \mathbf{d}_{I_{\tau^x}(t - \tau_u^w)}^x]^\top \mathbf{W} \mathbf{b}_u^w$.
 - 20: **else**
 - 21: Define τ^u as a sequence with the first element $t - \tau_{u+1}^w$ and the last element $t - \tau_u^w$. The elements in the middle are the knots of X within $I_{\tau^x}(t - \tau_{u+1}^w)$ and $I_{\tau^x}(t - \tau_u^w)$.
 - 22: **for** $s = 1, \dots, (\text{length of } \tau^u - 1)$ **do**
 - 23: $h_s^u = \tau_{s+1}^u - \tau_s^u$.
 - 24: Calculate \mathbf{K}^x , where $K_{ij}^x = (\tau_s^u + (i-1)h_s^u/3)^{j-1}$.
 - 25: Calculate \mathbf{K}^w , where $K_{ij}^w = (t - \tau_s^u - (i-1)h_s^u/3)^{j-1}$.
 - 26: $D_q(t) = D_q(t) + (h_s^u/2)[\mathbf{K}^x \mathbf{d}_{I_{\tau^x}(\tau_s^u)}^x]^\top \mathbf{W} [\mathbf{K}^w \mathbf{d}_u^w]$.
 - 27: **end for**
 - 28: **end if**
 - 29: **end for**
 - 30: **end for**
-

Web Appendix D Identifiability

Recall that the mean model in ACE-DLNM is

$$g(\mu_t) = f \left\{ \int_0^L w(l)X(t-l)dl \right\} + \sum_{j=1}^p h_j(z_{tj}).$$

Let $\mathbf{h}(\mathbf{z}_t) = \sum_{j=1}^p h_j(z_{tj})$ and $s(t; X) = f \left\{ \int_0^L w(l)X(t-l)dl \right\}$.

Given a known exposure process X , assuming that there exist two sets $\{\tilde{s}, \tilde{\mathbf{h}}\}$ and $\{s^*, \mathbf{h}^*\}$, where $\tilde{s}(t) = \tilde{f} \left\{ \int_{l_0}^L \tilde{w}(l)X(t-l)dl \right\}$ and $s^*(t) = f^* \left\{ \int_{l_0}^L w^*(l)X(t-l)dl \right\}$, such that,

$$\tilde{s}(t, X) + \tilde{\mathbf{h}}(\mathbf{z}_t) = s^*(t, X) + \mathbf{h}^*(\mathbf{z}_t) \quad (\text{S.6})$$

for all t and \mathbf{z}_t . Following the discussions of identifiability in Yuan (2011) and Chen and Samworth (2016), the ACE-DLNM is identifiable if Equation S.6 implies that $\tilde{f} = f^*$, $\tilde{w} = w^*$ and $\tilde{\mathbf{h}} = \mathbf{h}^*$.

The ACE-DLNM is reduced to a GAM if $s(t; X)$ is viewed as a function of t . The discussion on the identifiability of GAMs under linear constraints can be found in Wood et al. (2016) and Stringer (2023). Under some linear constraint, Equation S.6 implies that $\tilde{s} = s^*$ and $\tilde{\mathbf{h}} = \mathbf{h}^*$. To show the identifiability, we need to show that the following Proposition 2 is true.

Proposition 2. $\tilde{s} = s^*$ implies $\tilde{f} = f^*$ and $\tilde{w} = w^*$.

Let $\tilde{w}(z) = c \cdot w^*(z)$ and $\tilde{f}(z) = f^*(z/c)$, $c \in \mathbb{R} \setminus \{1\}$, and hence $\{\tilde{f}, \tilde{w}\} \neq \{f^*, w^*\}$; but it is obvious that $\tilde{s} = s^*$. Therefore, Proposition 2 is false and the model is not identifiable.

The constraints preventing the arbitrary $c \in \mathbb{R} \setminus \{1\}$ are required.

Web Appendix D.1 Review of Identifiability Constraints

We review the constraints used in existing models, including Kong et al. (2010), Ma (2016), Wilson et al. (2022) and Wang et al. (2023). In Web Table 2, we summarize the imposed constraints, and some information about the constraints including whether or not (1) the constraints are continuous (Continuous), (2) the bounds for ACE $E(t)$ are derived (Bounds for $E(t)$), (3) the constraints are fully absorbed by reparameterization (Absorbed by Reparameterization), and (4) the identifiability theorem/proposition was introduced (Proposition of Identifiability). We use the continuous constraints in Wilson et al. (2022) and address these issues simultaneously.

Web Table 2. A review of identifiability constraints.

Paper	Constraint 1	Constraint 2	Continuous	Bounds for $E(t)$	Absorbed by Reparameterization	Proposition of Identifiability
Our Paper	$\int w^2(l)dl = 1$	$\int w(l)dl > 0$	✓	✓	✓	✓
Kong et al. (2010)	$\int w(l)dl = 1$	$E(\int X(t-l)w(l)dl) = 0$	✓		✓	✓
Ma (2016)	$\sum_{m=1}^M \int w_k^2(l)dl = 1^1$	monotone functions ²	✓			✓
Wilson et al. (2022)	$\int w^2(l)dl = 1$	$\int w(l)dl > 0$	✓			
Wang et al. (2023)	$\sum_j (\alpha_j^w)^2 = 1$	$\alpha_1^w > 0$			✓	

¹ The model is for multiple X , and $E(t)$ is written as $f(\int \sum_{m=1}^M X_m(t-l)w_m(l)dl)$. ² $w_1(\cdot)$ is non-constant and monotone nondecreasing, or $f(\cdot)$ is monotone nondecreasing.

Web Appendix D.2 Constraints and Identifiability Proposition 1

Recall the two identifiability constraints described in Section 2.3:

Constraint 1 (Scale Constraint): $\int_0^L w(l)^2 dl = 1$,

Constraint 2 (Sign Constraint): $\int_0^L w(l) dl > 0$.

We assume the following Conditions:

- (a) X is continuous and non-constant on its domain. $X(t)$ can be represented with a B-spline basis expansion, $X(t) = \sum_{q=1}^{k_x} b_q^x(t)\alpha_q^x$, where $b_q^x(\cdot)$ are cubic B-spline functions and α_q^x are spline coefficients with some knot sequence.
- (b) f is continuously differentiable and non-constant on the range of $E(t)$.
- (c) w is continuous on $[0, L]$.

Next, we prove Proposition 1 in Section 2.3.

Proof of Proposition 1. To prove Proposition 1, we show that there exists a knot sequence such that Proposition 2 is true under the scale and sign constraints and Conditions (a), (b) and (c).

Assume there exist two sets $\{\tilde{f}, \tilde{w}\}$ and $\{f^*, w^*\}$, such that,

$$\tilde{f} \left\{ \int_0^L \tilde{w}(l)X(t-l)dl \right\} = f^* \left\{ \int_0^L w^*(l)X(t-l)dl \right\}, \quad (\text{S.7})$$

for all t . Define $\tilde{E}(t) = \int_0^L \tilde{w}(l)X(t-l)dl$ and $E^*(t) = \int_0^L w^*(l)X(t-l)dl$. Condition (a) and the range of $E(t)$ ensure the existence of the two integrals. To show Proposition 1 is true, we need to show that $\tilde{f} = f^*$ and $\tilde{w} = w^*$.

By Condition (a), $X(t) = \sum_{q=1}^{k_x} b_q^x(t)\alpha_q^x$. For $q \in [1, 2, \dots, k_x]$, taking derivatives w.r.t. α_q^x on both sides of Equation S.7 leads to

$$\tilde{f}' \left\{ \tilde{E}(t) \right\} \int_0^L b_q^x(t-l)\tilde{w}(l)dl = f^{*'} \left\{ E^*(t) \right\} \int_0^L b_q^x(t-l)w^*(l)dl, \quad (\text{S.8})$$

where $\tilde{f}'(z)$ and $f^{*'}(z)$ are the derivatives w.r.t z , which exist by Condition (b). Then, we take summation over $q = 1, 2, \dots, N$, which yields

$$\tilde{f}' \{ \tilde{E}(t) \} \int_0^L \tilde{w}(l) dl = f^{*'} \{ E^*(t) \} \int_0^L w^*(l) dl, \quad (\text{S.9})$$

using the property of B-spline, $\sum_{q=1}^{k_x} b_q^x(z) = 1$.

We have $\int_0^L w^*(l) dl > 0$ and $\int_0^L \tilde{w}(l) dl > 0$ by sign constraint. There exists some t such that $f^{*'} \{ E^*(t) \} \neq 0$ and $\tilde{f}' \{ \tilde{E}(t) \} \neq 0$ by Condition (b). For such t , we combine Equation S.8 and S.9, which leads to

$$\frac{\int_0^L b_q^x(t-l) \tilde{w}(l) dl}{\int_0^L \tilde{w}(l) dl} = \frac{\int_0^L b_q^x(t-l) w^*(l) dl}{\int_0^L w^*(l) dl}. \quad (\text{S.10})$$

Define $\tilde{r}(l) = \tilde{w}(l) / \int_0^L \tilde{w}(l) dl$ and $r^*(l) = w^*(l) / \int_0^L w^*(l) dl$. Equation S.10 is rewritten as

$$\int_0^L b_q^x(t-l) \{ \tilde{r}(l) - r^*(l) \} dl = 0, \quad (\text{S.11})$$

for all t and any $q \in [1, 2, \dots, k_x]$.

From Equation S.11, we claim that $\tilde{r} = r^*$ almost everywhere, which will be proved later.

Based on this claim, we have $\tilde{w}(l) = c \cdot w^*(l)$ almost everywhere, where $c = \int_0^L w^*(l) dl / \int_0^L \tilde{w}(l) dl$. By scale constraint and sign constraint, we have $c = 1$. Hence, $\tilde{w} = w^*$. Back to Equation S.7, for any t , we have

$$\tilde{f} \{ E^*(t) \} = f^* \{ E^*(t) \},$$

which leads to $\tilde{f} = f^*$.

Next, we prove the claim, $\tilde{r} = r^*$ a.e., by contradiction:

Suppose $\tilde{r}(l_1) - r^*(l_1) = 0$, a.e. is not true. Since \tilde{w} and w^* are continuous (Condition (c)) and hence \tilde{r}, r^* are continuous, there exists an interval $[a, b] \in [0, L]$ such that $\tilde{r}(l_1) - r^*(l_1), l_1 \in [a, b]$ are nonzero with the same sign. Assume $\tilde{r}(l_1) - r^*(l_1) > 0$ without loss of generality. Then, we can find a knot sequence $\boldsymbol{\tau}$ such that there exists a t_1 and an index j , $\tau_j \geq t_1 - b$ and $\tau_{j+4} \leq t_1 - a$. By the property of cubic B-spline, b_j^x is locally supported in (τ_j, τ_{j+4}) with positive values. Therefore, we have

$$\int_0^L b_j^x(t_1-l) \{ \tilde{r}(l) - r^*(l) \} dl = \int_a^b b_j^x(t_1-l) \{ \tilde{r}(l) - r^*(l) \} dl > 0,$$

which is contradicted by Equation S.11. The claim is proved, and the proof of Proposition 1 is complete. \square

Remark 1. Conditions (b) and (c) are ready if f and w can be modelled by cubic B-splines. For Condition (a), the continuous exposure process X is obtained by interpolating the observed data using a cubic B-spline, which ensures continuity, and the non-constancy of X can be easily verified.

Web Appendix D.3 Reparameterization

In Section 3.1, we present the reparameterization for w . In the reparameterization, the sequence $\{l_j\}_{j=1}^J$ is an evenly spaced partition of $[0, L]$. We replace $\int_0^L w^+(l) dl$ by $(L/J) \sum_{j=1}^J w^+(l_j)$ with a large J , which leads to $\int_0^L w(l) dl = \alpha_1^{w+}$. Then, we have

$$\alpha_1^{w+} = \frac{1}{([1, \phi^{w\top}] \mathbf{C} [1, \phi^{w\top}]^\top)^{1/2}} > 0.$$

Therefore, the sign constraint $\int_0^L w(l) dl > 0$ is guaranteed. By the definition of \mathbf{C} , we have

$$\int_0^L w(l)^2 dl = \boldsymbol{\alpha}^{w+\top} \mathbf{C} \boldsymbol{\alpha}^{w+},$$

where $\boldsymbol{\alpha}^{w+\top} \mathbf{C} \boldsymbol{\alpha}^{w+} = 1$. Hence, the w satisfies the two identifiability constraints.

Web Appendix E Optimization Algorithm

We summarize the algorithm as the following procedure:

1. **Outer Stage** (LAML): Estimate $\boldsymbol{\lambda}$ and $\boldsymbol{\theta}$ by maximizing $\mathcal{L}_{\text{LA}}^*(\boldsymbol{\lambda}, \boldsymbol{\theta})$ using BFGS.
At each iteration of BFGS:
 - (a) **Inner Stage** (Profile Likelihood): Estimate ϕ^w , α^f and β by the profile likelihood approach, where ϕ^w is estimated by maximizing $\mathbf{Q}(\phi^w; \boldsymbol{\lambda}, \boldsymbol{\theta})$ using Newton's method; at each iteration:
 - i. Estimate α^f and β by maximizing $\mathcal{L}(\phi^w, \alpha^f, \beta; \boldsymbol{\lambda}, \boldsymbol{\theta})$ using Newton's method.

The details are presented in the following Algorithms 2, 3 and 4. The algorithms are implemented using `cpp` code available at the R package file <https://github.com/tianyi-pan/aceDLNM/blob/main/src/aceDLNM.cpp>.

Algorithm 2 Outer Stage: Optimization for $\log \boldsymbol{\lambda}$ and $\log \boldsymbol{\theta}$

- 1: **while** not converged **do**
 - 2: Find $\hat{\phi}^w$, $\hat{\alpha}^f$ and $\hat{\beta}$ by Inner Stage optimization (Algorithm 3) with input $\boldsymbol{\lambda}$ and $\boldsymbol{\theta}$.
 - 3: Update $\log \boldsymbol{\lambda}$ and $\log \boldsymbol{\theta}$ by BFGS algorithm, where $\mathcal{L}_{\text{LA}}^*(\boldsymbol{\lambda}, \boldsymbol{\theta})$ and its gradient are evaluated as described in Web Appendix F.3.
 - 4: **end while**
 - 5: **return** $\hat{\boldsymbol{\lambda}}$, $\hat{\boldsymbol{\theta}}$, $\hat{\phi}^w$, $\hat{\alpha}^f$ and $\hat{\beta}$
-

Algorithm 3 Inner Stage: Optimization for ϕ^w

Require: λ and θ

```
1: while not converged do
2:   Find  $\hat{\alpha}^f$  and  $\hat{\beta}$  by Algorithm 4 with input  $\phi^w$ ,  $\lambda$  and  $\theta$ .
3:   Evaluate Hessian  $\nabla_{\phi^w}^2 \mathbf{Q}$  and gradient  $\nabla_{\phi^w} \mathbf{Q}$  (Web Appendix F.2).
4:   Check the convergence:  $\|\nabla_{\phi^w} \mathbf{Q}\|_2 \approx 0$ .
5:   Find the Newton step  $\Delta^{\phi^w}$  (Algorithm 5).
6:   while  $\mathbf{Q}(\phi^w) > \mathbf{Q}(\phi^w + \Delta^{\phi^w})$  do
7:     Step-halving:  $\Delta^{\phi^w} \leftarrow \Delta^{\phi^w}/2$ .
8:   end while
9:   Calculate  $\alpha^w$  according to  $\phi^w + \Delta^{\phi^w}$  and compute  $E(t) = \alpha^w \mathbf{D}(t)$ ,  $t = 1, 2, \dots, N$ .
10:  if the range of  $E(t)$  covers few (e.g.  $\leq 3$ ) knots of the B-spline for  $f$  then
11:    Step-halving:  $\Delta^{\phi^w} \leftarrow \Delta^{\phi^w}/2$ .
12:    Go back to step 9.
13:  end if
14:  Update:  $\phi^w \leftarrow \phi^w + \Delta^{\phi^w}$ .
15: end while
16: return  $\hat{\phi}^w$ ,  $\hat{\alpha}^f$  and  $\hat{\beta}$ 
```

Algorithm 4 Inner Stage: Optimization for α^f and β

Require: ϕ^w , λ and θ

```
1: while not converged do
2:   Evaluate Hessian  $\nabla_{\alpha^f, \beta}^2 \mathcal{L}$  and gradient  $\nabla_{\alpha^f, \beta} \mathcal{L}$  (Web Appendix F.1).
3:   Check the convergence:  $\|\nabla_{\alpha^f, \beta} \mathcal{L}\|_2 \approx 0$ .
4:   Find the Newton step  $\Delta^{\alpha^f, \beta}$  (Algorithm 5).
5:   while  $\mathcal{L}([\alpha^f, \beta]) > \mathcal{L}([\alpha^f, \beta] + \Delta^{\alpha^f, \beta})$  do
6:     Step-halving:  $\Delta^{\alpha^f, \beta} \leftarrow \Delta^{\alpha^f, \beta}/2$ .
7:   end while
8:   Update:  $[\alpha^f, \beta] \leftarrow [\alpha^f, \beta] + \Delta^{\alpha^f, \beta}$ .
9: end while
10: return  $\hat{\alpha}^f$  and  $\hat{\beta}$ 
```

We highlight the following step-having steps: (a) The step-havings in step 7, Algorithm 3 and step 6, Algorithm 4 are to ensure objective functions increase after Newton update. (b) The convergence of inner optimization is highly related to the current values of ϕ^w . If the range of $E(t)$ induced by the current ϕ^w contains only few knots of B-spline for f , there is not enough variation for f , and hence the convergence of inner optimization is difficult. Therefore, we propose to check the range of $E(t)$, and halve the Newton step until the range contains enough knots, e.g. 4 knots, in step 11, Algorithm 3.

The choice of starting values influences the speed and convergence of optimization algorithms. In Newton's method in the inner stage, we choose the results from the previous iteration as the starting values. In the outer stage, there is no standard guidance for the choice of starting values for BFGS. We recommend fitting a GAM (with the 0-day lagged exposure, for example) and using the fitted values as the starting values for parameters

excluding $\log \lambda^w$. The starting value for $\log \lambda^w$ is chosen as a moderate number arbitrarily. In our proposed R package `aceDLNM`, we fit the GAM using the modern big additive model framework (Wood et al., 2017) provided by `mgcv::bam`, and the starting value for $\log \lambda^w$ is fixed as 6 by default. We also provide an option for users to choose starting values based on prior knowledge.

Web Appendix E.1 Newton Step

Suppose the Hessian and gradient are \mathbf{H} and ∇ . The Newton step is obtained by $\mathbf{H}^{-1}\Delta$. To maintain Newton Step in an ascent direction and an appropriate length, \mathbf{H} should be positive definite. Let $\mathbf{H} = \mathbf{V}\mathbf{\Lambda}\mathbf{V}^\top$ by eigen-decomposition. \mathbf{H} is not positive definite numerically, if some $\mathbf{\Lambda}_{ii}$ are close to or smaller than zero.

To address the issue of \mathbf{H} , we adopt the following procedure. First, we check the minimum eigenvalue of \mathbf{H} using the Lanczos algorithm (Demmel, 1997). If the minimum eigenvalue is positive and not close to zero, we solve $\mathbf{H}^{-1}\nabla$ through Cholesky decomposition, otherwise, we find a Newton step by Algorithm 5. The Algorithm 5 based on the eigen-decomposition of \mathbf{H} follows the new Q-Newton’s method (Truong et al., 2023). The checking for the minimum eigenvalue is to avoid the eigen-decomposition — which is more expensive than Cholesky — in some iterations.

Algorithm 5 Find Newton Step Δ

Require: Hessian \mathbf{H} and gradient ∇ with dimension k .

- 1: Define \mathcal{I} as a $k \times k$ diagonal matrix, with diagonal element $\mathcal{I}_{i,i}$.
 - 2: Decompose $\mathbf{H} = \mathbf{V}\mathbf{\Lambda}\mathbf{V}^\top$ by eigen-decomposition, with eigenvalues $\lambda_1, \dots, \lambda_k$.
 - 3: **if** $\prod_{i=1}^k \lambda_i \approx 0$ **then**
 - 4: **for** $i = 1, \dots, k$ **do**
 - 5: Update $\lambda_i \leftarrow \lambda_i + \|\nabla\|_2$.
 - 6: **end for**
 - 7: **end if**
 - 8: **for** $i = 1, \dots, k$ **do**
 - 9: $\mathcal{I}_{i,i} = 1/|\lambda_i|$.
 - 10: **end for**
 - 11: **return** Newton step $\Delta = \mathbf{V}\mathcal{I}\mathbf{V}^\top\nabla$.
-

Web Appendix F Derivative Computation

The first- and second-order derivatives of \mathcal{L} are discussed in Web Appendix F.1. In Web Appendix F.2, we introduce the details of the first- and second-order derivatives computation of profile log-likelihood \mathbf{Q} . The first-order derivative of log-LAML $\mathcal{L}_{\text{LA}}^*$ w.r.t $\log \boldsymbol{\lambda}$ and $\log \boldsymbol{\theta}$ are described in Web Appendix F.3.

In this paper, we focus on the ACE-DLNM with a negative binomial distribution motivated by the Health Canada data. This framework applies generally to more general types of data, by taking the corresponding pdf/pmf in Web Appendix F.1.1 and the others hold the same.

All the derivatives are computed using `cpp` code available at the R package file <https://github.com/tianyi-pan/aceDLNM/blob/main/src/aceDLNM.cpp>.

Web Appendix F.1 Derivative of \mathcal{L}

We highlight the following terms in the calculation of the gradient and Hessian of \mathcal{L} : the probability mass function of the negative binomial distribution, the mean model, and the Jacobian matrix. The remaining parts of the derivatives are straightforward.

Web Appendix F.1.1 Probability mass function

The pmf of the negative binomial distribution is

$$f(x|\mu, \theta) = \exp \left\{ x \log \left(\frac{\mu}{\theta + \mu} \right) + \theta \log \left(\frac{\theta}{\theta + \mu} \right) + \log \left(\frac{\Gamma(x + \theta)}{\Gamma(\theta)x!} \right) \right\},$$

where $\Gamma(\cdot)$ is the gamma function.

Taking derivative of $\log f(x|\mu, \theta)$ w.r.t μ and θ leads to

$$\begin{aligned} \frac{\partial}{\partial \mu} \log f(x|\mu, \theta) &= \frac{x}{\mu} - \frac{\theta + x}{\theta + \mu}, \\ \frac{\partial}{\partial \theta} \log f(x|\mu, \theta) &= \log \left(\frac{\theta}{\theta + \mu} \right) + \frac{\mu - x}{\theta + \mu} + \psi(\theta + x) - \psi(\theta), \\ \frac{\partial}{\partial \log \theta} \log f(x|\mu, \theta) &= \theta \frac{\partial}{\partial \theta} \log f(x|\mu, \theta), \end{aligned}$$

where $\psi(s) = d \log \Gamma(s) / ds$.

The 2nd-order derivatives are given by

$$\begin{aligned} \frac{\partial^2}{\partial \mu^2} \log f(x|\mu, \theta) &= -\frac{x}{\mu^2} + \frac{\theta + x}{(\theta + \mu)^2}, \\ \frac{\partial^2}{\partial \theta^2} \log f(x|\mu, \theta) &= \frac{1}{\theta} - \frac{1}{\theta + \mu} - \frac{\mu - x}{(\theta + \mu)^2} + \psi'(\theta + x) - \psi'(\theta), \\ \frac{\partial^2}{\partial \log \theta^2} \log f(x|\mu, \theta) &= \theta^2 \frac{\partial^2}{\partial \theta^2} \log f(x|\mu, \theta) + \theta \frac{\partial}{\partial \theta} \log f(x|\mu, \theta), \\ \frac{\partial^2}{\partial \theta \partial \mu} \log f(x|\mu, \theta) &= \frac{x - \mu}{(\theta + \mu)^2}, \\ \frac{\partial^2}{\partial \log \theta \partial \mu} \log f(x|\mu, \theta) &= \theta \frac{\partial^2}{\partial \theta \partial \mu} \log f(x|\mu, \theta), \end{aligned}$$

where $\psi'(x + \theta) = d\psi(x)/dx$. However, $\Gamma(s)$, $\psi(x)$ and $\psi'(x + \theta)$ are intractable analytically. We adopt the Lanczos approximation (Lanczos, 1964) for the gamma function $\Gamma(s)$. The derivative of $\Gamma(s)$ is approximated by the Algorithm AS103 in Bernardo et al. (1976). Both algorithms are differentiable using `autodiff`, which is required for the derivative calculation of $\mathcal{L}_{\text{LA}}^*$ (Web Appendix F.3).

Web Appendix F.1.2 Mean model

By the model specification, we have

$$\log \mu_t = f \{ \boldsymbol{\alpha}^{w\top} \mathbf{D}(t) \} = \sum_q b_q^f(\boldsymbol{\alpha}^{w\top} \mathbf{D}(t)) \alpha_q^f.$$

Then, we have the 1st-order derivatives

$$\begin{aligned} \frac{\partial \log \mu_t}{\partial \boldsymbol{\alpha}^w} &= \mathbf{D}(t) \sum_q b_q'^f(\boldsymbol{\alpha}^{w\top} \mathbf{D}(t)) \alpha_q^f, \\ \frac{\partial \log \mu_t}{\partial \boldsymbol{\alpha}^f} &= \{ b_q^f(\boldsymbol{\alpha}^{w\top} \mathbf{D}(t)) \}_q, \end{aligned}$$

and the 2nd-order derivatives

$$\begin{aligned} \frac{\partial^2 \log \mu_t}{\partial \boldsymbol{\alpha}^{w2}} &= \mathbf{D}(t) \mathbf{D}(t)^\top \sum_q b_q''^f(\boldsymbol{\alpha}^{w\top} \mathbf{D}(t)) \alpha_q^f, \\ \frac{\partial^2 \log \mu_t}{\partial \boldsymbol{\alpha}^{f2}} &= 0, \\ \frac{\partial^2 \log \mu_t}{\partial \boldsymbol{\alpha}^f \partial \boldsymbol{\alpha}^w} &= \left\{ b_q'^f(\boldsymbol{\alpha}^{w\top} \mathbf{D}(t)) \right\}_j \mathbf{D}(t)^\top. \end{aligned}$$

The derivatives of μ are given by

$$\begin{aligned} \frac{\partial \mu_t}{\partial \boldsymbol{\alpha}^w} &= \mu_t \frac{\partial \log \mu_t}{\partial \boldsymbol{\alpha}^w}, \\ \frac{\partial \mu_t}{\partial \boldsymbol{\alpha}^f} &= \mu_t \frac{\partial \log \mu_t}{\partial \boldsymbol{\alpha}^f}, \\ \frac{\partial^2 \mu_t}{\partial \boldsymbol{\alpha}^{w2}} &= \mu_t \left(\frac{\partial \log \mu_t}{\partial \boldsymbol{\alpha}^w} \right)^2 + \mu_t \frac{\partial^2 \log \mu_t}{\partial \boldsymbol{\alpha}^{w2}}, \\ \frac{\partial^2 \mu_t}{\partial \boldsymbol{\alpha}^{f2}} &= \mu_t \left(\frac{\partial \log \mu_t}{\partial \boldsymbol{\alpha}^f} \right)^2 + \mu_t \frac{\partial^2 \log \mu_t}{\partial \boldsymbol{\alpha}^{f2}}, \\ \frac{\partial^2 \mu_t}{\partial \boldsymbol{\alpha}^w \partial \boldsymbol{\alpha}^f} &= \mu_t \frac{\partial \log \mu_t}{\partial \boldsymbol{\alpha}^w} \frac{\partial \log \mu_t}{\partial \boldsymbol{\alpha}^f} + \mu_t \frac{\partial^2 \log \mu_t}{\partial \boldsymbol{\alpha}^w \partial \boldsymbol{\alpha}^f}. \end{aligned}$$

The s -order derivative of the B-spline function $b_{l,p}(x)$ is given by Equation S.4; see more details in Wood (2017a).

Web Appendix F.1.3 Reparameterization

We make inferences for the unconstrained parameter $\boldsymbol{\phi}^w$. Define $\boldsymbol{\phi}^{wL} = [1, \boldsymbol{\phi}^w]^\top$. The Jacobian is given by

$$\frac{\partial \boldsymbol{\alpha}^w}{\partial \boldsymbol{\phi}^{wL}} = \left(\boldsymbol{\phi}^{wL\top} \mathbf{C} \boldsymbol{\phi}^{wL} \right)^{-\frac{1}{2}} \mathbf{I} - \boldsymbol{\phi}^{wL} \boldsymbol{\phi}^{wL\top} \mathbf{C} \left(\boldsymbol{\phi}^{wL\top} \mathbf{C} \boldsymbol{\phi}^{wL} \right)^{-\frac{3}{2}},$$

Then, we obtain $\partial \boldsymbol{\alpha}^w / \partial \boldsymbol{\phi}^w$ by removing the first column of $\partial \boldsymbol{\alpha}^w / \partial \boldsymbol{\phi}^{wL}$.

Web Appendix F.2 Derivative of Q

Web Appendix F.2.1 First-Order Derivative of Q

The profile log-likelihood $\mathbf{Q}(\phi^w; \lambda, \theta)$ is related to the estimates from the inner optimization, which are implicit functions of ϕ^w . We obtain the derivatives by implicit differentiation. The first-order derivative is given by

$$\begin{aligned} \frac{\partial \mathbf{Q}(\phi^w; \lambda, \theta)}{\partial \phi^w} &= \frac{\partial \mathcal{L}(\phi^w, \alpha^f, \beta; \lambda, \theta)}{\partial \phi^w} \Big|_{\alpha^f = \hat{\alpha}^f(\phi^w), \beta = \hat{\beta}(\phi^w)} \\ &\quad + \frac{\partial [\hat{\alpha}^f(\phi^w), \hat{\beta}(\phi^w)]}{\partial \phi^w} \frac{\partial \mathcal{L}(\phi^w, \hat{\alpha}^f(\phi^w), \hat{\beta}(\phi^w); \lambda, \theta)}{\partial [\alpha^f, \beta]^\top}. \end{aligned}$$

By definition, we have $\partial \mathcal{L}(\phi^w, \hat{\alpha}^f(\phi^w), \hat{\beta}(\phi^w); \lambda, \theta) / \partial [\alpha^f, \beta]^\top = 0$. Therefore, we have

$$\frac{\partial \mathbf{Q}(\phi^w; \lambda, \theta)}{\partial \phi^w} = \frac{\partial \mathcal{L}(\phi^w, \alpha^f, \beta; \lambda, \theta)}{\partial \phi^w} \Big|_{\alpha^f = \hat{\alpha}^f(\phi^w), \beta = \hat{\beta}(\phi^w)},$$

which is a part of the first-order derivative of \mathcal{L} .

Web Appendix F.2.2 Second-Order Derivative of Q

We define $\mathbf{H}^{\eta, w}$ as

$$\mathbf{H}^{\eta, w} = \frac{\partial^2 \mathcal{L}(\phi^w, \alpha^f, \beta; \lambda, \theta)}{\partial [\alpha^f, \beta] \partial \phi^w} \Big|_{\alpha^f = \hat{\alpha}^f(\phi^w), \beta = \hat{\beta}(\phi^w)}.$$

Then, the second-order derivative can be written as

$$\begin{aligned} \frac{\partial^2 \mathbf{Q}(\phi^w; \lambda, \theta)}{\partial \phi^{w2}} &= \frac{\partial^2 \mathcal{L}(\phi^w, \alpha^f, \beta; \lambda, \theta)}{\partial \phi^{w2}} \Big|_{\alpha^f = \hat{\alpha}^f(\phi^w), \beta = \hat{\beta}(\phi^w)} \\ &\quad + \frac{\partial [\hat{\alpha}^f(\phi^w), \hat{\beta}(\phi^w)]}{\partial \phi^w} \mathbf{H}^{\eta, w}. \end{aligned}$$

The derivative $\partial [\hat{\alpha}^f(\phi^w), \hat{\beta}(\phi^w)] / \partial \phi^w$ is obtained through the implicit differentiation. Given that $\partial \mathcal{L}(\phi^w, \hat{\alpha}^f(\phi^w), \hat{\beta}(\phi^w); \lambda, \theta) / \partial [\alpha^f, \beta] = 0$, taking derivative with respect to ϕ^w on both sides leads to

$$\frac{\partial^2 \mathcal{L}(\phi^w, \hat{\alpha}^f(\phi^w), \hat{\beta}(\phi^w); \lambda, \theta)}{\partial [\alpha^f, \beta]^2} \frac{\partial [\hat{\alpha}^f(\phi^w), \hat{\beta}(\phi^w)]}{\partial \phi^w} = -\mathbf{H}^{\eta, w}.$$

Solving this equation gives $\partial [\hat{\alpha}^f(\phi^w), \hat{\beta}(\phi^w)] / \partial \phi^w$.

Web Appendix F.3 Derivative of $\mathcal{L}_{\text{LA}}^*$

In the outer stage, we use the BFGS algorithm to maximize $\mathcal{L}_{\text{LA}}^*$ for $\log \boldsymbol{\lambda}$ and $\log \boldsymbol{\theta}$. In this Newton-type algorithm, the gradient is required.

Recall that the log-LAML is

$$\begin{aligned} \mathcal{L}_{\text{LA}}^*(\boldsymbol{\lambda}, \boldsymbol{\theta}) = & \mathcal{L}(\hat{\mathbf{u}}(\boldsymbol{\lambda}, \boldsymbol{\theta}); \boldsymbol{\lambda}, \boldsymbol{\theta}) - \frac{1}{2} \log \{\det \boldsymbol{\mathcal{H}}(\hat{\mathbf{u}}(\boldsymbol{\lambda}, \boldsymbol{\theta}); \boldsymbol{\lambda}, \boldsymbol{\theta})\} + \frac{M}{2} \log(2\pi) \\ & + \frac{1}{2} \log |\boldsymbol{\lambda}^w \mathbf{S}^w|_+ + \frac{1}{2} \log |\boldsymbol{\lambda}^f \mathbf{S}^f|_+ + \frac{1}{2} \sum_{j=1}^p \log |\lambda_j^h \mathbf{S}_j^h|_+. \end{aligned}$$

We will describe the first-order derivatives of $\mathcal{L}(\hat{\mathbf{u}}(\boldsymbol{\lambda}, \boldsymbol{\theta}); \boldsymbol{\lambda}, \boldsymbol{\theta})$. The other derivatives are discussed in Section 3.2.3.

The first-order derivative of $\mathcal{L}(\hat{\mathbf{u}}(\boldsymbol{\lambda}, \boldsymbol{\theta}); \boldsymbol{\lambda}, \boldsymbol{\theta})$ is given by

$$\frac{\partial \mathcal{L}(\hat{\mathbf{u}}(\boldsymbol{\lambda}, \boldsymbol{\theta}); \boldsymbol{\lambda}, \boldsymbol{\theta})}{\partial [\log \boldsymbol{\lambda}, \log \boldsymbol{\theta}]} = \frac{\partial \mathcal{L}(\mathbf{u}, \boldsymbol{\lambda}, \boldsymbol{\theta})}{\partial [\log \boldsymbol{\lambda}, \log \boldsymbol{\theta}]} \Big|_{\mathbf{u}=\hat{\mathbf{u}}(\boldsymbol{\lambda}, \boldsymbol{\theta})} + \frac{\partial \hat{\mathbf{u}}(\boldsymbol{\lambda}, \boldsymbol{\theta})}{\partial [\log \boldsymbol{\lambda}, \log \boldsymbol{\theta}]} \left[\frac{\partial \mathcal{L}(\mathbf{u}, \boldsymbol{\lambda}, \boldsymbol{\theta})}{\partial \mathbf{u}} \Big|_{\mathbf{u}=\hat{\mathbf{u}}(\boldsymbol{\lambda}, \boldsymbol{\theta})} \right].$$

The derivatives of \mathcal{L} are described in Web Appendix F.1. We address the unsolved part, the derivative of $\hat{\mathbf{u}}(\boldsymbol{\lambda}, \boldsymbol{\theta})$, using the implicit differentiation.

The estimator $\hat{\boldsymbol{\phi}}^w(\boldsymbol{\lambda}, \boldsymbol{\theta})$ is obtained from maximizing the profile likelihood $\mathbf{Q}(\boldsymbol{\phi}^w; \boldsymbol{\lambda}, \boldsymbol{\theta})$. Therefore, we have, $\partial \mathbf{Q}(\hat{\boldsymbol{\phi}}^w; \boldsymbol{\lambda}, \boldsymbol{\theta}) / \partial \boldsymbol{\phi}^w = 0$. The derivative can be written as

$$\begin{aligned} 0 = \frac{\partial \mathbf{Q}(\hat{\boldsymbol{\phi}}^w; \boldsymbol{\lambda}, \boldsymbol{\theta})}{\partial \boldsymbol{\phi}^w} = & \frac{\partial \mathcal{L}(\boldsymbol{\phi}^w, \boldsymbol{\alpha}^f, \boldsymbol{\beta}; \boldsymbol{\lambda}, \boldsymbol{\theta})}{\partial \boldsymbol{\phi}^w} \Big|_{\boldsymbol{\phi}^w=\hat{\boldsymbol{\phi}}^w(\boldsymbol{\lambda}, \boldsymbol{\theta}), \boldsymbol{\alpha}^f=\hat{\boldsymbol{\alpha}}^f(\boldsymbol{\phi}^w), \boldsymbol{\beta}=\hat{\boldsymbol{\beta}}(\boldsymbol{\phi}^w)} \\ & + \frac{\partial \mathcal{L}(\boldsymbol{\phi}^w, \hat{\boldsymbol{\alpha}}^f(\boldsymbol{\phi}^w), \hat{\boldsymbol{\beta}}(\boldsymbol{\phi}^w); \boldsymbol{\lambda}, \boldsymbol{\theta})}{\partial [\boldsymbol{\alpha}^f, \boldsymbol{\beta}]} \frac{\partial [\hat{\boldsymbol{\alpha}}^f(\boldsymbol{\phi}^w), \hat{\boldsymbol{\beta}}(\boldsymbol{\phi}^w)]}{\partial \boldsymbol{\phi}^w}. \end{aligned}$$

Recall that $\hat{\mathbf{u}}(\boldsymbol{\lambda}, \boldsymbol{\theta}) = [\hat{\boldsymbol{\alpha}}(\boldsymbol{\lambda}, \boldsymbol{\theta}), \hat{\boldsymbol{\beta}}(\boldsymbol{\lambda}, \boldsymbol{\theta}), \hat{\boldsymbol{\phi}}^w(\boldsymbol{\lambda}, \boldsymbol{\theta})]^\top$. The estimates $\hat{\boldsymbol{\alpha}}^f, \hat{\boldsymbol{\beta}}$ are obtained from maximizing \mathcal{L} , and therefore,

$$\frac{\partial \mathcal{L}(\boldsymbol{\phi}^w, \hat{\boldsymbol{\alpha}}^f(\boldsymbol{\phi}^w), \hat{\boldsymbol{\beta}}(\boldsymbol{\phi}^w); \boldsymbol{\lambda}, \boldsymbol{\theta})}{\partial [\boldsymbol{\alpha}^f, \boldsymbol{\beta}]} = 0. \quad (\text{S.12})$$

Hence, we have

$$\frac{\partial \mathcal{L}(\boldsymbol{\phi}^w, \boldsymbol{\alpha}^f, \boldsymbol{\beta}; \boldsymbol{\lambda}, \boldsymbol{\theta})}{\partial \boldsymbol{\phi}^w} \Big|_{\boldsymbol{\phi}^w=\hat{\boldsymbol{\phi}}^w(\boldsymbol{\lambda}, \boldsymbol{\theta}), \boldsymbol{\alpha}^f=\hat{\boldsymbol{\alpha}}^f(\boldsymbol{\phi}^w), \boldsymbol{\beta}=\hat{\boldsymbol{\beta}}(\boldsymbol{\phi}^w)} = 0. \quad (\text{S.13})$$

Combining the Equations S.12 and S.13 yields

$$\frac{\partial \mathcal{L}(\hat{\mathbf{u}}(\boldsymbol{\lambda}, \boldsymbol{\theta}), \boldsymbol{\lambda}, \boldsymbol{\theta})}{\partial \mathbf{u}} = 0.$$

Taking derivative with respect to $[\log \boldsymbol{\lambda}, \log \boldsymbol{\theta}]$ on both sides of the equation leads to

$$\frac{\partial^2 \mathcal{L}(\hat{\mathbf{u}}(\boldsymbol{\lambda}, \boldsymbol{\theta}), \boldsymbol{\lambda}, \boldsymbol{\theta})}{\partial \mathbf{u}^2} \frac{\partial \hat{\mathbf{u}}(\boldsymbol{\lambda}, \boldsymbol{\theta})}{\partial [\log \boldsymbol{\lambda}, \log \boldsymbol{\theta}]} = - \frac{\partial^2 \mathcal{L}(\mathbf{u}, \boldsymbol{\lambda}, \boldsymbol{\theta})}{\partial \mathbf{u} \partial [\log \boldsymbol{\lambda}, \log \boldsymbol{\theta}]} \Big|_{\mathbf{u}=\hat{\mathbf{u}}(\boldsymbol{\lambda}, \boldsymbol{\theta})}.$$

Solving this equation gives the derivative of $\hat{\mathbf{u}}(\boldsymbol{\lambda}, \boldsymbol{\theta})$.

Web Appendix G Delta Method

To quantify the uncertainty in maximum likelihood estimators with transformation, the delta method is a standard manner. The unconstrained parameters $\mathbf{u} = [\boldsymbol{\phi}^w, \boldsymbol{\alpha}^f, \boldsymbol{\beta}]^\top$ is estimated by maximizing (penalized) log-likelihood. We estimate the variance of $\widehat{\mathbf{u}}(\boldsymbol{\lambda}, \boldsymbol{\theta})$ by the inverse of the negative Hessian matrix, i.e. $\widehat{\text{Var}}(\widehat{\mathbf{u}}(\boldsymbol{\lambda}, \boldsymbol{\theta})) = [\boldsymbol{\mathcal{H}}(\widehat{\mathbf{u}}(\boldsymbol{\lambda}, \boldsymbol{\theta}))]^{-1}$. Then, the estimated variance of the constrained parameters, $[\boldsymbol{\alpha}^w, \boldsymbol{\alpha}^f, \boldsymbol{\beta}]^\top$, in the original parameter space is given by

$$\widehat{\text{Var}}([\boldsymbol{\alpha}^w, \boldsymbol{\alpha}^f, \boldsymbol{\beta}]^\top) = \mathbf{J}[\widehat{\mathbf{u}}(\boldsymbol{\lambda}, \boldsymbol{\theta})] [\boldsymbol{\mathcal{H}}(\widehat{\mathbf{u}}(\boldsymbol{\lambda}, \boldsymbol{\theta}))]^{-1} \mathbf{J}[\widehat{\mathbf{u}}(\boldsymbol{\lambda}, \boldsymbol{\theta})]^\top,$$

where $\mathbf{J}[\widehat{\mathbf{u}}(\boldsymbol{\lambda}, \boldsymbol{\theta})]$ is the Jacobian matrix of reparametrization from $[\boldsymbol{\phi}^w, \boldsymbol{\alpha}^f, \boldsymbol{\beta}]^\top$ to $[\boldsymbol{\alpha}^w, \boldsymbol{\alpha}^f, \boldsymbol{\beta}]^\top$ evaluated at $\widehat{\mathbf{u}}(\boldsymbol{\lambda}, \boldsymbol{\theta})$. The details of the Jacobian matrix can be found in Web Appendix F.1.3.

The approximated $(1 - \alpha)$ confidence intervals for i^{th} parameters are obtained as

$$[\widehat{\boldsymbol{\alpha}}^w, \widehat{\boldsymbol{\alpha}}^f, \widehat{\boldsymbol{\beta}}]_i^\top \pm z_{\alpha/2} \left\{ \mathbf{J}[\widehat{\mathbf{u}}(\boldsymbol{\lambda}, \boldsymbol{\theta})] [\boldsymbol{\mathcal{H}}(\widehat{\mathbf{u}}(\boldsymbol{\lambda}, \boldsymbol{\theta}))]^{-1} \mathbf{J}[\widehat{\mathbf{u}}(\boldsymbol{\lambda}, \boldsymbol{\theta})]^\top \right\}_{ii}^{1/2},$$

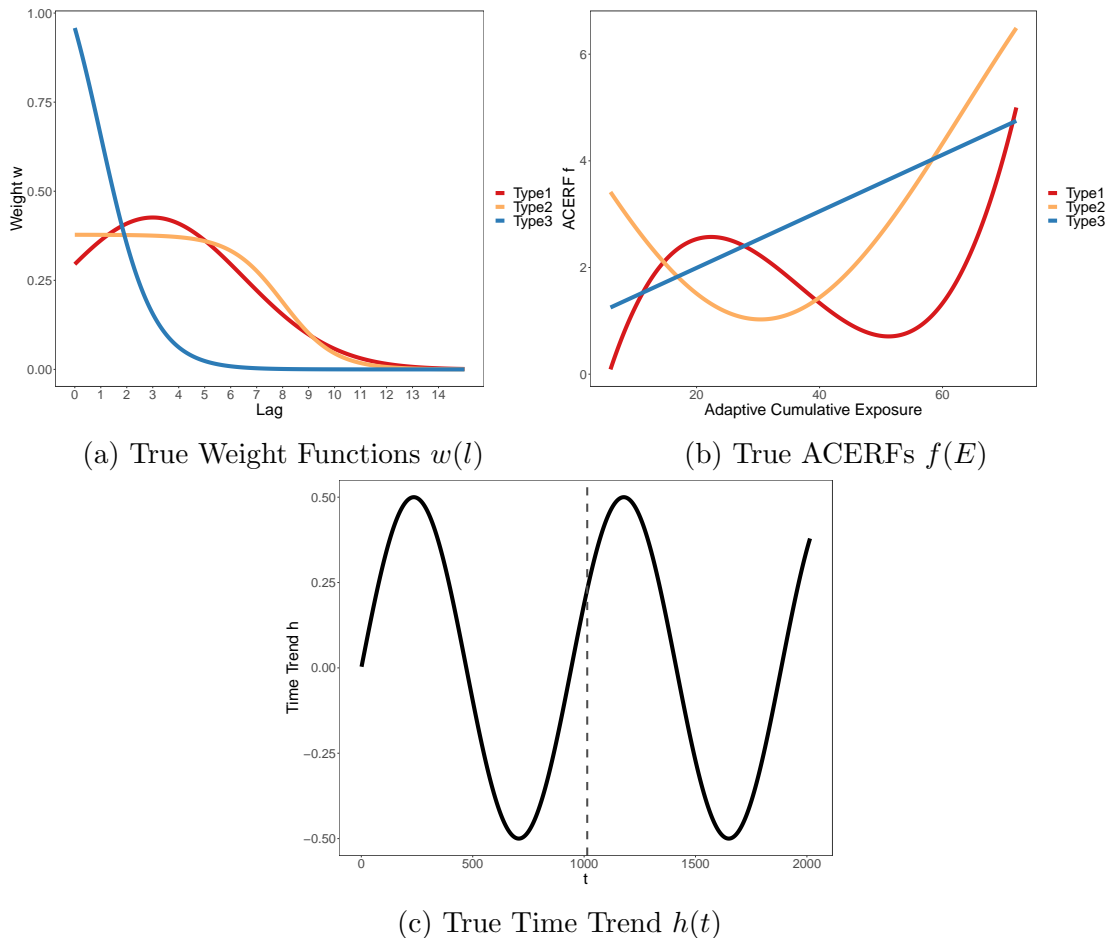
where $z_{1-\alpha/2}$ is the $1 - \alpha/2$ quantile of a standard normal distribution. We replace $\boldsymbol{\lambda}$ and $\boldsymbol{\theta}$ by their estimates, and their uncertainty is ignored as is typical in GAM contexts (Wood et al., 2016).

To our knowledge, there are no existing results that guarantee the performance of the delta method in finite samples. In Simulation A, we found that it yielded poor finite sample performance (see Web Table 5). Instead, we recommend the sampling method described in Section 3.4.

Web Appendix H Simulations

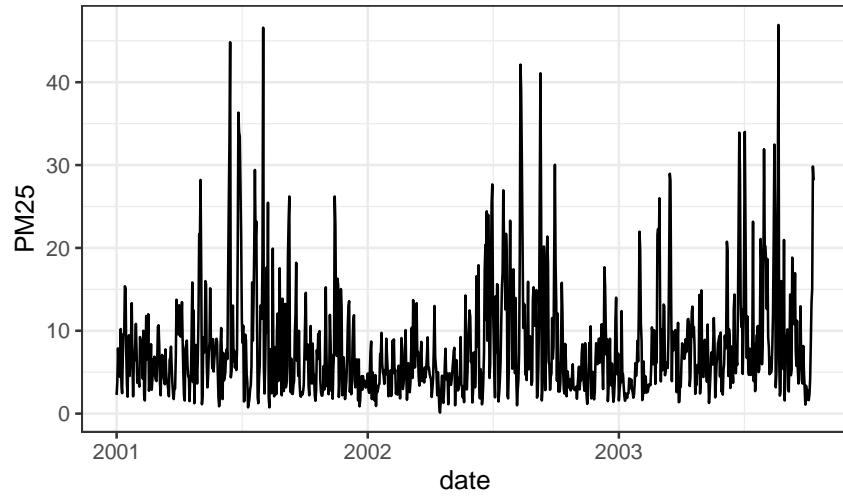
Web Appendix H.1 Data-Generation Details

The true functions for data generation are visualized in Web Figure 1.

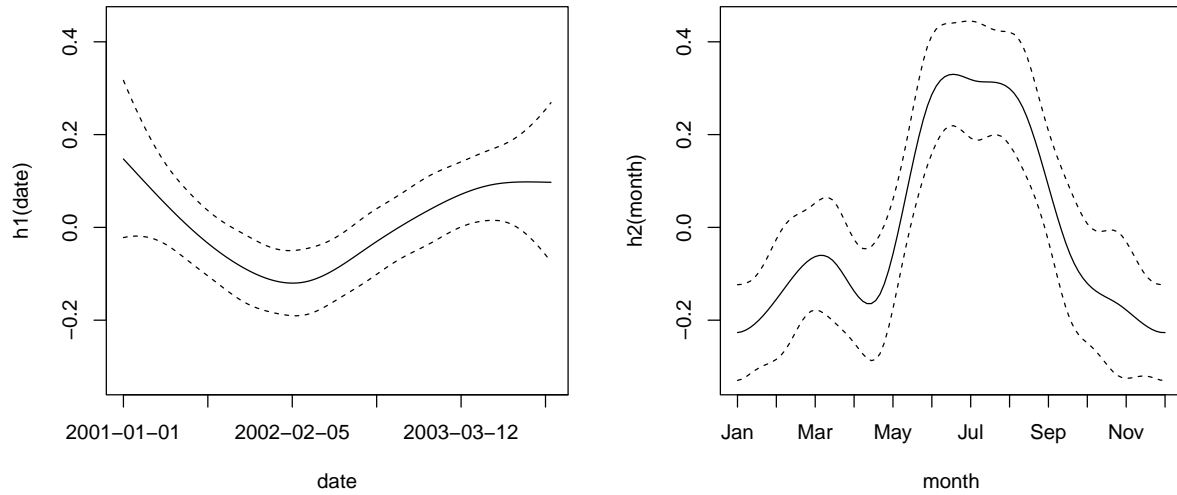


Web Figure 1. True functions in Simulation A, including (a) three types of w , (b) three types of f , and (c) h where the curve on the left of the dashed line is for the sample size of 1,000 and the full curve is for the sample size of 2,000.

We use the $\text{PM}_{2.5}$ concentrations to generate data in the simulation studies. In Web Figure 2a, we visualize the $\text{PM}_{2.5}$ concentrations from Jan. 1, 2001 to Oct. 11, 2003 (corresponding to a sample size of 1000). To illustrate seasonality in the $\text{PM}_{2.5}$ concentrations, we fit a generalized additive model, regressing the log-transformed $\text{PM}_{2.5}$ concentrations on a smooth function of date for the time trend and a cyclic smooth function of month for seasonality (the residual diagnostics show no evidence of a lack of model fit). We plot the estimated function in Web Figure 2b, and observe a seasonal pattern.



(a) Visualization of the $PM_{2.5}$ concentrations.

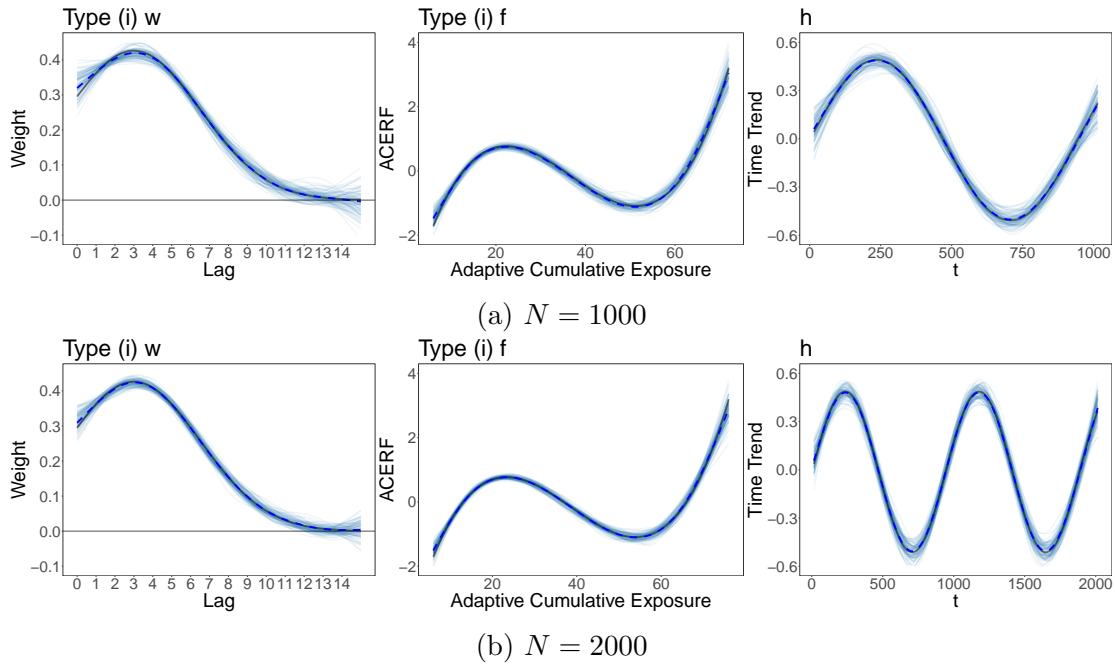


(b) Estimated time trend and seasonality in $PM_{2.5}$ concentrations.

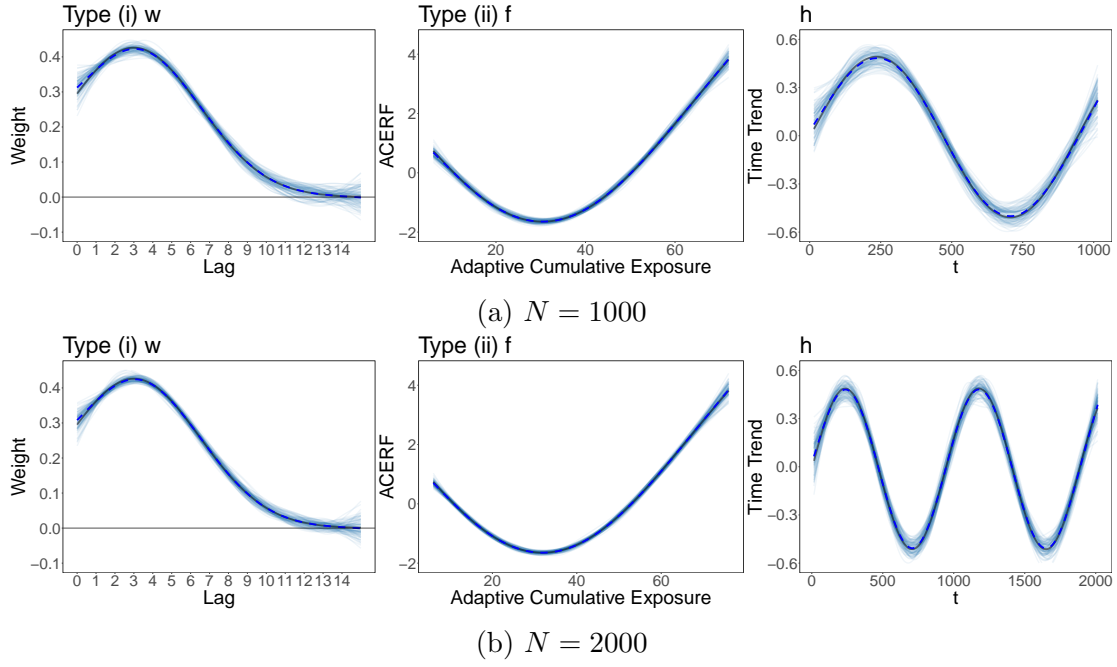
Web Figure 2. $PM_{2.5}$ concentrations in Waterloo from Jan. 1, 2001 to Oct. 11, 2003, corresponding to a sample size of 1000.

Web Appendix H.2 Additional Simulation Results

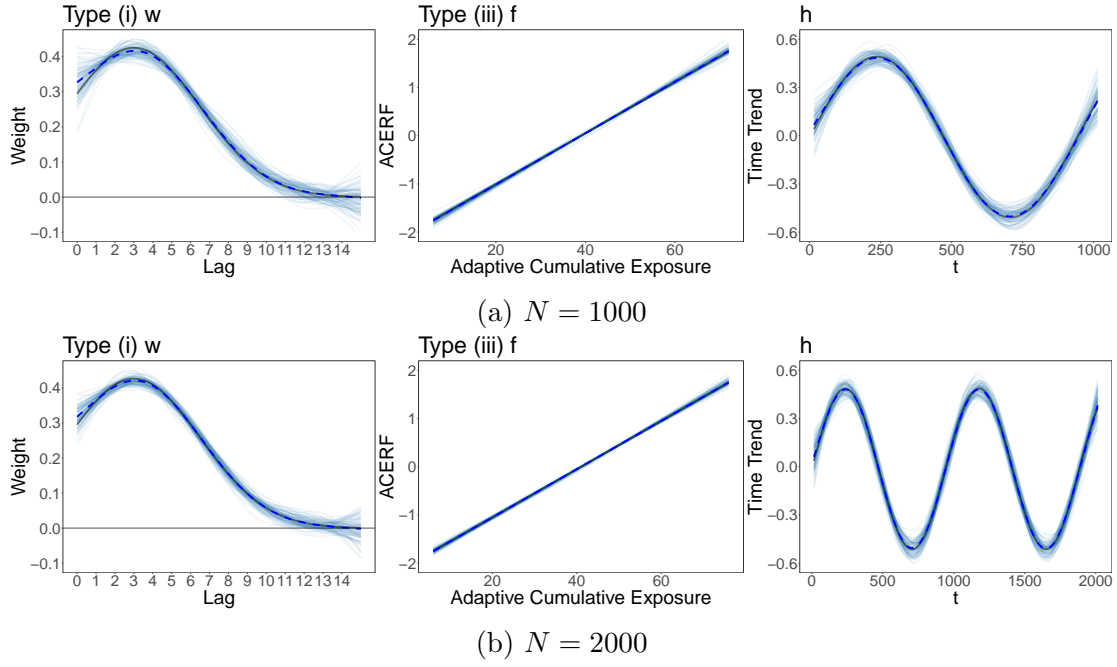
Web Appendix H.2.1 Visualization of Simulation A Results



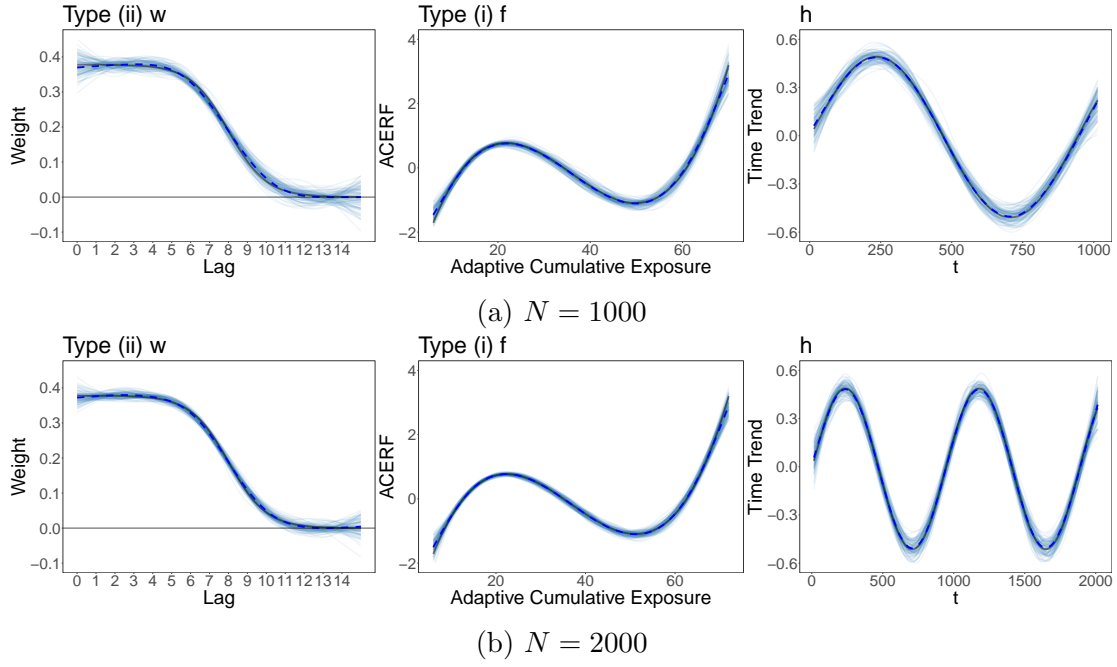
Web Figure 3. Visualization of Simulation A Results. The data are generated with type (i) weight function and type (i) ACERF. The sample sizes are 1,000 (a) and 2,000 (b). The estimates from the first 100 simulated data for the weight function $w(l)$ (first column), ACEFR $f(E)$ (second column) and the time trend $h(t)$ (third column) are labelled by blue curves. The dashed blue curves show the mean of the estimates over all of the 10,000 simulated datasets. The true functions are the solid black curves.



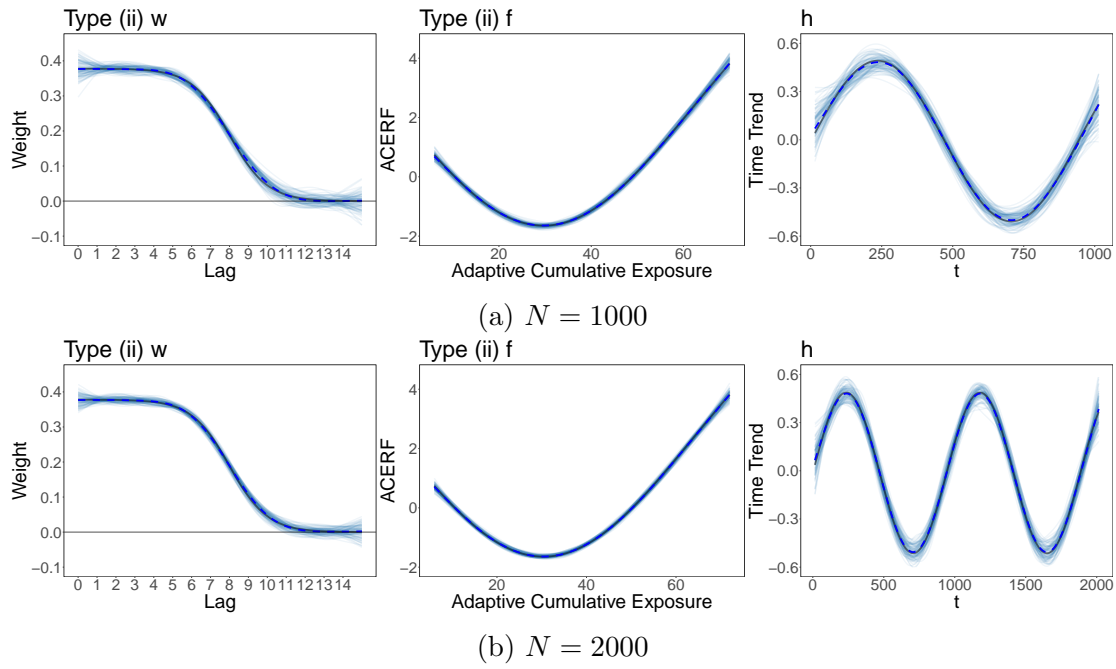
Web Figure 4. Visualization of Simulation A Results. The data are generated under type (i) weight function and type (ii) ACERF. The sample sizes are 1,000 (a) and 2,000 (b). The estimates from the first 100 simulated data for the weight function $w(l)$ (first column), ACEFR $f(E)$ (second column) and the time trend $h(t)$ (third column) are labelled by blue curves. The dashed blue curves show the mean of the estimates over all of the 10,000 simulated datasets. The true functions are the solid black curves.



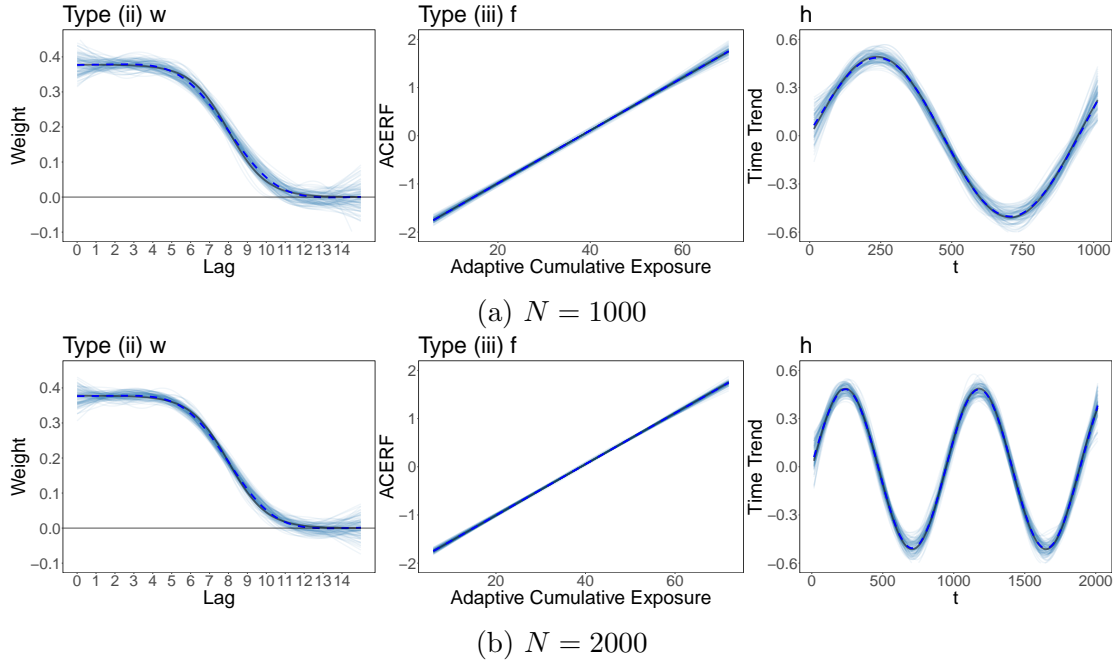
Web Figure 5. Visualization of Simulation A Results. The data are generated under type (i) weight function and type (iii) ACERF. The sample sizes are 1,000 (a) and 2,000 (b). The estimates from the first 100 simulated data for the weight function $w(l)$ (first column), ACEFR $f(E)$ (second column) and the time trend $h(t)$ (third column) are labelled by blue curves. The dashed blue curves show the mean of the estimates over all of the 10,000 simulated datasets. The true functions are the solid black curves.



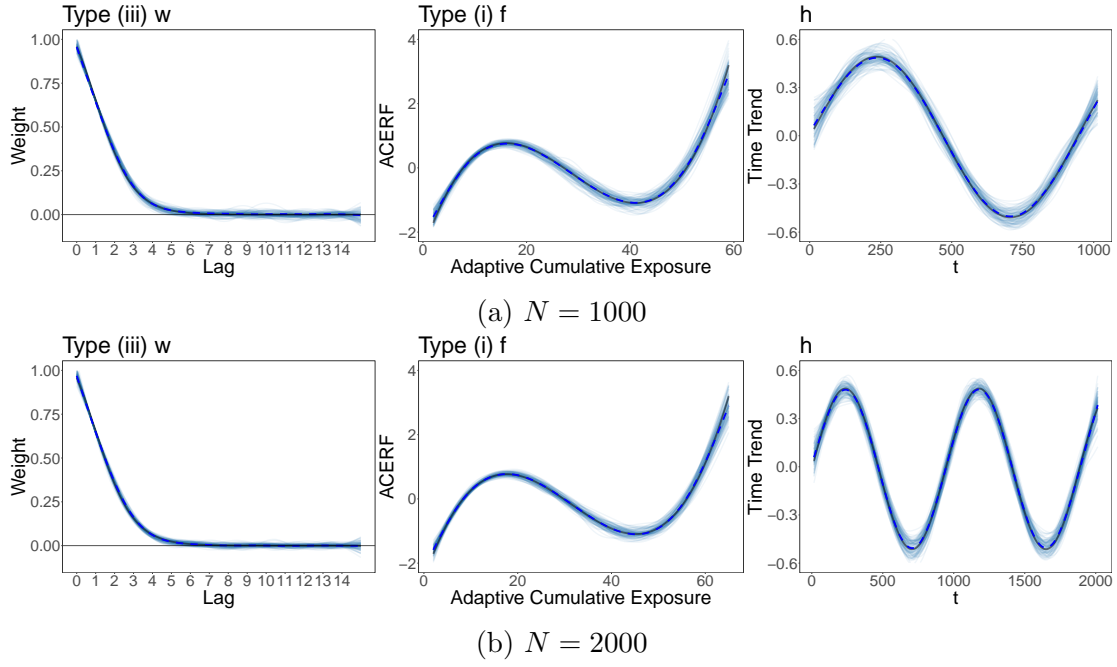
Web Figure 6. Visualization of Simulation A Results. The data are generated under type (ii) weight function and type (i) ACERF. The sample sizes are 1,000 (a) and 2,000 (b). The estimates from the first 100 simulated data for the weight function $w(l)$ (first column), ACEFR $f(E)$ (second column) and the time trend $h(t)$ (third column) are labelled by blue curves. The dashed blue curves show the mean of the estimates over all of the 10,000 simulated datasets. The true functions are the solid black curves.



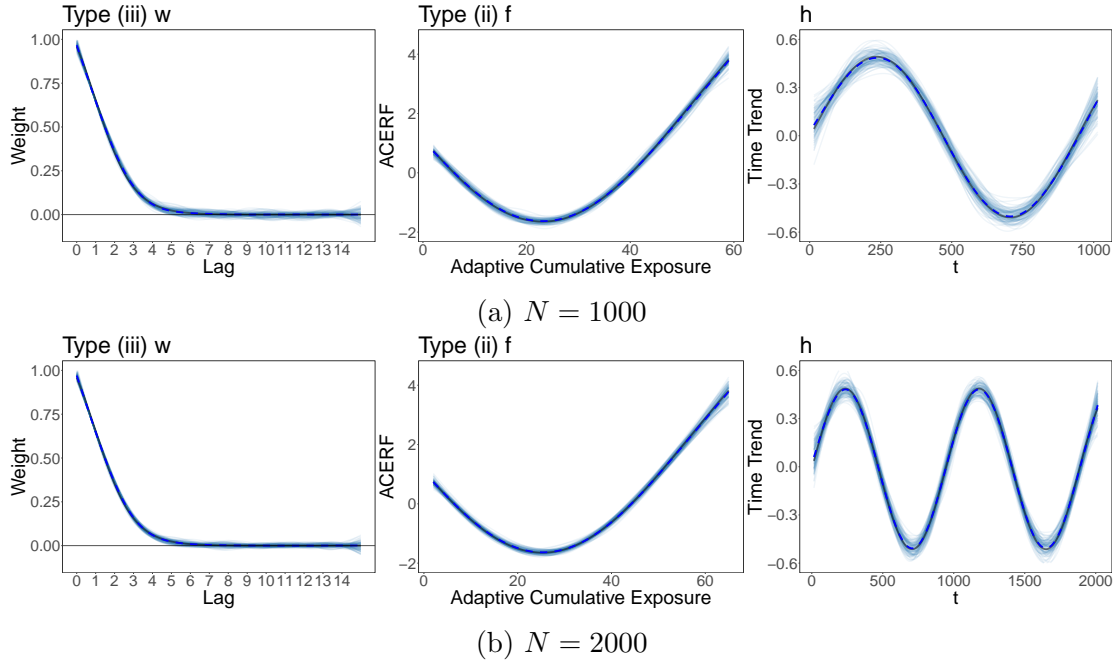
Web Figure 7. Visualization of Simulation A Results. The data are generated under type (ii) weight function and type (ii) ACERF. The sample sizes are 1,000 (a) and 2,000 (b). The estimates from the first 100 simulated data for the weight function $w(l)$ (first column), ACEFR $f(E)$ (second column) and the time trend $h(t)$ (third column) are labelled by blue curves. The dashed blue curves show the mean of the estimates over all of the 10,000 simulated datasets. The true functions are the solid black curves.



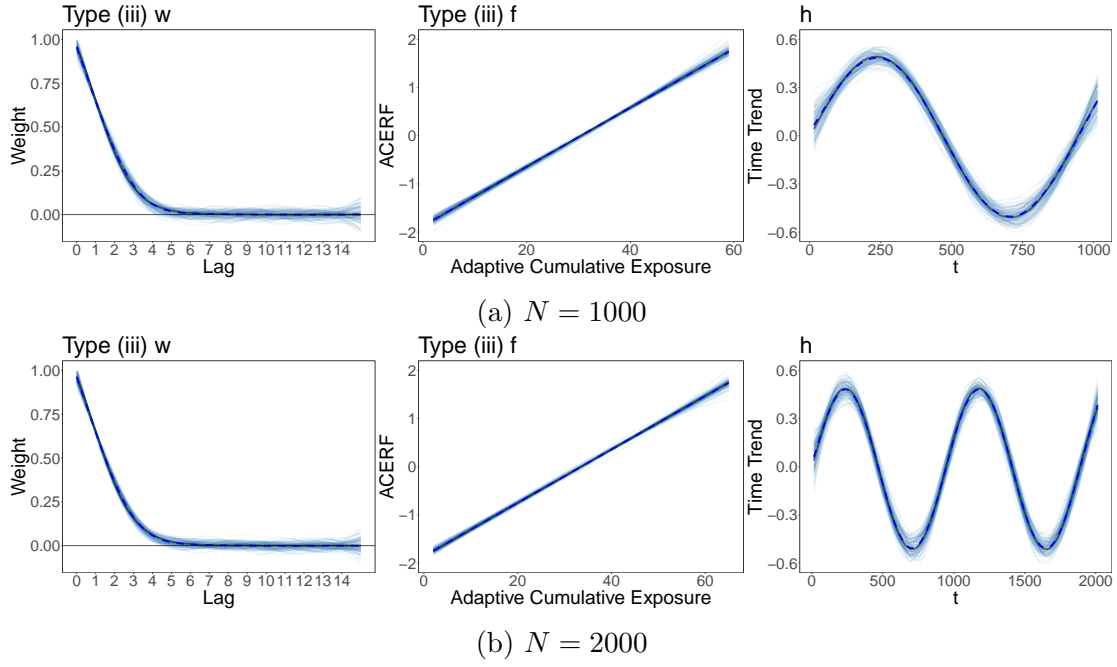
Web Figure 8. Visualization of Simulation A Results. The data are generated under type (ii) weight function and type (iii) ACERF. The sample sizes are 1,000 (a) and 2,000 (b). The estimates from the first 100 simulated data for the weight function $w(l)$ (first column), ACEFR $f(E)$ (second column) and the time trend $h(t)$ (third column) are labelled by blue curves. The dashed blue curves show the mean of the estimates over all of the 10,000 simulated datasets. The true functions are the solid black curves.



Web Figure 9. Visualization of Simulation A Results. The data are generated under type (iii) weight function and type (i) ACERF. The sample sizes are 1,000 (a) and 2,000 (b). The estimates from the first 100 simulated data for the weight function $w(l)$ (first column), ACEFR $f(E)$ (second column) and the time trend $h(t)$ (third column) are labelled by blue curves. The dashed blue curves show the mean of the estimates over all of the 10,000 simulated datasets. The true functions are the solid black curves.



Web Figure 10. Visualization of Simulation A Results. The data are generated under type (iii) weight function and type (ii) ACERF. The sample sizes are 1,000 (a) and 2,000 (b). The estimates from the first 100 simulated data for the weight function $w(l)$ (first column), ACEFR $f(E)$ (second column) and the time trend $h(t)$ (third column) are labelled by blue curves. The dashed blue curves show the mean of the estimates over all of the 10,000 simulated datasets. The true functions are the solid black curves.



Web Figure 11. Visualization of Simulation A Results. The data are generated under type (iii) weight function and type (iii) ACERF. The sample sizes are 1,000 (a) and 2,000 (b). The estimates from the first 100 simulated data for the weight function $w(l)$ (first column), ACEFR $f(E)$ (second column) and the time trend $h(t)$ (third column) are labelled by blue curves. The dashed blue curves show the mean of the estimates over all of the 10,000 simulated datasets. The true functions are the solid black curves.

Web Appendix H.2.2 Monte Carlo Standard Errors in Simulation A

Web Table 3. Monte Carlo Standard Errors in Simulation A under different weight functions w and ACERFs f . The Monte Carlo Standard Error for RMSE, 95% confidence intervals coverage (Cvg) and average widths (Width) for w and f with the sample size $N = 1000$ and 2000 are reported.

N	w			f		
	RMSE	Cvg	Width	RMSE	Cvg	Width
Type (i) w						
1000	0.000	0.001	0.000	0.001	0.001	0.000
2000	0.000	0.000	0.000	0.000	0.001	0.000
Type (ii) f						
1000	0.000	0.001	0.000	0.002	0.001	0.003
2000	0.000	0.000	0.000	0.000	0.001	0.000
Type (iii) f						
1000	0.000	0.001	0.000	0.000	0.002	0.000
2000	0.000	0.001	0.000	0.000	0.002	0.000
Type (ii) w						
1000	0.000	0.001	0.000	0.001	0.001	0.000
2000	0.000	0.001	0.000	0.000	0.001	0.000
Type (ii) f						
1000	0.000	0.001	0.000	0.001	0.001	0.001
2000	0.000	0.000	0.000	0.000	0.001	0.000
Type (iii) f						
1000	0.000	0.001	0.000	0.000	0.002	0.000
2000	0.000	0.001	0.000	0.000	0.002	0.000
Type (iii) w						
1000	0.000	0.001	0.000	0.001	0.001	0.001
2000	0.000	0.000	0.000	0.000	0.001	0.000
Type (ii) f						
1000	0.000	0.001	0.000	0.004	0.001	0.005
2000	0.000	0.000	0.000	0.000	0.001	0.000
Type (iii) f						
1000	0.000	0.001	0.000	0.000	0.002	0.000
2000	0.000	0.001	0.000	0.000	0.002	0.000

Web Appendix H.2.3 Results for Other Terms in Simulation A

Web Table 4. Results for other terms in Simulation A under different weight functions and ACERFs. The RMSE, 95% confidence intervals coverage (Cvg) and average widths (Width) for the time trend $h(t)$, and the Bias and RMSE for dispersion parameter θ with $N = 1000$ and 2000 are reported.

N	h			θ	
	RMSE	Cvg	Width	Bias	RMSE
Type (i) w; Type (i) f					
1000	0.037	0.960	(0.155)	0.104	0.744
2000	0.037	0.966	(0.159)	0.060	0.512
Type (i) w; Type (ii) f					
1000	0.040	0.960	(0.169)	0.163	0.902
2000	0.040	0.967	(0.171)	0.090	0.598
Type (i) w; Type (iii) f					
1000	0.036	0.961	(0.153)	0.090	0.697
2000	0.036	0.968	(0.157)	0.057	0.485
Type (ii) w; Type (i) f					
1000	0.037	0.960	(0.156)	0.091	0.736
2000	0.037	0.966	(0.159)	0.047	0.501
Type (ii) w; Type (ii) f					
1000	0.040	0.960	(0.170)	0.150	0.886
2000	0.040	0.967	(0.172)	0.090	0.594
Type (ii) w; Type (iii) f					
1000	0.036	0.960	(0.152)	0.092	0.686
2000	0.036	0.967	(0.155)	0.047	0.476
Type (iii) w; Type (i) f					
1000	0.038	0.958	(0.157)	0.028	0.961
2000	0.038	0.966	(0.162)	0.074	0.541
Type (iii) w; Type (ii) f					
1000	0.038	0.959	(0.160)	0.126	0.835
2000	0.038	0.967	(0.161)	0.071	0.516
Type (iii) w; Type (iii) f					
1000	0.038	0.961	(0.160)	0.115	0.792
2000	0.038	0.967	(0.165)	0.066	0.559

Web Appendix H.2.4 Results for Delta Method in Simulation A

The only difference between the delta method and the sampling method lies in the confidence intervals for w . We report the Cvg and Width of the 95% confidence intervals using the sampling method and delta method in Web Table 5 for comparison. We can observe the wide confidence intervals and over-coverage from the delta method. Hence, the delta method is less recommended than the sampling method.

Web Table 5. Additional Results in Simulation A. The coverage (Cvg) and average widths (Width) of 95% confidence intervals for w using the sampling method and delta method are reported.

N	w			
	Sampling		Delta	
	Cvg	Width	Cvg	Width
Type (i) w; Type (i) f				
1000	0.970	(0.064)	0.991	(0.094)
2000	0.979	(0.049)	0.992	(0.068)
Type (i) w; Type (ii) f				
1000	0.977	(0.055)	0.992	(0.086)
2000	0.980	(0.042)	0.993	(0.062)
Type (i) w; Type (iii) f				
1000	0.961	(0.075)	0.991	(0.120)
2000	0.973	(0.060)	0.992	(0.090)
Type (ii) w; Type (i) f				
1000	0.965	(0.060)	0.987	(0.090)
2000	0.966	(0.044)	0.988	(0.061)
Type (ii) w; Type (ii) f				
1000	0.968	(0.051)	0.989	(0.079)
2000	0.973	(0.038)	0.990	(0.055)
Type (ii) w; Type (iii) f				
1000	0.954	(0.071)	0.986	(0.113)
2000	0.964	(0.055)	0.988	(0.083)
Type (iii) w; Type (i) f				
1000	0.964	(0.063)	0.979	(0.144)
2000	0.975	(0.050)	0.990	(0.100)
Type (iii) w; Type (ii) f				
1000	0.975	(0.060)	0.991	(0.139)
2000	0.979	(0.047)	0.991	(0.098)
Type (iii) w; Type (iii) f				
1000	0.969	(0.093)	0.996	(0.256)
2000	0.976	(0.078)	0.992	(0.203)

Web Appendix H.3 Supplementary Simulation: Linear f

In Simulation A, the data are generated from the model:

$$\log(\mu_t) = f \left\{ \int_0^{15} w(l)X(t-l)dl \right\} + h(t),$$

When f is linear (Type (iii)), the model reduces to a distributed lag (linear) model (DLM):

$$\log(\mu_t) = \beta \int_0^{15} w(l)X(t-l)dl + h(t),$$

which can be fitted using the existing methods such as Gasparrini (2013). In this Supplementary Simulation, we compare the ACE-DLNM and DLM under the settings Simulation A with Type (iii) linear f . Since the function w and the coefficient β are not mutually identifiable in the DLM, separate estimates for w and the linear f cannot be directly obtained. Therefore, we compare the DLM and DLNM using RMSE, 95% confidence intervals coverage (Cvg) and average widths (Width) for $f(\int_0^{15} w(l)X(t-l)dl)$ evaluated over $t \in \mathcal{T}$ across 10,000 replicates.

The results are reported in Web Table 6. The DLM correctly specifying the linear association yields slightly lower RMSE, narrower confidence intervals, as expected. The ACE-DLNM, despite assuming a flexible f , performs closely to the correctly specified DLM. In practice, if there is no strong evidence supporting a linear association, one would favour the ACE-DLNM which behaves well in both linear and non-linear settings.

Web Table 6. Simulation results under Type (iii) linear f . The ACE-DLNM and DLM are compared based on the RMSE, 95% confidence intervals coverage (Cvg) and average widths (Width) for $f(\int_0^{15} w(l)X(t-l)dl)$ evaluated over $t \in \mathcal{T}$ across 10,000 replicates with sample size $N = 1000$ and 2000.

w	N	ACE-DLNM			DLM		
		RMSE	Cvg	Width	RMSE	Cvg	Width
Type (i)	1000	0.038	0.947	0.143	0.036	0.953	0.140
	2000	0.028	0.953	0.107	0.027	0.957	0.104
Type (ii)	1000	0.038	0.945	0.142	0.037	0.950	0.138
	2000	0.028	0.952	0.105	0.027	0.954	0.103
Type (iii)	1000	0.044	0.953	0.167	0.043	0.957	0.163
	2000	0.033	0.957	0.126	0.032	0.958	0.122

Web Appendix H.4 Supplementary Simulation: Misspecification

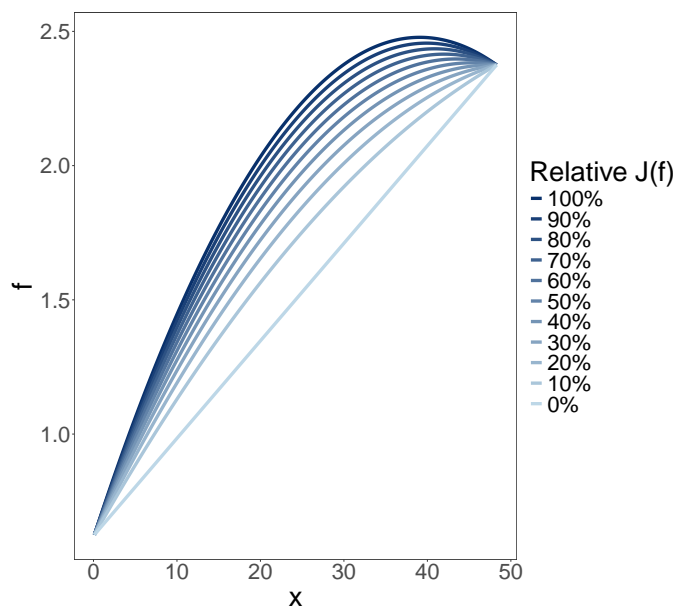
We conduct two supplementary simulation studies to investigate the sensitivity of the proposed ACE-DLNM framework to misspecification of the model assumption. The ACE-DLNM framework assumes that the association function applies to the ACE. Here we consider two misspecification scenarios: (A) the association function applies directly to the exposure and remains constant over time; and (B) the association function applies directly to the exposure and changes with time. Under both scenarios, the DRF-DLNM is correctly specified.

Web Appendix H.4.1 Misspecification Scenario A

We generate data from a model where the association function applies directly to the exposure and remains constant over time, specifically:

$$\log(\mu_t) = \sum_{l=0}^{14} w(l)f(x_{t-l}) + h(t),$$

where $w(\cdot)$ is Type (i) in Simulation A (Section 4.1). Under this data-generating mechanism, the DRF-DLNM is correctly specified, while the ACE-DLNM is misspecified except when f is linear. We consider the function f from linear to non-linear as shown in Web Figure 12. We use the integrated squared second derivatives, $J(f) = \int [f''(x)]^2 dx$, to quantify the roughness of the function f (Green and Silverman, 1993). A higher value of $J(f)$ indicates a rougher f , and $J(f) = 0$ if f is linear. We calculate the relative roughness by dividing $J(f)$ by the value of the roughest function in Web Figure 12 shown in darkest blue. We would expect the ACE-DLNM to perform well with linear f , and to perform worse as the roughness $J(f)$ increases.



Web Figure 12. A set of functions f used in Misspecification Scenario A. The relative roughness $J(f)$ is indicated by color, with the roughest function shown in the darkest blue.

We compare the models using RMSE and 95% confidence intervals coverage (Cvg) for the distributed lag term $s_t = \sum_{l=0}^{14} w(l)f(x_{t-l})$ evaluated over $t \in \mathcal{T}$ across 10,000 replicates, reported in Web Table 7. The DRF-DLNM is correctly specified regardless of the shape of f , and performs better with low RMSE and near nominal coverage. When the f is linear (relative $J(f) = 0$), the ACE-DLNM is also correctly specified and achieves low RMSE and near nominal coverage, close to the DRF-DLNM. As f becomes increasingly non-linear with higher roughness $J(f)$, the data-generating mechanism deviates from the model assumption of ACE-DLNM, leading to gradually increased RMSE and undercoverage. Overall, the ACE-DLNM maintains reasonable performance in this misspecification scenario, particularly when the association function is close to linear.

Web Table 7. Simulation results for Misspecification Scenario A. The ACE-DLNM and DRF-DLNM are compared based on the RMSE, 95% confidence intervals coverage (Cvg) under different relative roughness of the association function f .

Relative $J(f)$	ACE-DLNM		DRF-DLNM	
	RMSE	Cvg	RMSE	Cvg
0% (Linear)	0.025	0.951	0.025	0.965
10%	0.039	0.869	0.032	0.966
20%	0.048	0.835	0.033	0.975
30%	0.055	0.806	0.034	0.977
40%	0.061	0.784	0.035	0.978
50%	0.067	0.765	0.036	0.979
60%	0.073	0.748	0.036	0.979
70%	0.078	0.732	0.037	0.979
80%	0.082	0.719	0.037	0.979
90%	0.087	0.707	0.037	0.979
100%	0.091	0.696	0.038	0.979

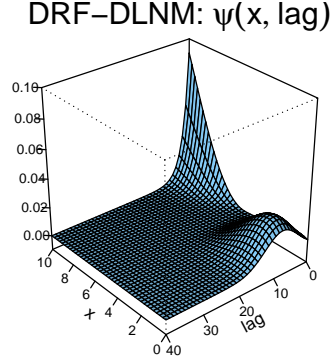
Web Appendix H.4.2 Misspecification Scenario B

In this scenario, we generate data from a model in which the association function applies directly to the exposure but changes with time. This corresponds to the framework of the DRF-DLNM, as considered in, for example, Gasparrini et al. (2017). Specifically, we follow Gasparrini et al. (2017) to generate data from the model:

$$\log(\mu_t) = \sum_{l=0}^{40} \psi(x_{t-l}, l),$$

where the exposure-lag-response function $\psi(x_{t-l}, l)$ is taken from Scenario 2 in Gasparrini et al. (2017), as shown in Web Figure 13. The sample size is 5,114 and the exposure is the daily temperature in Chicago from 1987 to 2000; see Gasparrini et al. (2017) for details. We compare the ACE-DLNM and DRF-DLNM under this setting. As the two models are reparameterized differently, we compare the models using RMSE and 95% confidence intervals coverage (Cvg) for the distributed lag term $s_t = \sum_{l=0}^{40} \psi(x_{t-l}, l)$ evaluated over

$t \in \mathcal{T}$ across 10,000 replicates, reported in Web Table 8. Because the data-generating mechanism deviates substantially from the model assumption of ACE-DLNM, it is difficult for the ACE-DLNM to capture the underlying model structure, yielding high RMSE and undercoverage. Similarly, in Simulation B in the main manuscript, the DRF-DLNM is misspecified and performs poorly.



Web Figure 13. The exposure-lag-response function used in Misspecification Scenario B, following the simulation study in Gasparrini et al. (2017).

Web Table 8. Simulation results for Misspecification Scenario B. The ACE-DLNM and DRF-DLNM are compared based on the RMSE, 95% confidence intervals coverage (Cvg).

	RMSE	Cvg
ACE-DLNM	0.017	0.424
DRF-DLNM	0.007	0.900

Overall, neither ACE-DLNM nor DRF-DLNM performs better in all settings — they are based on different model assumptions and the relative performance depends on how well their assumptions align with the data-generating mechanism. In practice, one may select between the two models based on AIC or interpretability considerations, as we illustrated in Section 5.

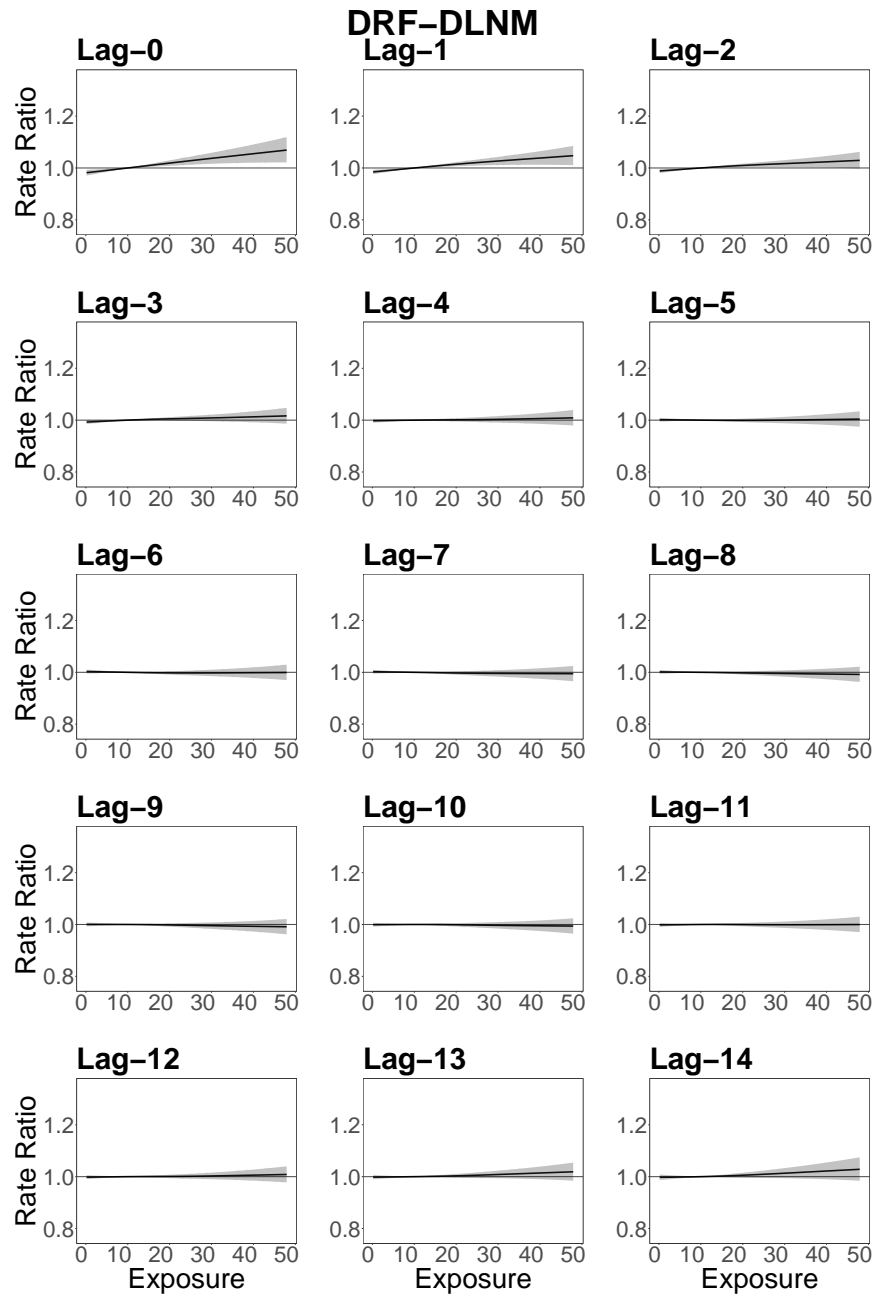
Web Appendix I Canadian Air Pollution Data

Web Appendix I.1 Data Summary

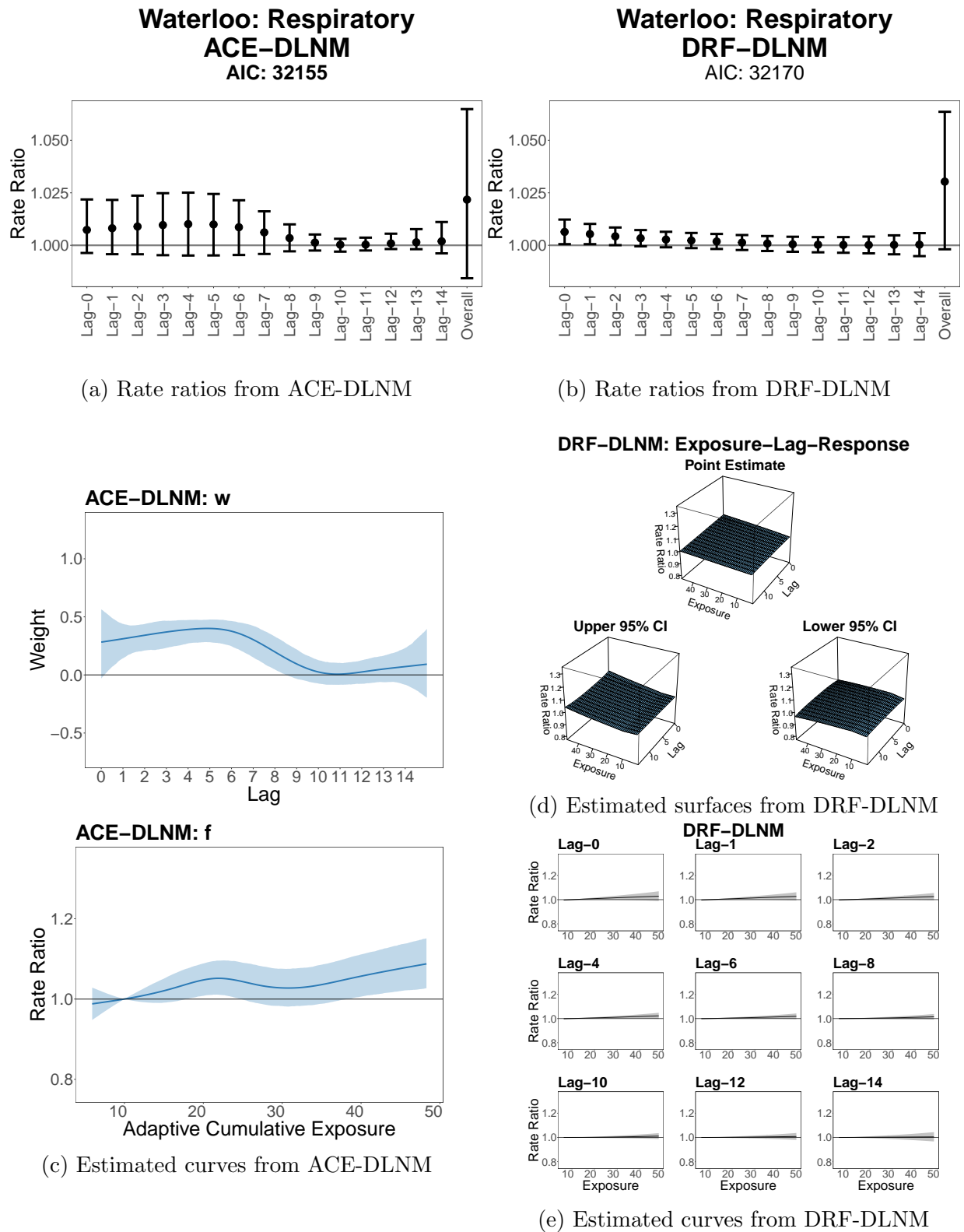
Web Table 9. Data Summary. We report the population in 2016, the daily average PM_{2.5} concentration ($\mu g/m^3$), and daily average respiratory morbidity count, from January 1, 2001 to December 31, 2018, along with sample variance in brackets.

	Waterloo	Peel	Hamilton	Calgary	Vancouver
Population (2016)	535,154	1,381,739	536,917	1,498,778	2,463,431
PM _{2.5} ($\mu g/m^3$)	7.6 (33.4)	7.5 (31.8)	8.6 (38.0)	8.0 (43.7)	5.3 (15.4)
Respiratory Morbidity	7.4 (12.5)	16.4 (37.2)	9.6 (16.0)	16.6 (38.8)	32.7 (113.6)

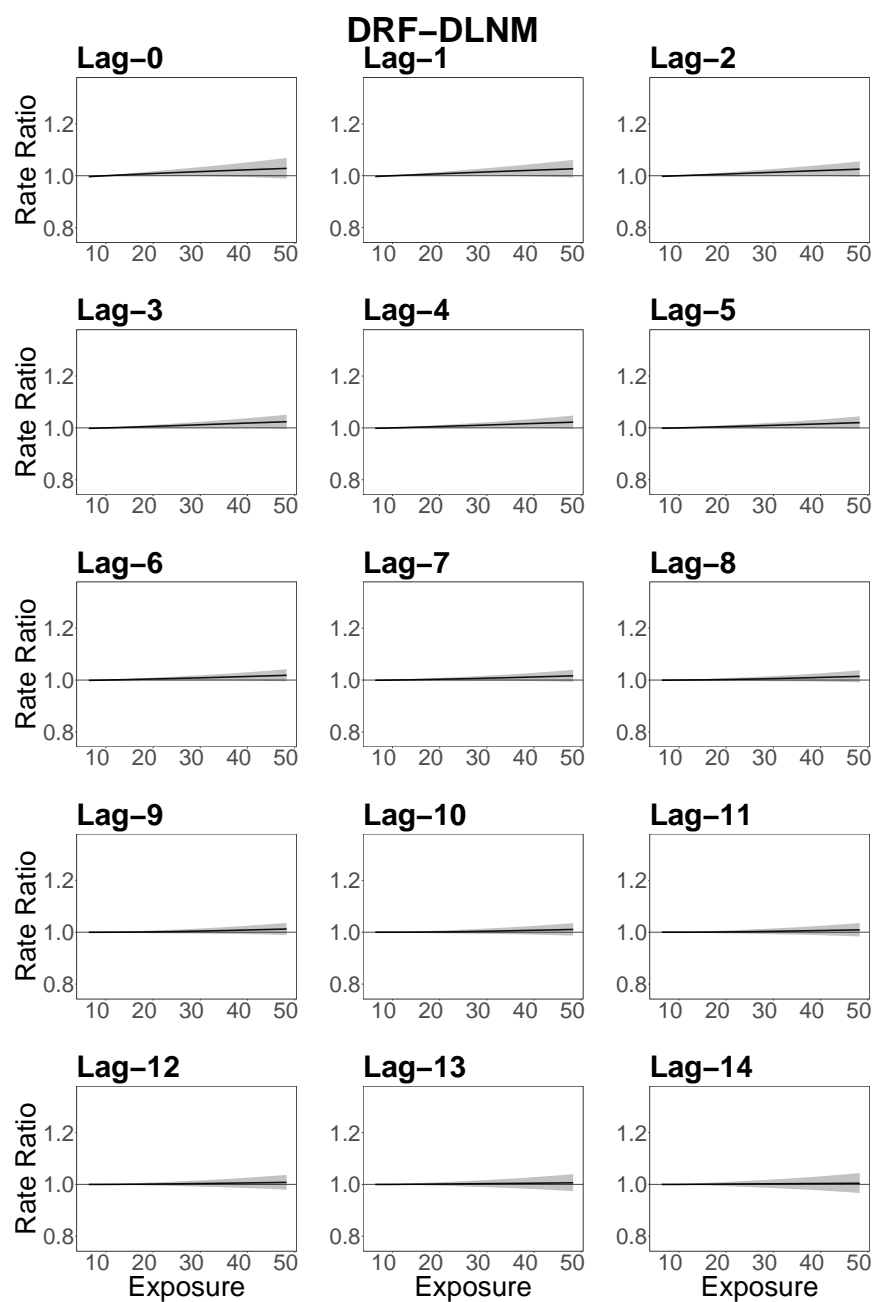
Web Appendix I.2 Additional Application Results



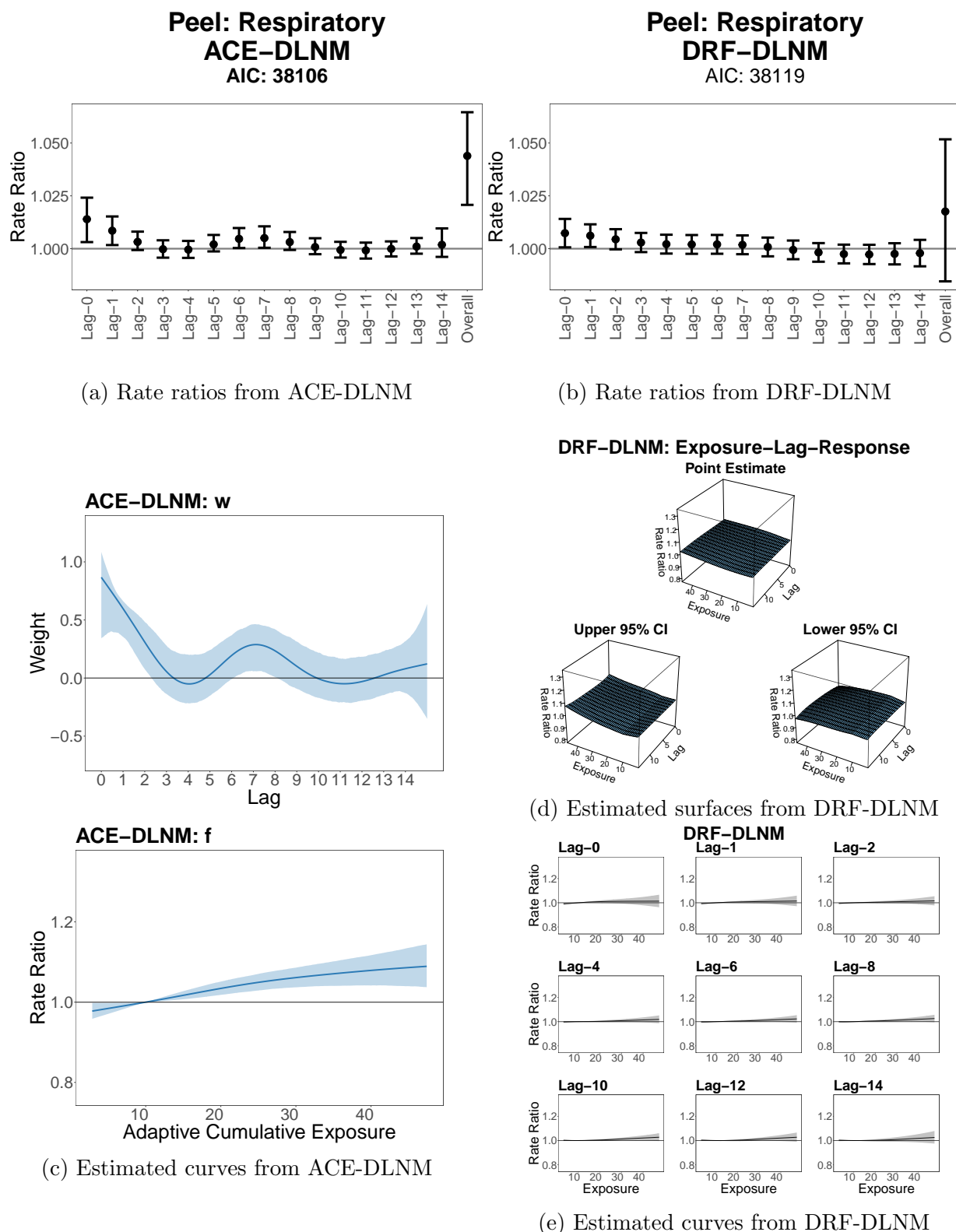
Web Figure 14. The estimated curves at each lag from the DRF-DLNM for the Hamilton dataset.



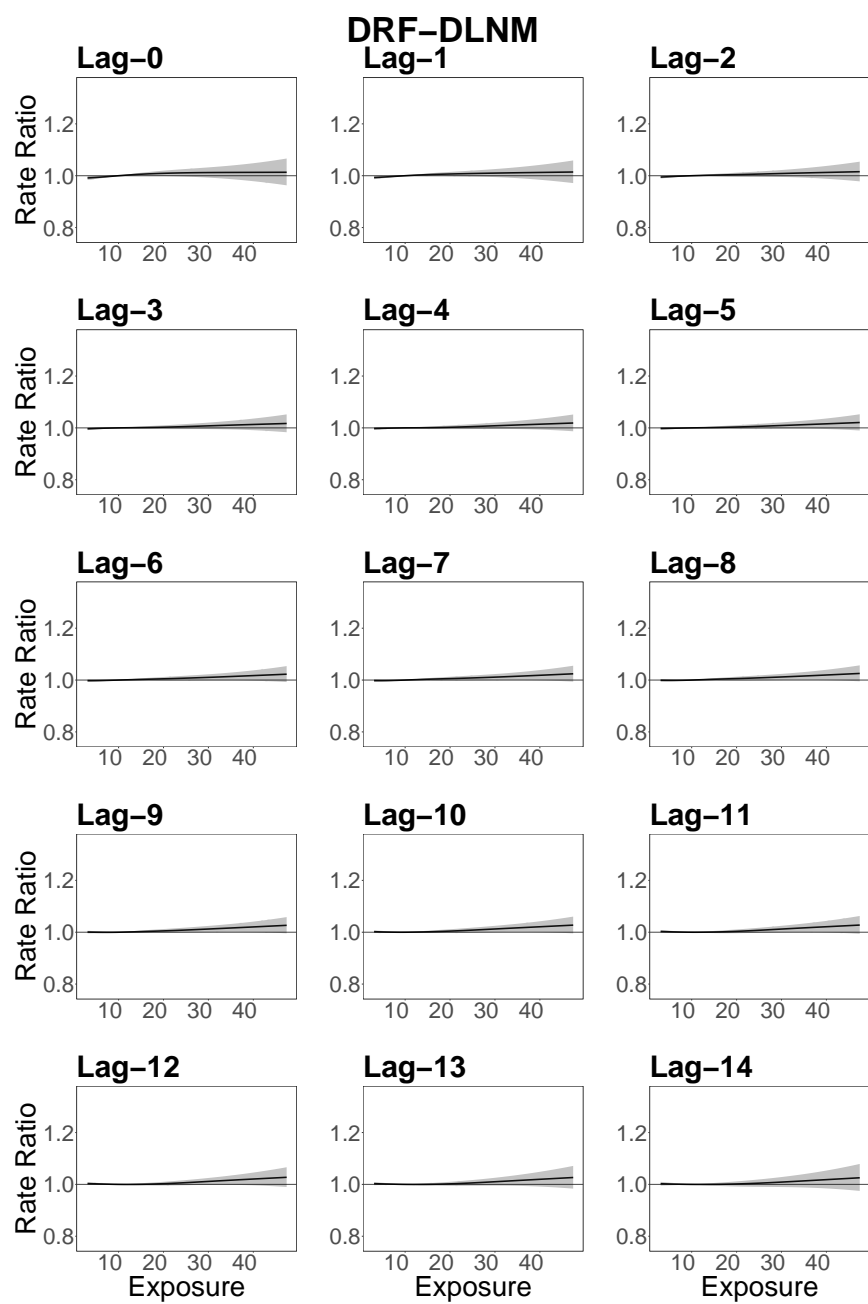
Web Figure 15. Comparisons between the ACE-DLNM and DRF-DLNM in the Waterloo dataset. The lag-specific and overall rate ratios from the ACE-DLNM (a) and DRF-DLNM (b) are plotted. Interpretation of the ACE-DLNM is based on the two curves shown in (c). Interpretation of the DRF-DLNM relies on the bivariate surfaces in (d), and we plot the estimated curves at selected lags in (e) (the full results are provided in Web Figure 16). The AICs for the two fitted models are reported.



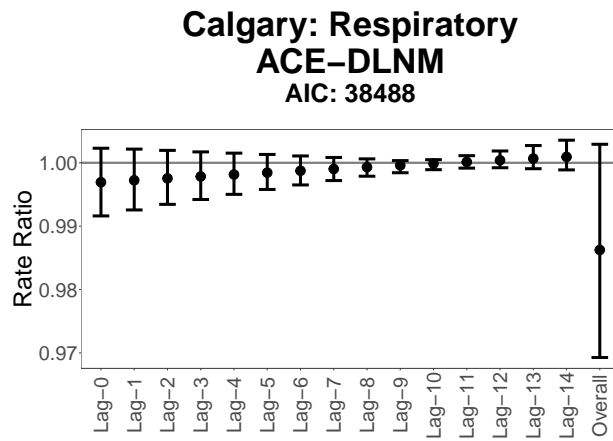
Web Figure 16. The estimated curves at each lag from the DRF-DLNM for the Waterloo dataset.



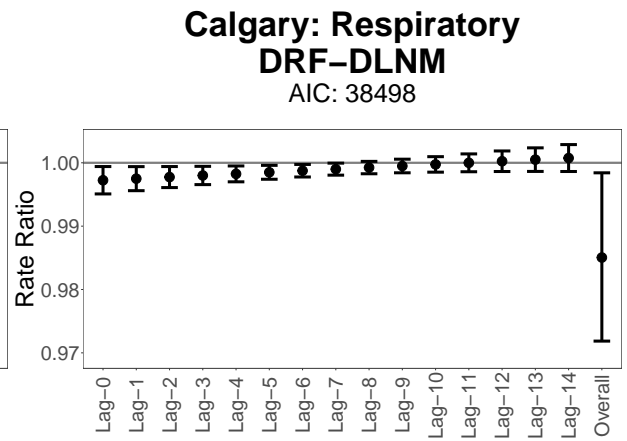
Web Figure 17. Comparisons between the ACE-DLNM and DRF-DLNM in the Peel dataset. The lag-specific and overall rate ratios from the ACE-DLNM (a) and DRF-DLNM (b) are plotted. Interpretation of the ACE-DLNM is based on the two curves shown in (c). Interpretation of the DRF-DLNM relies on the bivariate surfaces in (d), and we plot the estimated curves at selected lags in (e) (the full results are provided in Web Figure 18). The AICs for the two fitted models are reported.



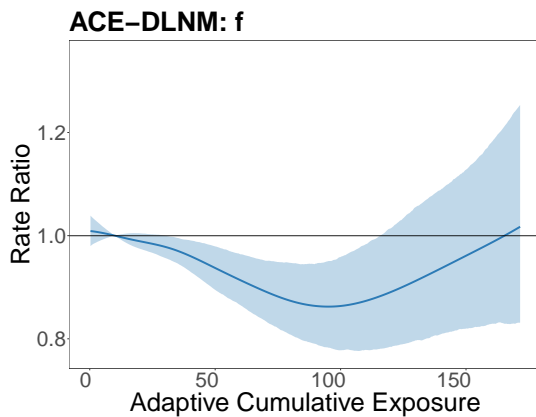
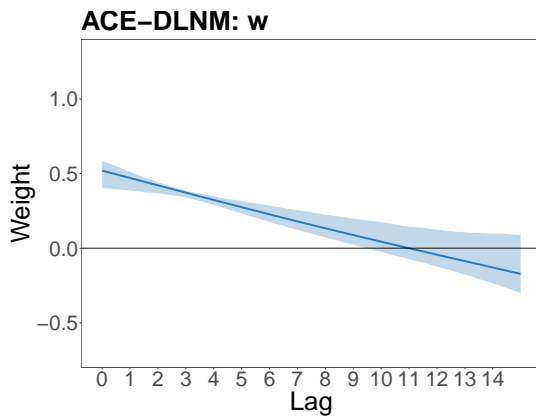
Web Figure 18. The estimated curves at each lag from the DRF-DLNM for the Peel dataset.



(a) Rate ratios from ACE-DLNM

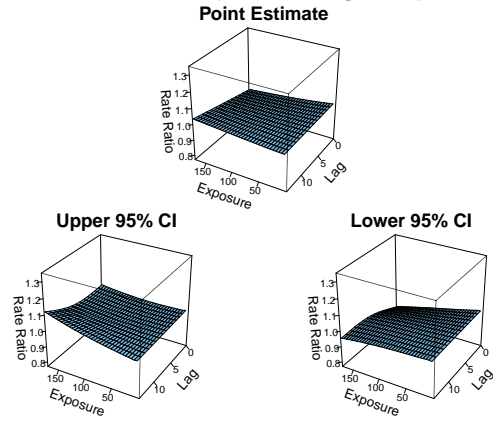


(b) Rate ratios from DRF-DLNM

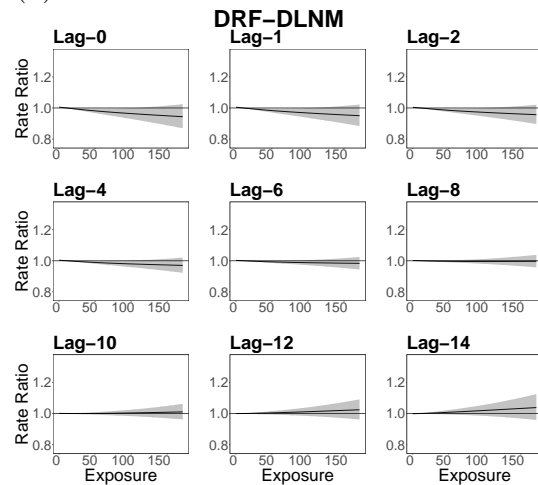


(c) Estimated curves from ACE-DLNM

DRF-DLNM: Exposure-Lag-Response

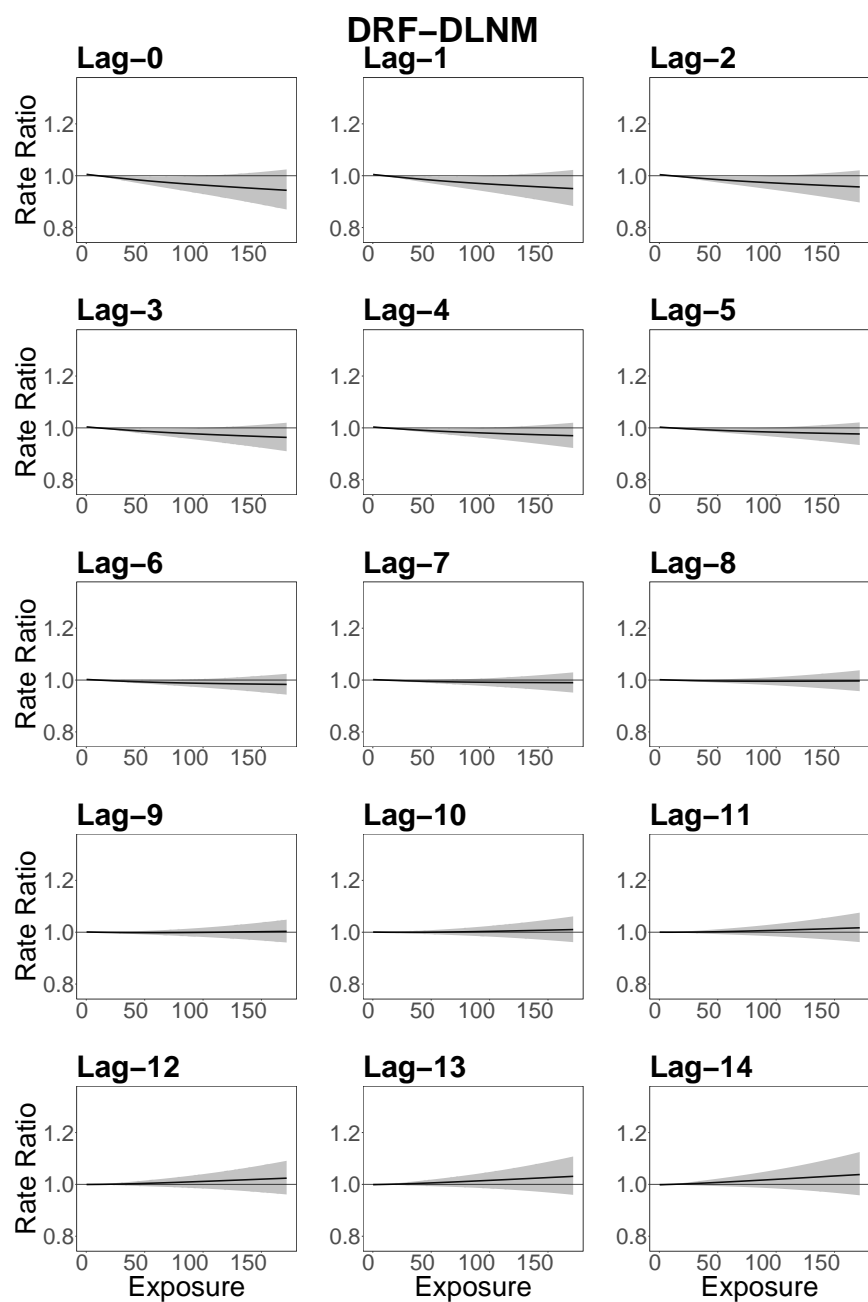


(d) Estimated surfaces from DRF-DLNM

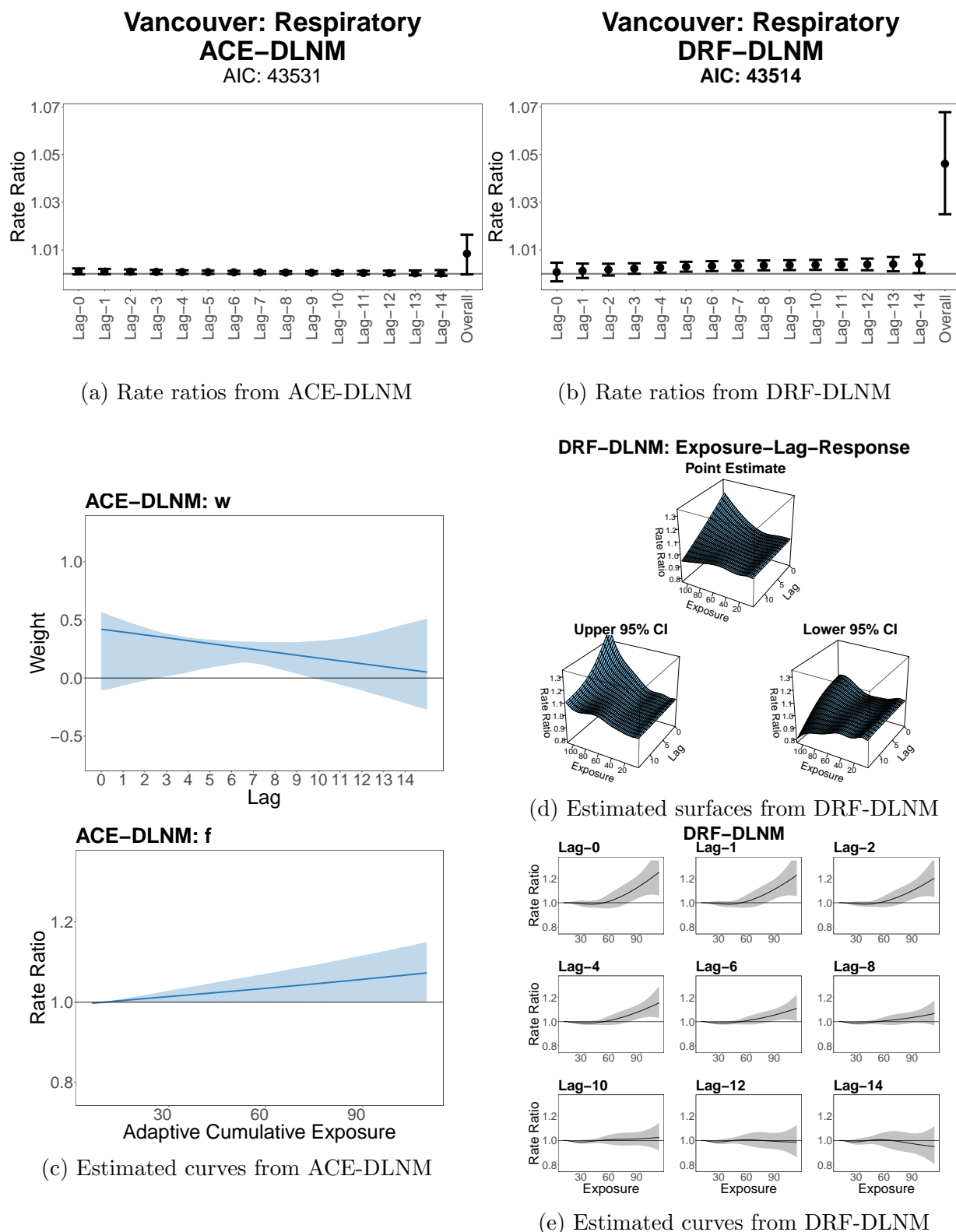


(e) Estimated curves from DRF-DLNM

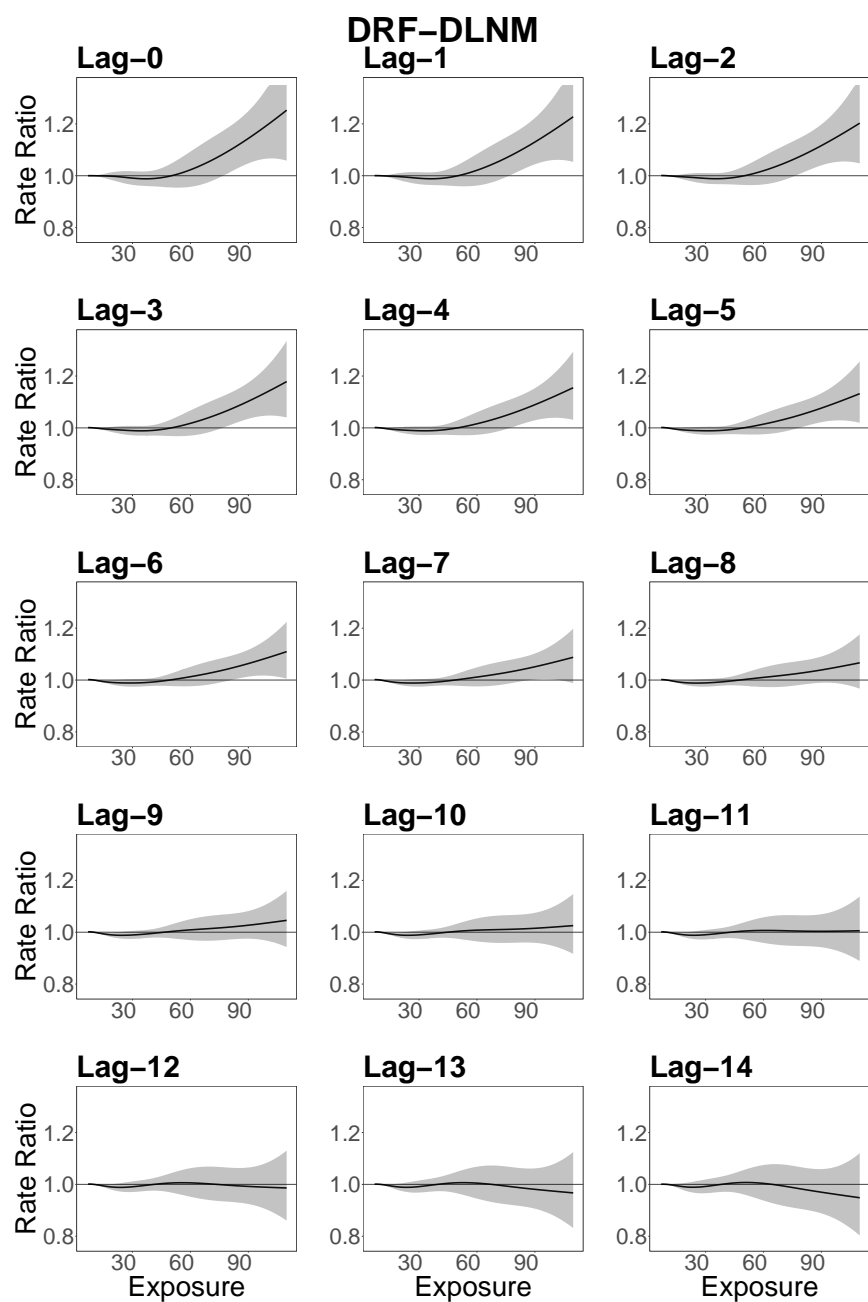
Web Figure 19. Comparisons between the ACE-DLNM and DRF-DLNM in the Calgary dataset. The lag-specific and overall rate ratios from the ACE-DLNM (a) and DRF-DLNM (b) are plotted. Interpretation of the ACE-DLNM is based on the two curves shown in (c). Interpretation of the DRF-DLNM relies on the bivariate surfaces in (d), and we plot the estimated curves at selected lags in (e) (the full results are provided in Web Figure 20). The AICs for the two fitted models are reported.



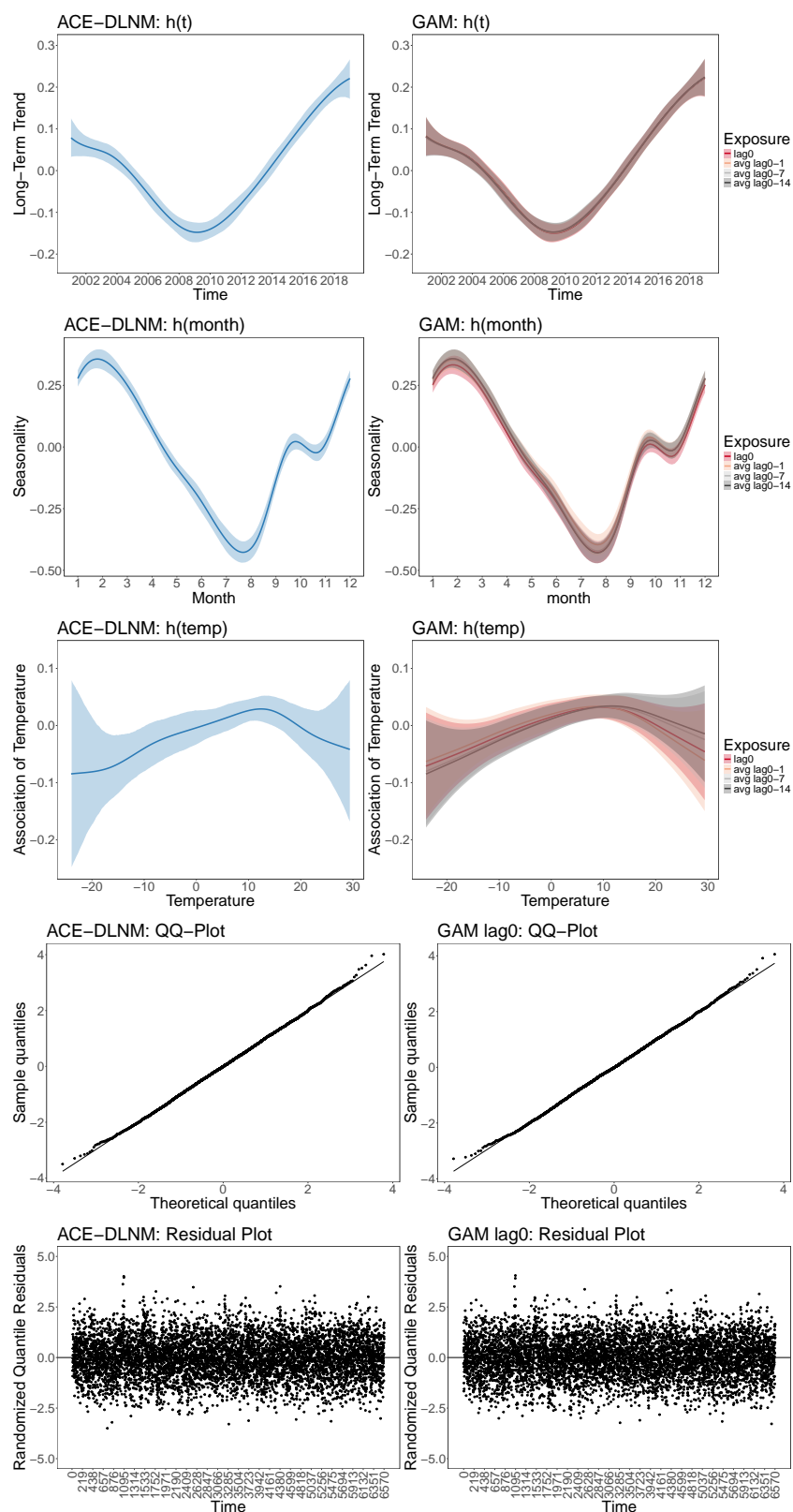
Web Figure 20. The estimated curves at each lag from the DRF-DLNM for the Calgary dataset.



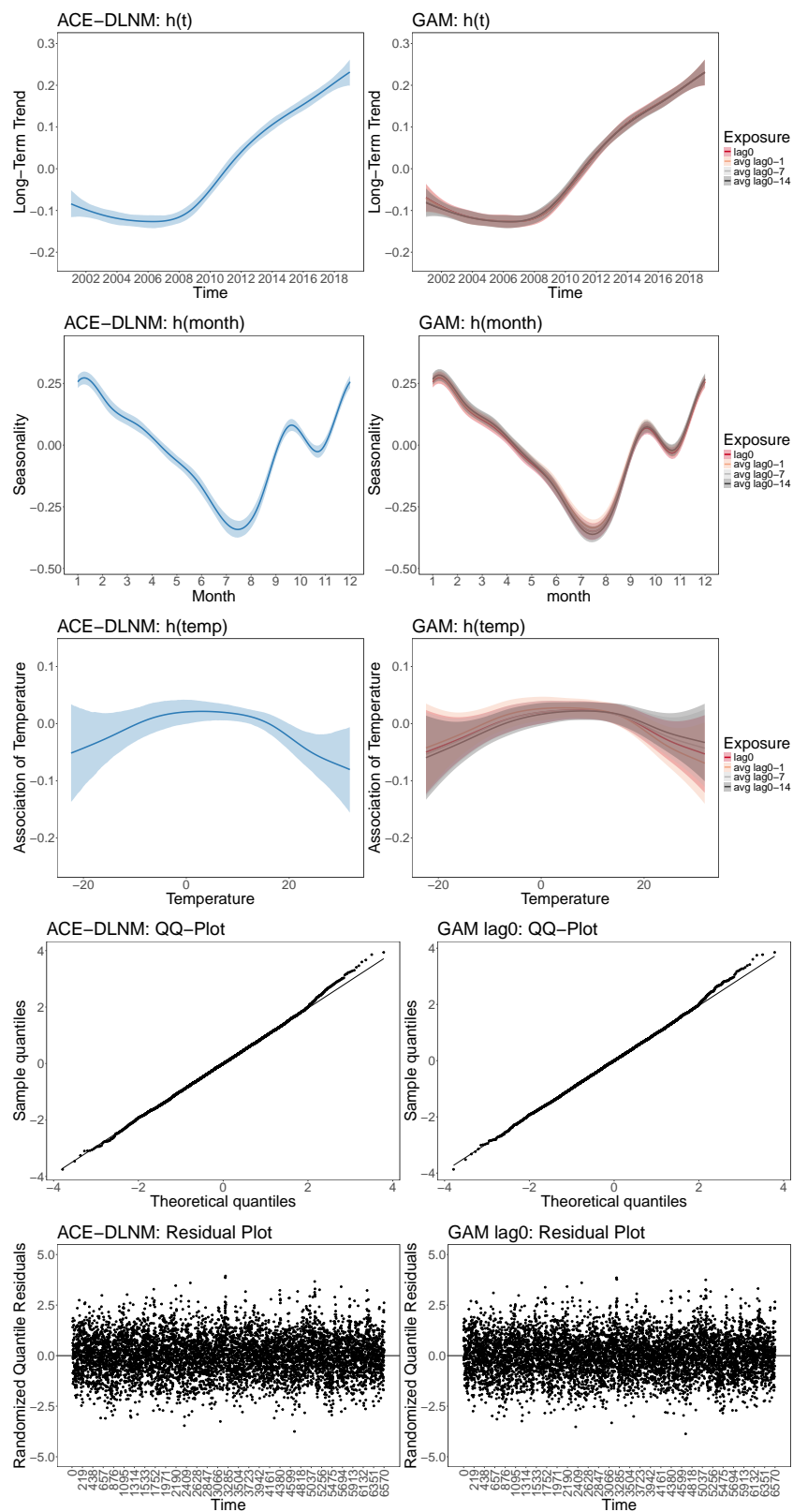
Web Figure 21. Comparisons between the ACE-DLNM and DRF-DLNM in the Vancouver dataset. The lag-specific and overall rate ratios from the ACE-DLNM (a) and DRF-DLNM (b) are plotted. Interpretation of the ACE-DLNM is based on the two curves shown in (c). Interpretation of the DRF-DLNM relies on the bivariate surfaces in (d), and we plot the estimated curves at selected lags in (e) (the full results are provided in Web Figure 22). The AICs for the two fitted models are reported.



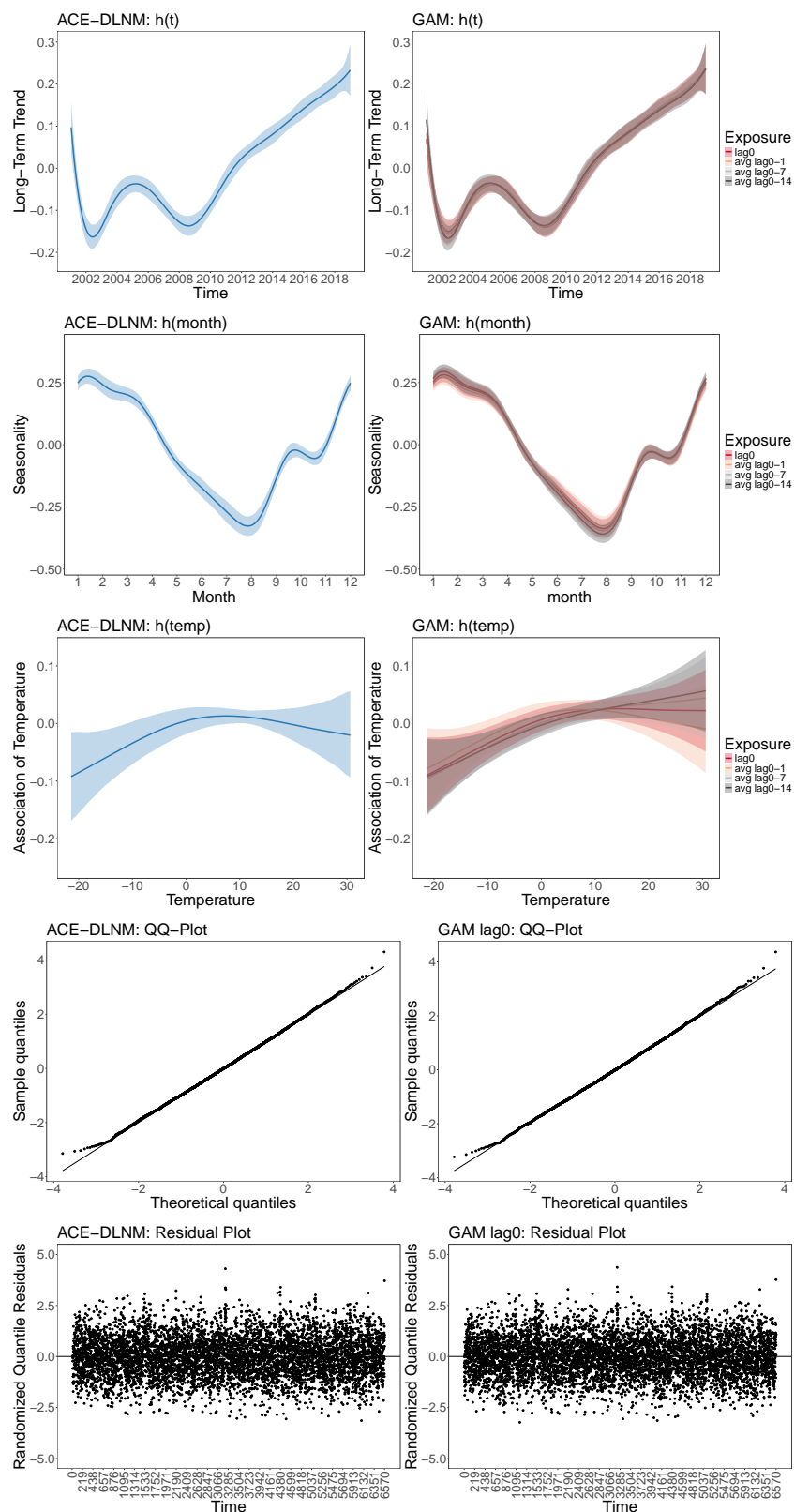
Web Figure 22. The estimated curves at each lag from the DRF-DLNM for the Vancouver dataset.



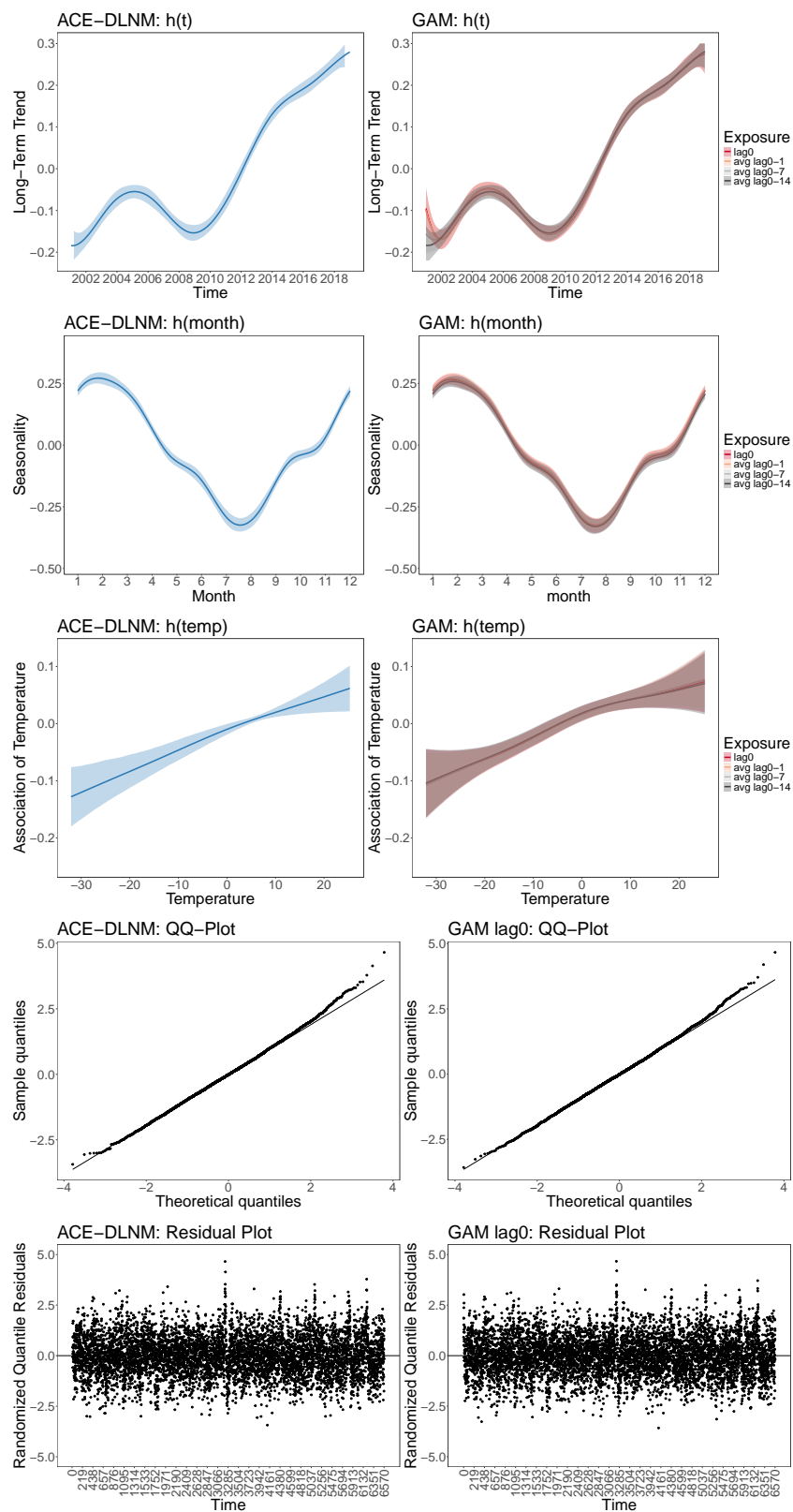
Web Figure 23. Additional Results for Respiratory Morbidity in Waterloo.



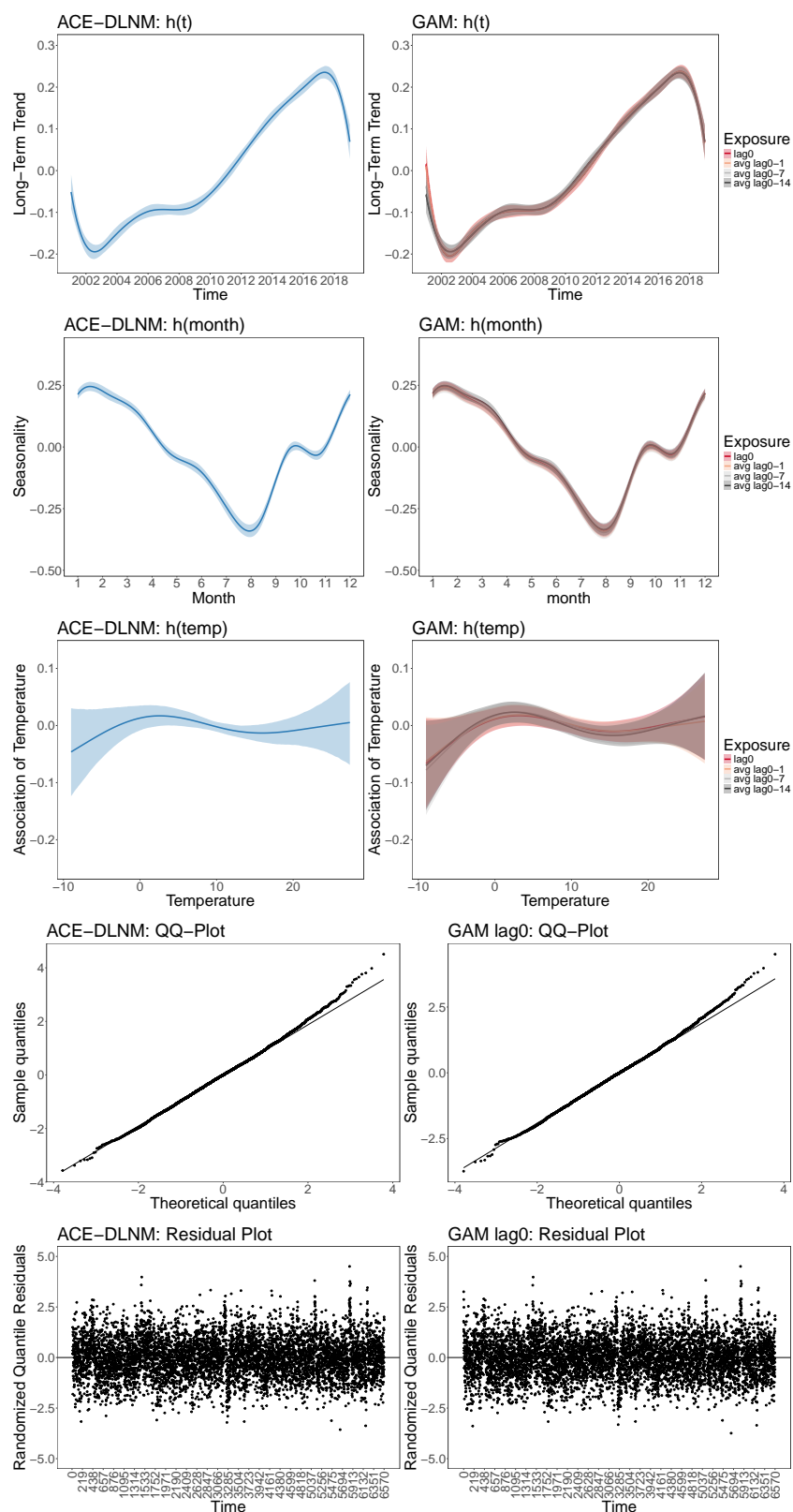
Web Figure 24. Additional Results for Respiratory Morbidity in Peel.



Web Figure 25. Additional Results for Respiratory Morbidity in Hamilton.



Web Figure 26. Additional Results for Respiratory Morbidity in Calgary.



Web Figure 27. Additional Results for Respiratory Morbidity in Vancouver.

Web Table 10. Estimates for the linear components and the dispersion parameter for respiratory morbidity in Waterloo.

	ACE-DLNM		GAM Lag0	
	Point Est.	CI Est.	Point Est.	CI Est.
Intercept	1.967	(1.884, 2.050)	1.898	(1.867, 1.929)
β Mon	0.192	(0.157, 0.227)	0.192	(0.157, 0.228)
β Tue	0.155	(0.119, 0.191)	0.156	(0.120, 0.192)
β Wed	0.096	(0.060, 0.133)	0.097	(0.060, 0.133)
β Thu	0.113	(0.077, 0.149)	0.114	(0.078, 0.151)
β Fri	0.072	(0.037, 0.108)	0.075	(0.038, 0.111)
β Sat	-0.049	(-0.086, -0.010)	-0.048	(-0.086, -0.011)
$\log \theta$	4.046		3.903	

Web Table 11. Estimates for the linear components and the dispersion parameter for respiratory morbidity in Peel.

	ACE-DLNM		GAM Lag0	
	Point Est.	CI Est.	Point Est.	CI Est.
Intercept	2.712	(2.651, 2.773)	2.679	(2.657, 2.702)
β Mon	0.183	(0.158, 0.209)	0.184	(0.158, 0.209)
β Tue	0.203	(0.178, 0.229)	0.204	(0.179, 0.229)
β Wed	0.134	(0.109, 0.161)	0.136	(0.110, 0.161)
β Thu	0.135	(0.109, 0.160)	0.135	(0.109, 0.161)
β Fri	0.084	(0.058, 0.109)	0.084	(0.059, 0.110)
β Sat	-0.038	(-0.065, -0.011)	-0.037	(-0.064, -0.011)
$\log \theta$	4.116		4.128	

Web Table 12. Estimates for the linear components and the dispersion parameter for respiratory morbidity in Hamilton.

	ACE-DLNM		GAM Lag0	
	Point Est.	CI Est.	Point Est.	CI Est.
Intercept	2.113	(2.060, 2.164)	2.171	(2.143, 2.199)
β Mon	0.126	(0.096, 0.156)	0.126	(0.094, 0.157)
β Tue	0.148	(0.117, 0.179)	0.149	(0.118, 0.180)
β Wed	0.093	(0.062, 0.124)	0.093	(0.061, 0.124)
β Thu	0.104	(0.073, 0.136)	0.105	(0.073, 0.136)
β Fri	0.100	(0.070, 0.132)	0.101	(0.069, 0.132)
β Sat	-0.041	(-0.073, -0.009)	-0.040	(-0.073, -0.008)
$\log \theta$	4.265		4.283	

Web Table 13. Estimates for the linear components and the dispersion parameter for respiratory morbidity in Calgary.

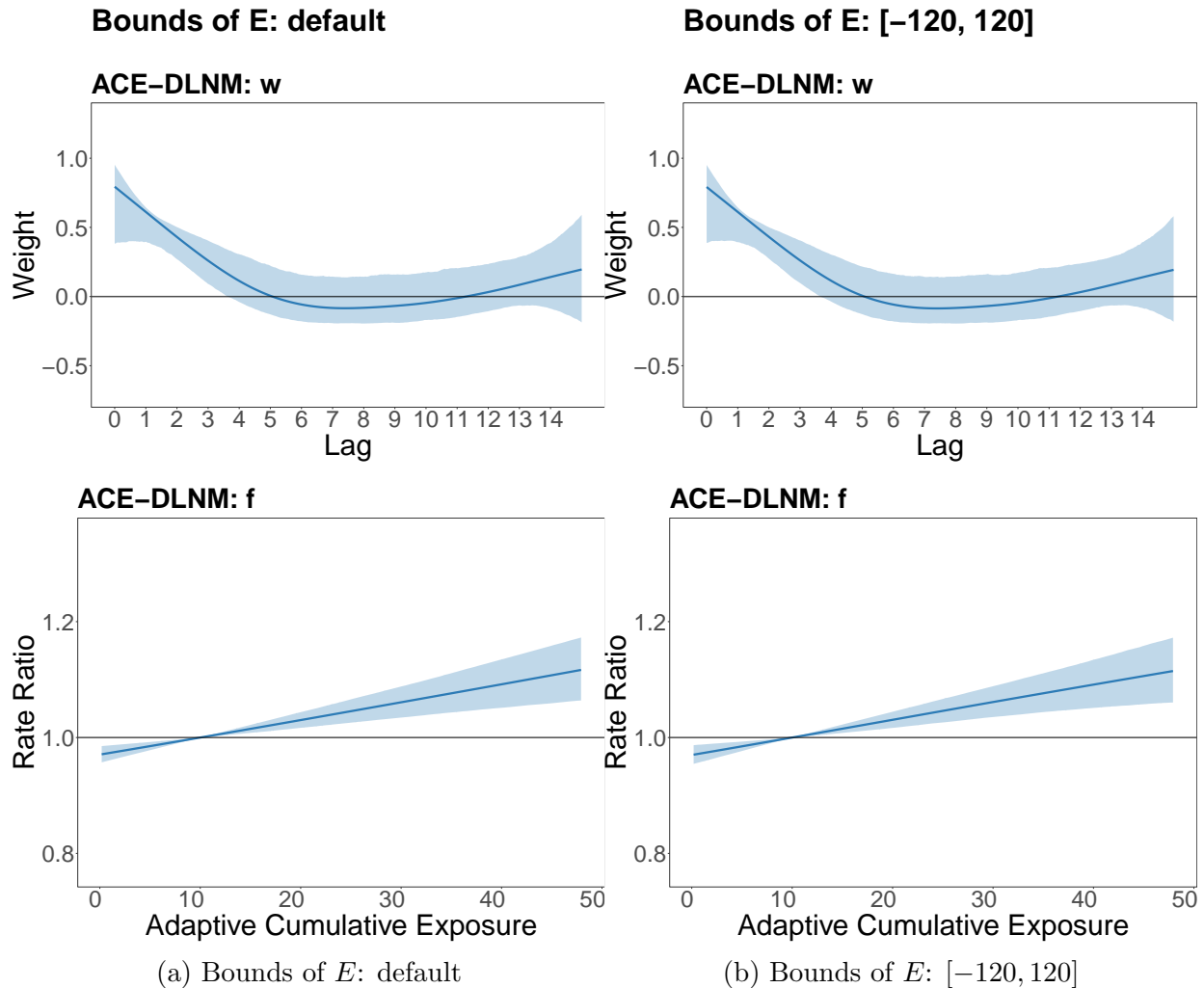
	ACE-DLNM		GAM Lag0	
	Point Est.	CI Est.	Point Est.	CI Est.
Intercept	2.735	(2.512, 2.951)	2.643	(2.614, 2.671)
β Mon	0.176	(0.150, 0.202)	0.177	(0.151, 0.203)
β Tue	0.154	(0.128, 0.181)	0.156	(0.130, 0.182)
β Wed	0.142	(0.116, 0.168)	0.143	(0.117, 0.169)
β Thu	0.146	(0.120, 0.173)	0.149	(0.123, 0.175)
β Fri	0.103	(0.077, 0.128)	0.104	(0.078, 0.131)
β Sat	-0.011	(-0.037, 0.017)	-0.010	(-0.036, 0.017)
$\log \theta$	3.929		3.924	

Web Table 14. Estimates for the linear components and the dispersion parameter for respiratory morbidity in Vancouver.

	ACE-DLNM		GAM Lag0	
	Point Est.	CI Est.	Point Est.	CI Est.
Intercept	3.405	(3.348, 3.461)	3.352	(3.332, 3.372)
β Mon	0.166	(0.147, 0.186)	0.166	(0.147, 0.186)
β Tue	0.181	(0.162, 0.201)	0.181	(0.162, 0.201)
β Wed	0.164	(0.145, 0.184)	0.164	(0.145, 0.184)
β Thu	0.117	(0.098, 0.137)	0.117	(0.098, 0.137)
β Fri	0.146	(0.128, 0.165)	0.146	(0.126, 0.165)
β Sat	-0.034	(-0.054, -0.013)	-0.034	(-0.054, -0.014)
$\log \theta$	4.268		4.267	

Web Appendix I.3 Sensitivity to the Bounds of ACE

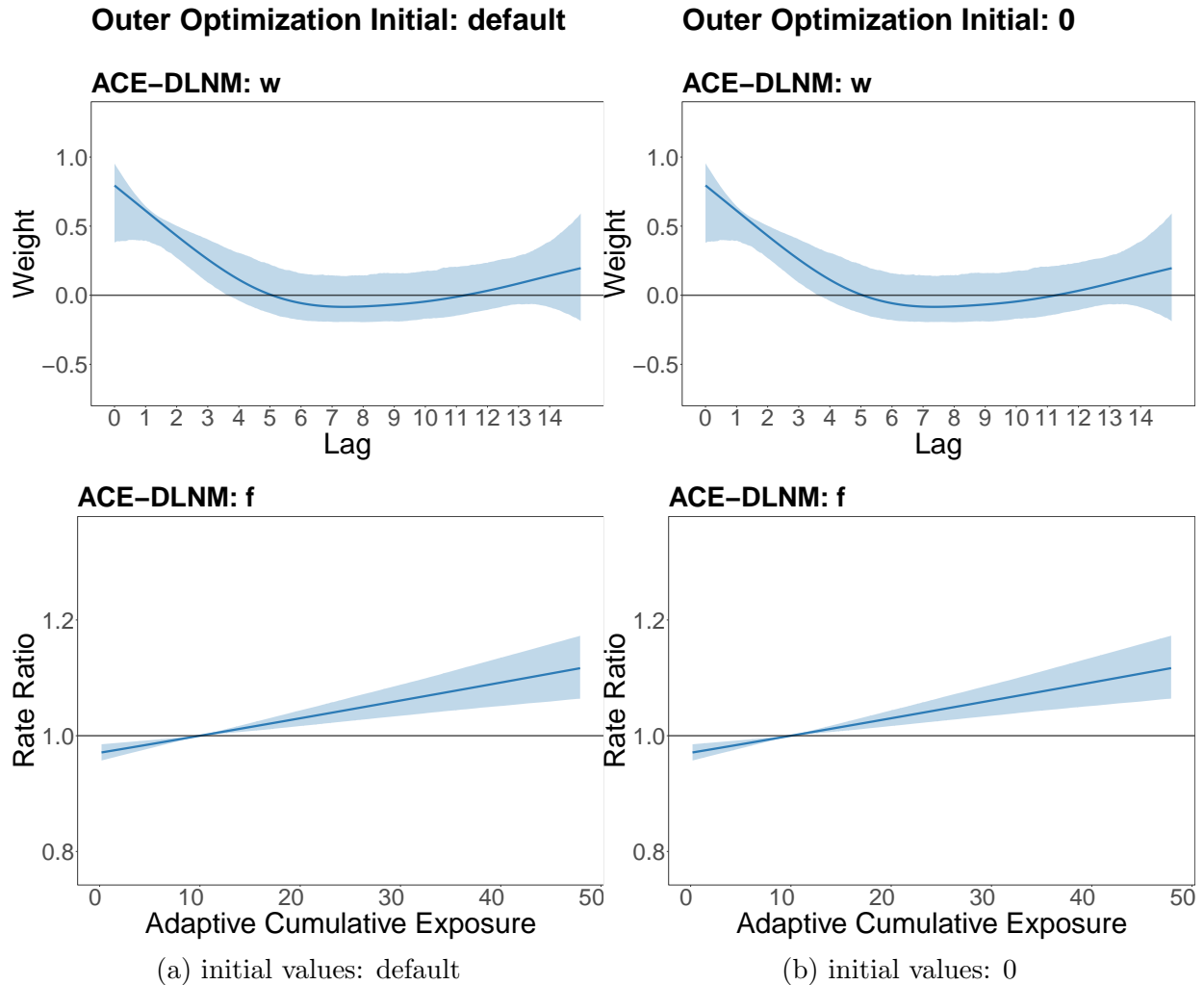
We use the Hamilton data as an example to investigate the sensitivity to bounds of the ACE. As introduced in Section 3.2, we use the pre-determined bounds for ACE through the Cauchy-Schwarz inequality, and then define the basis function and compute the penalty matrix accordingly. In the Hamilton dataset, the predetermined bounds are $[-94, 94]$ (rounded to integers in the implementation), and the range of the estimated ACE is $[-4.264, 69.800]$. We first re-fit the model using narrower bounds $[-70, 70]$, but the inner optimization algorithm cannot converge. We re-fit the model by setting the bounds as $[-120, 120]$, and find that the results remain the same; see Web Figure 28.



Web Figure 28. Estimates of w and f for the Hamilton dataset using (a) the default bounds of E ($[-94, 94]$ in this example) and (b) $[-120, 120]$ as the bounds of E .

Web Appendix I.4 Sensitivity to the Initial Values

We use the Hamilton data as an example to investigate the sensitivity to initial values of the outer optimization. The default and recommended choice of initial values is introduced in Web Appendix E. We re-fit the model by setting the initial values as 0, and find that the results remain the same; see Web Figure 29. However, when using 0 as the initial values, the BFGS algorithm converges in 48 iterations, while the BFGS algorithm with the recommended initial values converges in 37 iterations.



Web Figure 29. Estimates of w and f for the Hamilton dataset using (a) the default initial values and (b) 0 as the initial values.

Web Appendix I.5 Negative Binomial and Poisson Distribution

We compare the ACE-DLNMs under negative binomial response assumption and Poisson response assumption in terms of AIC. The model comparison results are reported in Web Table 15. For all cities, the negative binomial distribution yields smaller AICs. The results support our choice of the negative binomial response, which is the default for the proposed framework implemented in the R package `aceDLNM`.

Web Table 15. AICs for ACE-DLNMs with negative binomial response (default in `aceDLNM`) and Poisson response.

	Negative Binomial	Poisson
Waterloo	32155	32232
Peel	38106	38314
Hamilton	33869	33923
Calgary	38488	38786
Vancouver	43531	44038